HARVARD UNIVERSITY

THE GRADUATE SCHOOL OF ARTS AND SCIENCES

THESIS ACCEPTANCE CERTIFICATE

(To be placed in Original Copy)

The undersigned, appointed by the

Division

Department of Physics

Committee

have examined a thesis entitled
"Cryogenic Scanning Probe Microscopy for Semiconductor Nanostructures"

presented by Mark Alan Eriksson

candidate for the degree of Doctor of Philosophy and hereby certify that it is worthy of acceptance.

Signature ....

Typed name Robert M. Westervelt, Chair

Signature ....

Typed name Eric J. Heller

Signature ....

Typed name Michael Tinkham

Date May 16, 1997

Cryogenic Scanning Probe Microscopy for Semiconductor Nanostructures

A thesis presented

by

Mark Alan Eriksson

to

The Department of Physics

in partial fulfillment of the requirements

for the degree of

Doctor of Philosophy

in the subject of

Physics

Harvard University

Cambridge, Massachusetts

May, 1997

UMI Number: 9733280

Copyright 1997 by
Eriksson, Mark Alan

All rights reserved.

UMI Microform 9733280
Copyright 1997, by UMI Company. All rights reserved.

This microform edition is protected against unauthorized
copying under Title 17, United States Code.

UMI
300 North Zeeb Road
Ann Arbor, MI 48103

© 1997 by Mark Alan Eriksson
All rights reserved.

Abstract

This thesis presents research on the application of scanning probe microscopy to the study of semiconductor nanostructures. Scanning probe microscopy is a potentially valuable tool for studying nanostructures, because it provides data on the spatial profile of experimental quantities. Although research on both scanning probe microscopy and semiconductor nanostructures is well established, until recently there has been little contact between the two. Obstacles have included the need for low temperatures in nanostructure experiments, the difficulty of aligning microscopes to single devices on large substrates, and the sensitivity of semiconductor nanostructures to both light and lower frequency electrical noise. New developments in cryogenic scanning probe techniques provide a way to overcome these obstacles.

We begin with a description of the techniques used to fabricate semiconductor nanostructures. Next, we present a detailed description of the scanning probe microscope we designed and built for nanostructure experiments. The special requirements which our scanning probe microscope meets in order to study semiconductor nanostructures are explained. We report an experiment using our scanning probe microscope to study electron transport through a classical ballistic point contact. This experiment allows us to image properties of the point contact which have previously been measured indirectly or have previously been inaccessible, such as the

collimation of the electron flux near the point contact and the distribution of current in the contact itself. Resolution limits and the imaging mechanism of the microscopy are discussed. Finally, we present the results of calculations done by collaborators which show that this microscopy has the potential to image individual quantum states in nanostructures at low temperatures.

Table of Contents

Abstract iii

Table of Contents v

Acknowledgments viii

CHAPTER 1 *Introduction* 1

1.1 Mesoscopic physics and nanostructures 2
1.2 Overview of the thesis 3

CHAPTER 2 *Experimental system: technology and physics* 5

2.1 Heterostructure growth and 2DEGs 6
Heterostructure growth 6
Wafer design — band structure engineering 8
Heterostructure characterization 14
Heterostructures used in this research 15
2.2 Lithography 15
Electron beam lithography vs. photolithography 16
Spinning resist 17
Pattern design 19
Sample mounting 21
Writing the pattern on the SEM 22
Developing the sample 23
2.3 Evaporation and wire-bonding 23
Evaporation and liftoff 24
Wirebonding 27
2.4 Ohmic contact to the 2DEG 30
2.5 Lateral confinement of the 2DEG 33
Surface gates 33
Mesa etches 34

CHAPTER 3 *A scanning probe microscope for low temperature mesoscopic physics* 38

3.1 Overview of scanning probe microscopy 38
History and operating principles 39
Goal of our research 45
3.2 Deflection sensors 47
Piezoresistive cantilevers 48
3.3 Microscope stage 56
SPM stage head 57
SPM stage base 60
3.4 Reduction of vibration induced noise 64
Vibration rejection 64
Vibration isolation 67
3.5 Dewar 69
Dewar basics and operation 69
SPM mounting and feedthroughs. 72
3.6 SPM electronics 74
Overview of the SPM electronics 74
Control electronics 77
Feedback and Z electrode electronics 81
3.7 Computer control system 83
NB-MIO16X Board 83
Control program 85
3.8 SPM performance 87

CHAPTER 4 *Change in sheet density due to a biased SPM tip* 90

4.1 Geometry for the calculation 91
4.2 Sheet density perturbations 94

CHAPTER 5 *Scanned gate imaging of point contact electronic properties* 100

5.1 Scanned gate experiments 101
Introduction 101
AC versus DC perturbations 103
5.2 Classical ballistic point contacts 104
Motivation 104

Sample 105
Change in resistance images 107
The contrast mechanism 110
Scattering model and peak profiles 114
5.3 Quantum point contacts 120
Motivation and theory 120
Theoretical predictions 123

CHAPTER 6 ***Conclusions and future directions*** **127**

APPENDIX A ***Procedure for making PC boards*** **131**

Acknowledgments

The last five years have been a very enjoyable time for me, and it is a pleasure to make several acknowledgments.

The most important acknowledgment I can make is that I have learned more from my friends and teachers than I ever anticipated since coming to this university five years ago. A large part of the credit goes to my advisor Bob Westervelt. Bob has encouraged and supported me through a difficult but very rewarding thesis project. I have learned a lot of physics while working with him, but most of all Bob has taught me to think like a scientist.

I would also like to thank the other members of my committee. Professor Tinkham has provided support throughout my thesis project, and I particularly enjoyed his class on superconductivity. Professor Heller has also been very supportive, and I have enjoyed our discussions on modeling experiments in ballistic microstructures.

I have worked especially closely with several of my fellow students in the Westervelt group. Jordan Katine took me under his wing early in graduate school and taught me much of what I know about low noise measurements, and he also managed to transfer to me some small fraction of his vast store of trivia. Rex Beck is one of the clearest thinking experimentalists I have ever worked with, and his continual good cheer has made the 2nd floor a very happy place to do research. I have had a good time working with Mark Topinka to iron out the kinks in our scanning probe microscope, and I will

always be grateful for his considerable skill at programming computers. Carol Livermore has been a great scientist to work with and has provided much valuable advice — technical and otherwise — and she has always been quick with humorous insights into the sometimes bizarre world out there.

It has been a lot of fun working with Catherine Crouch on Physics 11b, and she also weathered the storm of first year classes with me, always making them more pleasant. Aram Adourian continues to broaden my horizons, both inside and outside of physics, and his good sense of humor is always appreciated. Junmin Hu provided balance in our group by resisting the urge to work with semiconductors — at least until after she graduated. It has been a lot of fun getting to know and working with Marija Drndic, Dave Duncan, and Lester Chen, and I wish them the best of luck in the coming years.

In my first year in the Westervelt group John Baskey, Doug Mar, Fred Waugh, Michael Berry, and Scott Yang all were helpful in getting me started in my research. Ed Hogan has kept the administrative side of life from encroaching into the lab. Steve Shepard has done a fantastic job keeping the clean room running smoothly, and he continually goes the extra mile to help out in many different ways.

To Chuck Black I owe thanks for answering my naive and incessant questions about SPMs when I was first starting out. Dan Ralph has been a great mentor, and I hope I will continue to benefit from his advice.

I want to include special thanks to the people I worked with at the University of Wisconsin-Madison, Professors Max Lagally, Dan McCammon, C.C. Lin, and L.W.

Anderson, all of whom provided me with an amazingly broad and useful research experience.

Rich Finlay has been a great friend throughout graduate school, and I am especially pleased that we were able to keep Experimental Kids up and on its feet.

My fiancee Roberta Peyer has been supportive throughout the long process of this thesis research — even going as far as picking up a soldering iron when necessary. The best part of the year is yet to come.

Finally, I want to thank my parents. Their help, good advice, and support have been invaluable. They have taught best by example, and I look forward to learning as much from them in the future as I have in the past.

CHAPTER 1 Introduction

In 1947, fifty years ago this year, the transistor was invented by Bardeen, Brattain, and Shockley.[1,2] One of the key elements in their discovery, which revolutionized solid state electronics and physics, was the ability to control the position and type of dopant atoms in a semiconductor crystal.[3] In the intervening decades, the technology of semiconductor device fabrication has seen steady progress. That progress now enables fantastic control of semiconductor properties down to the atomic length scale.

The ability to grow semiconductor crystals with precisely tuned carrier densities and band profiles has resulted in the development of a number of new semiconductor

1. J. Bardeen and W.H. Brattain, *Phys. Rev.* 74, 230 (1948).
2. W. Shockley, *Bell Syst. Tech. J.* **28**, 435 (1949).
3. For a review semiconductor device technology see S.M. Sze, *Physics of Semiconductor Devices*, John Wiley and Sons, New York (1981).

devices. One of the most important advances for our work was the development of the two-dimensional electron gas, which is described in chapter two. Two dimensional electron gases are excellent systems in which to fabricate electron devices known as nanostructures. As their name implies, nanostructures are devices whose characteristic size is on the nanometer length scale. These devices have become the system of choice for studying the interesting field of mesoscopic physics.[4]

1.1 Mesoscopic physics and nanostructures

A mesoscopic electron device is neither macroscopic nor microscopic, but rather has an intermediate size. Mesoscopic physics is therefore concerned with systems which are most naturally described neither by classical models nor by fully quantum mechanical treatments. The physics of mesoscopic devices is governed by the interplay between the size of the device and the natural length scales of the underlying system.[4]

Semiconductor devices are excellent candidates for studying mesoscopic physics because of the overlap between the natural length scales for electron transport in semiconductors and the range of possible semiconductor device sizes. Examples of important length scales for electrical transport are the electron mean free path, the electron phase coherence length, and the electron Fermi wavelength. Current fabrication technology allows researchers to make devices which have sizes comparable to all of these length scales. Over the last decade many new discoveries in mesoscopic physics

4. For a review of mesoscopic devices see *Nanostructures and Mesoscopic Systems*, ed. by Wiley P. Kirk and Mark A. Reed, Academic Press, Inc., San Diego (1992).

have been made in nanostructures formed in two-dimensional electron gases. However, because of the low temperatures required to study nanostructures, it has been difficult to perform experiments which image the important physics of these devices.

Imaging techniques have been important in many scientific disciplines, and semiconductor physics is no exception. Examples of microscopes which have been useful for studying semiconductors include the scanning electron microscope, the transmission electron microscope, and more recently the atomic force microscope. It is the purpose of this thesis to apply the techniques of scanning probe microscopy to the low temperature study of semiconductor nanostructures with the goal of imaging some of the important properties of these mesoscopic semiconductor devices.

1.2 Overview of the thesis

In chapter 2 we describe the fabrication of semiconductor nanostructures. Our fabrication process is a collaboration between researchers at Harvard University and the University of California-Santa Barbara (UCSB). The molecular beam epitaxy for our samples, which is described in chapter 2, is performed by our collaborators at UCSB. All of the lithography and other fabrication steps are done in Gordon McKay Laboratory at Harvard University.

Chapter three presents a description of the scanning probe microscope (SPM) we designed and built for the study of semiconductor nanostructures. We discuss the

special requirements our instrument satisfies in order to study nanostructures, and we also discuss the performance of the SPM.

In chapter 4 we present calculations which determine one of the resolution limits on our microscopy. The calculations are also important in interpreting the data in chapter 5.

Chapter 5 describes an experiment studying the flow of electrons through a classical ballistic point contact in a near surface two-dimensional electron gas. We discuss the imaging mechanism for our microscopy, using this experiment as an example. The images are interpreted in terms of a scattering model and are shown to reveal details about the flow of current through the point contact. We also present calculations done by students working with Professor Heller at Harvard University, which show that our experimental method may be able to resolve individual quantum states in semiconductor nanostructures.

Finally, chapter 6 presents ideas on improving the scanning probe microscope and possibilities for several future experiments.

CHAPTER 2

Experimental system: technology and physics

Semiconductor nanostructures are excellent systems for studying phenomena in mesoscopic physics. It is possible to make semiconductor nanostructures in many different ways, but one of the most flexible is to form the nanostructures out of a two-dimensional electron gas, or 2DEG. As will be seen in this chapter, the advantage of the 2DEG system is this flexibility. Electrical leads are easily attached to nanostructures formed in 2DEGs, and nanostructure size and shape can be controlled while the experiment is in progress. Furthermore, the heterostructures in which 2DEGs are formed are particularly clean systems.

This chapter describes several steps in nanostructure fabrication. It opens with an explanation of the physics and the fabrication of heterostructures containing two-

dimensional electron gases, which form the basis for all of our nanostructures. Next we present an overview of electron beam lithography, which is important in fabricating nanostructures. Ohmic contact to the 2DEG is discussed, and finally we present the evaporation and etching procedures which are used to transfer the nanostructure pattern to the 2DEG.

2.1 Heterostructure growth and 2DEGs

A heterostructure consists of crystalline thin films grown on top of a crystalline substrate, such that the lattices of the overlayers and the substrate are well matched and have few interface defects. A growth process which extends a single crystal in this way is called epitaxial growth. Most thin film growth procedures, such as those described below in section 2.3, result in a polycrystalline film which is not matched in a useful way to the substrate crystal lattice. Epitaxial growth is a much more sophisticated technique, which builds atomic layers one by one, placing the atoms in the correct lattice sites. Epitaxially grown heterostructures can be produced in many materials systems, but the most important example for this work is the $GaAs/Al_xGa_{1-x}As$ system. At the present time, it is in these structures that the highest quality 2DEGs can be fabricated.[1]

2.1.1 Heterostructure growth

There are two common methods for growing epitaxial layers on semiconductor crystals: molecular beam epitaxy (MBE) and metal organic chemical vapor deposition

1. M.J. Kelly, *Low-Dimensional Semiconductors*, Oxford University Press, Oxford, (1995).

(MOCVD). The technology of the two techniques is substantially different. The introductory book by Kelly[1] provides an overview of each method and a bibliography of references. Here we will discuss only MBE, the technique used by our collaborators at the University of California-Santa Barbara to grow the semiconductor heterostructures used in our experiments.

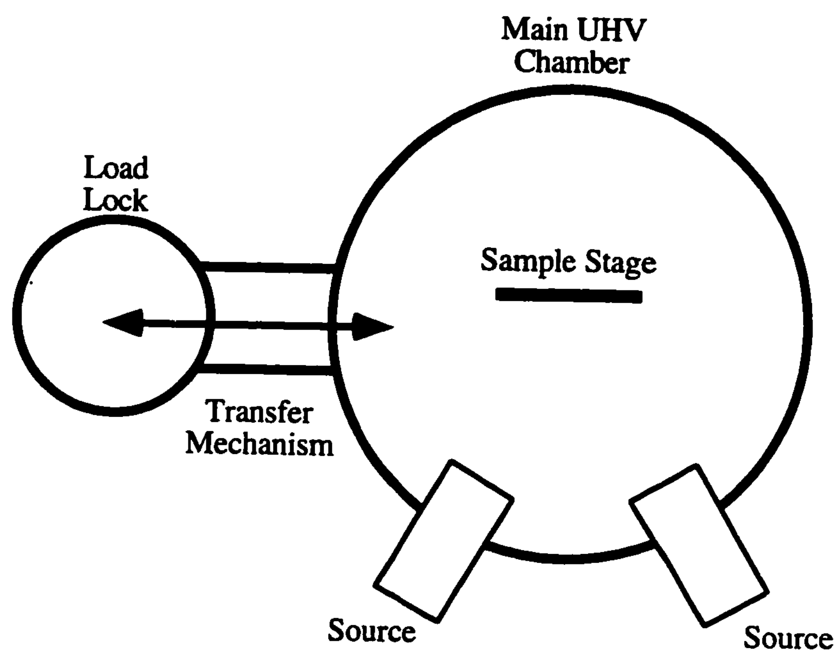

Figure 2-1 Schematic of an MBE system.

Figure 2-1 is a schematic diagram of some of the important elements in an MBE system. MBE is performed in ultra-high vacuum (UHV) chambers, at pressures as low as 10^{-11} torr. The MBE system at UCSB uses large cryopumps to maintain this low pressure; cryopumps are used because of their large pumping speed and because they are very clean pumps. In addition to the commercial cryopumps, liquid nitrogen shields are

placed in the growth region of the chamber. These shields tend to adsorb any gas atoms which strike them.

As indicated in figure 2-1, MBE is essentially a sophisticated evaporation technique. Sources containing the elements to be deposited are heated to increase the vapor pressure of those atoms. Shutters over the sources control which type of atom strikes the sample surface. The sample is usually rotated at an angular frequency of approximately 1 Hz, to increase the uniformity of the epitaxial layers. In addition to an excellent vacuum, the most important parameters in MBE growth are the substrate temperature and the partial pressures at the sample surface of the various deposition atoms. Typical substrate temperatures for GaAs depositions are of order 600 °C.[1]

2.1.2 Wafer design — band structure engineering

Given the ability to control the atomic structure of a crystal lattice layer by layer, it is possible to make a variety of sophisticated electronic structures. One of the more important examples is the two-dimensional electron gas, which is the basis for the devices studied in this work.

Figure 2-2 shows the composition by layer of one of the heterostructures used in our work, wafer KC9.[2] The process of designing heterostructures is often given the name band structure engineering, because tuning the atomic composition and the number and

2. The naming convention we use is that the initials of the grower start the name, and the number indicates the number of wafers that person has grown for us. KC9 is the ninth wafer grown for us at UCSB by Ken Campman.

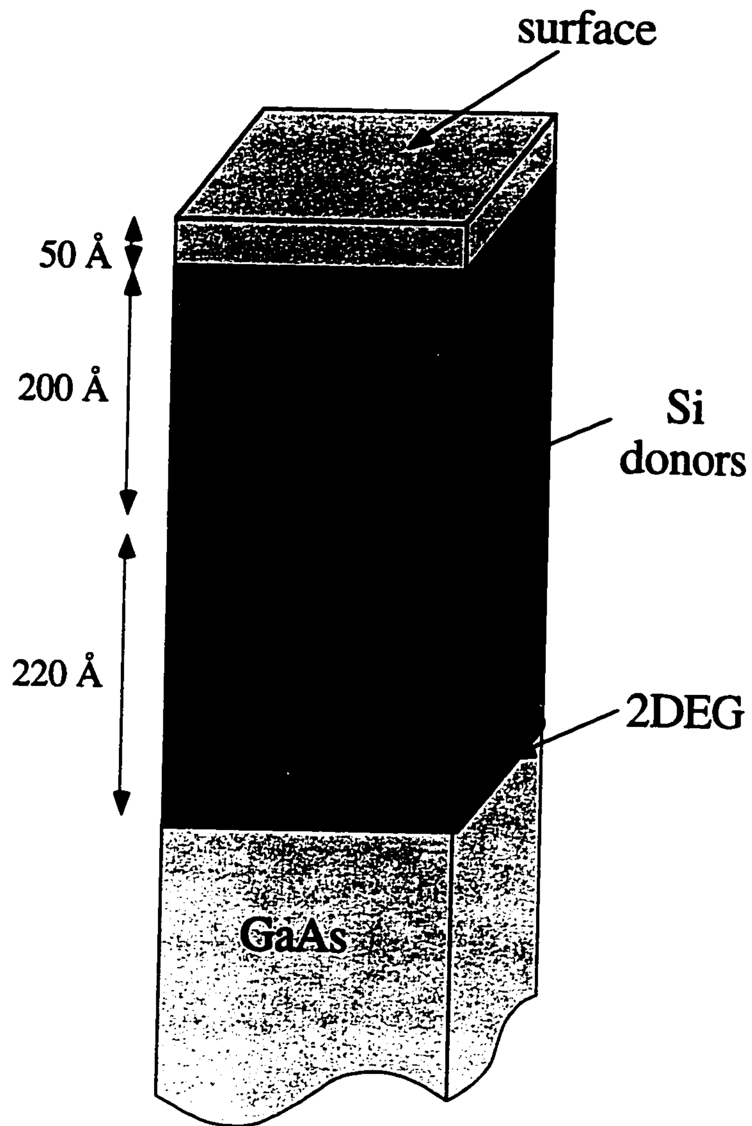

Figure 2-2 Heterostructure profile of wafer KC9.

position of the dopants allows control of the band energies. In the $Al_xGa_{1-x}As/GaAs$ system, we take advantage of the band gap difference and conduction band offset between $Al_xGa_{1-x}As$ and GaAs. In our heterostructures we use $x = 0.3$ in the $Al_xGa_{1-x}As$ layer.

Table 2-1 summarizes some important parameters for understanding the design of our heterostructures. The bandgap in $Al_{0.3}Ga_{0.7}As$ is larger than the band gap in GaAs by 360 meV at low temperature. This results in a shift in the conduction bands from one layer to the next. The conduction band shift allows the formation of the 2DEG.

TABLE 2-1 Conduction Band Properties for GaAs and $Al_{0.3}Ga_{0.7}As$[a]

(eV)	300 K		4.2 K	
	GaAs	$Al_{0.3}Ga_{0.7}As$	GaAs	$Al_{0.3}Ga_{0.7}As$
Band Gap	1.42	1.80	1.31	1.67
Conduction Band Offset	0.33		~0.3[b]	

a. Assembled from *Gallium Arsenide*, ed. by J. S. Blakemore, American Institute of Physics, New York (1987).

b. Approximate value quoted in Harris et al.[7]

Two-dimensional electron gases are formed in our heterostructures at the interface between the GaAs and the $Al_{0.3}Ga_{0.7}As$ layers. Figure 2-3 shows a schematic of the self-consistent conduction band edge energy as a function of depth into the semiconductor in the effective mass approximation.[3] The self-consistent solution for the conduction band edge is important because it determines where the free carriers will sit in the heterostructure. The trick in designing these structures is to arrange the layer composition, layer thickness, dopant positions, and dopant densities such that the Fermi

3. C. W. J. Beenakker, and H. van Houten, "Quantum Transport in Semiconductor Nanostructures," *Sol. State Phys.* **44**, H Eherenreich and D. Turnbull, eds., Academic Press, San Diego, CA (1991).

Energy lies above the conduction band edge only in the narrow V-shaped potential well just beneath the $Al_{0.3}Ga_{0.7}As$ layer.

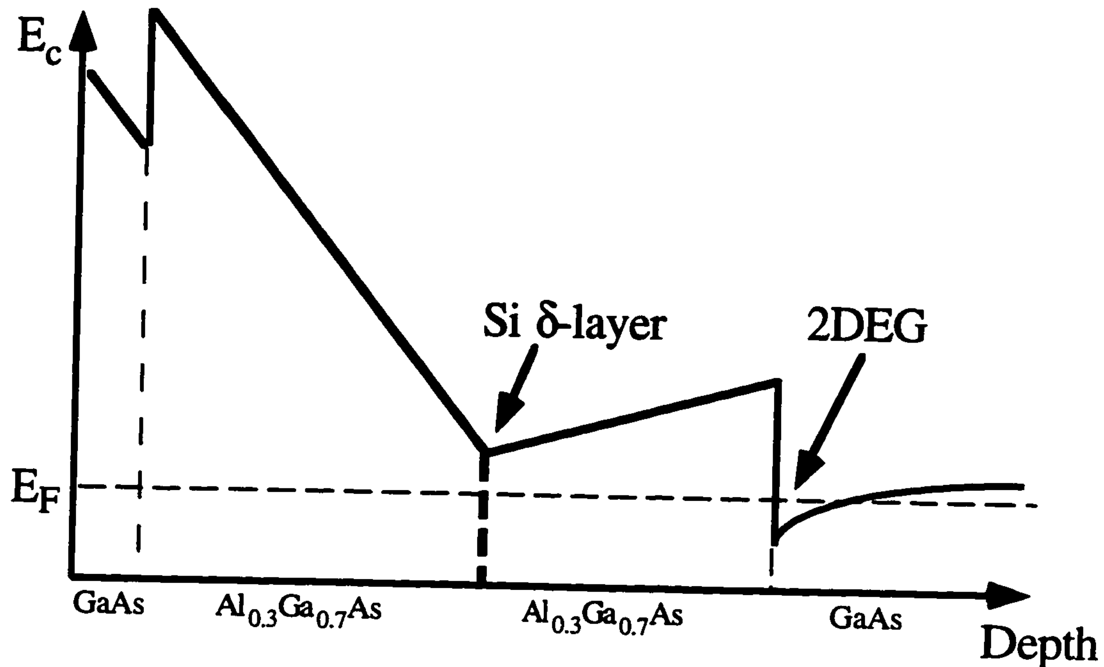

Figure 2-3 Conduction band edge versus depth into heterostructure.

The electrons which fill the surface states in our heterostructures come from the Si donor atoms located in the delta layer several hundred Å beneath the surface.[4] The important physics for understanding the conduction band plot in figure 2-3 is as follows: at the GaAs surface there is a large density of states with energies in the band gap.[5] As a

4. Delta-doping refers to the process of depositing the silicon donors in a single, very thin layer, usually several hundred Å away from any areas which need to contain high-mobility carriers.

5. Although it may sound contradictory that there is a large density of states in the band gap, this is not the case. The term "band gap" refers to the band structure in the bulk material, and the surface has a different electronic structure. Specifically, there are states at the surface with energies in the bulk band gap.

result, the Fermi energy at the surface always lies approximately 0.6 to 0.8 eV below the conduction band edge. The conduction band bends down to a minimum at the location of the silicon donors, where it is pinned by the donor levels (provided there are sufficient numbers of donors in the delta layer). Some of the electrons from the Si delta layer leave the $Al_{0.3}Ga_{0.7}As$ and fall to the lower conduction band level in the GaAs layer. This leaves behind positive Si donors, which attract the electrons and pin them against the interface. The self-consistent solution to this electrostatic problem produces the triangular shaped potential well in which the 2DEG resides, and determines the density of the 2DEG.

The triangular shaped potential well in figure 2-3 which holds the 2DEG will in general have many subbands.[3,6] The well can be sharp enough that only the lowest subband is occupied. To understand the physics of the 2DEG, we can write Schrodinger's equation and assume free electrons in the lateral directions (x and y) and a potential $E_c(z)$ in the growth direction (which would be determined self-consistently, as indicated above):

$$-\frac{\hbar^2}{2m}\nabla^2\Psi(x, y, z) + E_c(z) = E\Psi(x, y, z). \qquad \text{(EQ 1)}$$

6. A subband is a continuum of states, like a normal band, where the energy levels are modified by a potential in addition to that of the lattice. See Eq. 1 and Eq. 2.

The effective mass appropriate for GaAs is 0.067 times the free electron mass. By substituting $\Psi(x, y, z) = \phi_1(x, y)\phi_2(z)$, one finds that the lowest energy solutions are given by

$$E(\vec{k}, n) = E_n + \frac{\hbar^2 k^2}{2m}, \quad \text{(EQ 2)}$$

where $n = 0,1,2,...$ and $\vec{k} = (k_x, k_y)$. In words, the motion in the z direction is quantized, and the motion in the x and y directions is free. At low temperatures the first electron to fall into the well has quantum numbers $n = 0$ and $k_x = k_y = 0$. Increasing the electron density increases $k_F = \sqrt{k_x^2 + k_y^2} = \sqrt{2}k_x$. This process continues until $\frac{\hbar^2 k_F^2}{2m} > E_1 - E_0$, at which point it costs less energy to begin filling the next subband starting with $k = 0$ and $n = 1$. For a heterostructure with $n_s = 3.0\times10^{11}$ cm^{-2}, E_1 - E_0 ~ 34 meV, which is estimated using the Airy function approximation from Harris et al.[7,8] By correctly adjusting the spacing between the interface and the donors, 2DEGs can be obtained in which the only free electrons in the crystal at low temperatures lie in the lowest subband of Eq. 2, i.e. $n = 0$. It is in this sense that the sample contains a *two-dimensional* electron layer, because with only one subband occupied there is no freedom to adjust the *z position* of an electron by changing the composition of its quantum state.

7. J.J. Harris, J.A. Pals, and R. Woltjer, *Rep. Prog. Phys.* **52**, 1217 (1989).

8. J.A. Katine, Ph.D. Thesis, Harvard University (1996).

The 2D electron layer is often called a two-dimensional electron *gas*, because the physics in many situations is well described by a two-dimensional layer of *non-interacting* electrons.

2.1.3 Heterostructure characterization

The heterostructures grown at UCSB are characterized to answer the following questions:

- How many subbands are occupied?
- What is the sheet density of the 2DEG?
- What is the mobility of the electrons in the 2DEG?

These questions can be answered by measuring the Shubnikov-de Haas oscillations in the resistance and the zero field resistance of the sample, both at the low temperatures where our nanostructure experiments are performed.[3]

In the Drude model for electron transport, the conductivity is written as

$$\sigma = \frac{ne^2\tau}{m} = ne\mu, \qquad \text{(EQ 3)}$$

where n is the sheet density, e is the electronic charge, τ is the momentum relaxation time, m is the electron effective mass, and μ is the mobility. A measurement of the resistance of a known geometry, in addition to a measurement of the sheet density n, will determine the mobility μ, and thus the scattering time τ, because

$$\mu = \frac{e\tau}{m}. \quad \text{(EQ 4)}$$

The sheet density is determined by measuring the Hall voltage or by measuring the period of the Shubnikov-de Haas oscillations.[9] We can thus fully characterize the 2DEG with a single Shubnikov de Haas measurement and a measurement of the zero-field resistivity.

2.1.4 Heterostructures used in this research

Heterostructures have been grown at UCSB by Ken Campman, Kevin Maranowski, and Professor Westervelt for work here at Harvard. A summary of these structures can be found in the Ph.D. thesis of Jordan Katine.[8] I have used nearly all of these wafers at some point while working in Gordon McKay Laboratory, but two heterostructures will play a prominent role in this thesis and are summarized in Table 2-2.

TABLE 2-2

	n (cm^{-2})	μ (cm^2/Vs)	Gas Depth (Å)
KC8	3.0×10^{11}	540,000	520
KC9	3.6×10^{11}	510,000	470

2.2 Lithography

The general goal in fabricating nanostructures is to confine the carriers in the 2DEG to narrow channels and small cavities. As discussed in Chapter 1, one of the remarkable

9. The Shubinikov-de Haas oscillations refer to the oscillations in resistance which occur as the Fermi energy passes through various Landau levels as the magnetic field is swept. The Fermi energy will pass through multiple levels because the degeneracy of the Landau levels (including the spin degeneracy) is given by eB/h.[3]

features of mesoscopic physics is that simply confining carriers to small volumes leads to interesting new behavior.

Most of the semiconductor processing techniques which can be used to modify a 2DEG will affect the entire wafer or chip unless some sort of mask is used to modify the process. This is certainly true for the etching and metal deposition processes discussed in the following sections. Lithography is a technique which allows these indiscriminate processes to be selectively applied to portions of a wafer.

Lithography has three steps. First, a resist is spun onto the wafer in a thin layer and allowed to dry. The e-beam resist we currently use is the polymer polymethyl-methacrylate, commonly known as PMMA. Second, the resist is exposed in the desired pattern, usually by light or an electron beam. Finally, the resist is developed, and the exposed region or the unexposed region is removed, depending on whether the resist type is positive or negative respectively. The result is a mask attached directly to the surface, through which etching or metal deposition can be performed.

2.2.1 Electron beam lithography vs. photolithography

For mass production of semiconductor integrated circuits, the lithographic method of choice is photolithography, primarily because it is a parallel process: an entire chip can be exposed simultaneously. For fabrication of research devices the method of choice is electron beam lithography. Electron beam lithography (or e-beam lithography) is flexible because the exposed pattern is determined by modifiable software files, rather

than expensive optical masks. Furthermore, the minimum feature size that is easily obtained in the laboratory is ~ 50 nm for e-beam lithography, much smaller than for photolithography

2.2.2 Spinning resist

E-beam resist needs to be applied to the GaAs surface in a thin, uniform layer. This is accomplished by placing a small drop of PMMA/Chlorobenzene solution on the surface and spinning the chip at high speed. The resist is then baked on a hotplate at 180 °C to evaporate the solvent. In order for the e-beam resist to spin on uniformly and without defects, the wafer surface must be clean and free of particles. To maintain a clean environment, the spinner is located in the inner clean room in Gordon McKay Laboratory. The inner room has a measured particle content of less than $100\left(\frac{0.2\ \mu\text{m sized particles}}{\text{ft}^3}\right)$, i.e. it is class 100, and the outer room is class 10,000.[10] A spinner speed of 4000 rpm will give a layer that is approximately 1000 Å thick if a 2% by weight solution of 950K molecular weight PMMA in chlorobenzene is used, or a 600 Å thick layer if a 2% solution of 495K PMMA is spun at the same speed.

There are three important considerations in choosing which PMMA weight to use in which layer and how many layers to apply. First, lighter molecular weight PMMA exposes at a lower electron dose than higher weight PMMA. Figure 2-4 illustrates the

---

10. Steve, Shepard, personal communication.

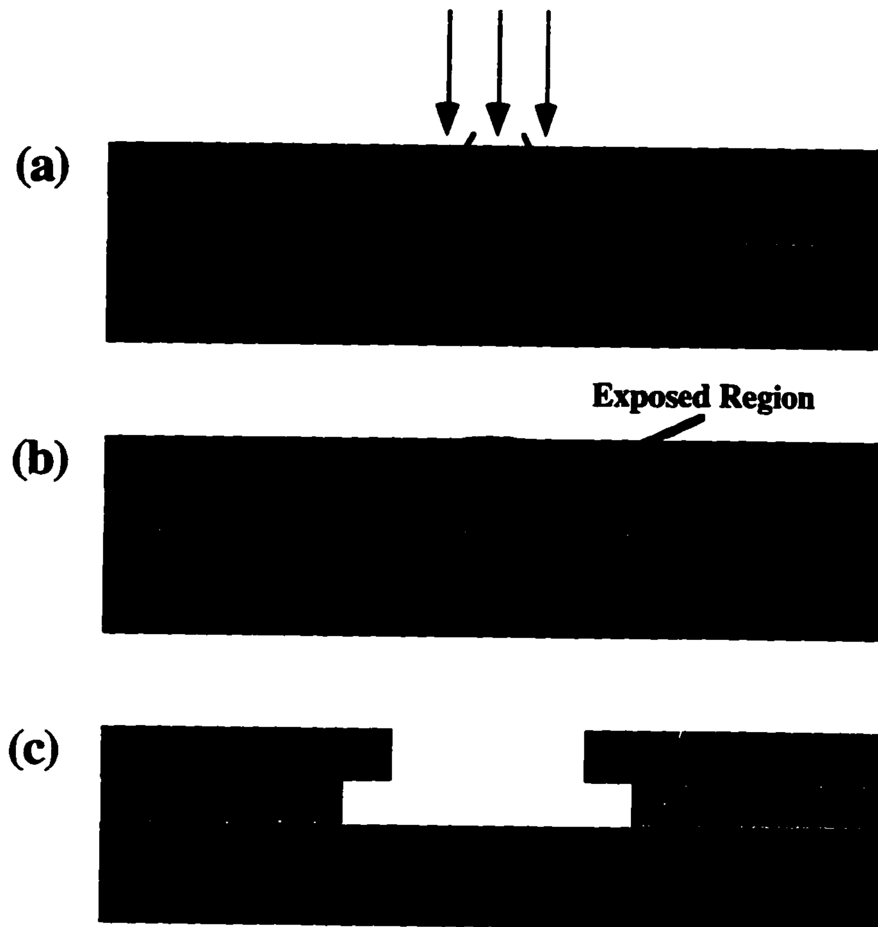

Figure 2-4 Schematic of bilayer PMMA exposure.

exposure of a bilayer of PMMA. When the electron beam hits the PMMA, it begins to spread. When it reaches the surface, which has a high electron density, a substantial electron flux is backscattered, which spreads the beam considerably. This spreading causes an undercut in the developed PMMA. If a bilayer of PMMA is used, with a lighter weight PMMA in the bottom layer, the undercut will be enhanced (figure 2-4).

The second consideration is the thickness of the various layers. If the undercut shown in figure 2-4c is to be effective, the metal evaporated onto the surface must not be thicker than the bottom layer of PMMA.

The final consideration is how many layers to use. When PMMA is baked to evaporate the solvent, it can develop long narrow cracks. These cracks are observed experimentally if a single layer of PMMA is used as a mask for a wet etch. The GaAs chip will have the desired pattern etched into the surface, but it will also have long narrow streaks where the cracks were located. It is possible that metal can be deposited through pinholes in the PMMA found at the intersection of two cracks. If the metal forms ohmic contact to the 2DEG, these contacts can short out gates which are deposited in later processing steps. The hypothesis is that multiple layers will produce cracks in random directions and at random positions. If this is the case, then no holes will form in a trilayer of PMMA (three narrow lines in two dimensions will not intersect at a single point very often). A trilayer of PMMA is therefore recommended for ohmic contact lithography, and a bilayer is acceptable for all other lithographic steps.

2.2.3 Pattern design

Harvard University has a system, known as the Nabity Pattern Generation System, or NPGS,[11] which transforms a JEOL 6400 scanning electron microscope (SEM) into an e-beam writer. NPGS is a software program which runs on a PC equipped with analog

---

11. J. C. Nabity, Lithography Systems, P. O. Box 5354, Bozeman, MT 59717. (406)587-0848

and digital input/output (I/O) boards. The I/O boards allow the PC to communicate with and control the SEM.

There are two software files which determine the pattern that NPGS will cause the SEM to write on the surface: a drawing made with a modified form of the PC application Design CAD®, and a text file, called a *run file*, which tells NPGS the current SEM configuration so that NPGS can issue the correct instructions to the SEM.[12] There are some special formatting rules which must be followed when creating the Design CAD file, but the essence of the process is that the user creates a drawing in which the regions enclosed by lines, rectangles, circles, ellipses, etc. will be exposed to the electron beam in the writing process.

E-beam writing is performed in several stages called layers. The purpose of using multiple layers is that it is easier to write small features on high magnifications and with low beam currents. On the other hand, it would take forever to write the entire pattern with the low beam currents that are appropriate for fine features. Patterns are therefore written from the finest to the coarsest features, increasing the beam current and decreasing the magnification at each subsequent layer.

The beam current is controlled by a setting called the condenser lens (CL). Condenser lens settings range from 1 to 16, with CL1 yielding the largest current as well

---

[12]. DesignCAD® is a registered trademark of American Small Business Machines, Inc.

as spot size, and CL16 yielding the smallest current and spot size. It is important to note that there is a limit to the method of increasing pattern writing speed by increasing the beam current: at beam currents above CL4 this process does not reduce writing time. Apparently at large point spacings the dose must be increased so that the regions between points receive sufficient scattered electron flux to expose the PMMA. There is a threshold at CL4, such that above that beam current the increase in the required dose exceeds the time saved by using an increased beam current. For this reason, it is not useful to use condenser lenses 3, 2, or 1 for e-beam writing.[13]

It is possible to check in advance that the pattern will write properly by hooking up the SEM control voltages to the storage scope next to the SEM. Writing the pattern on the scope will allow errors which crash NPGS to be found and easily located. This simple step can save substantial time if even one error in a new pattern is caught by this process.

2.2.4 Sample mounting

Sample mounting is important because the focus of the SEM will be maintained over the entire chip only to the extent that the chip is mounted flat on the sample slug. The slug is about 1 cm in diameter. The GaAs chip is attached to the slug by allowing carbon paint to run around its edges. There are substantial differences in procedure from student to student at this stage,[8,14] but all the methods seem to work well. My technique

---

13. An additional consideration is that the beam currents on the condenser lenses 3, 2, and 1 are less stable than the currents on the higher condenser lenses.

is to use very thin carbon paint so that it runs around the whole chip and underneath as well. The sample slug I use has ridges on its surface so that the carbon paint running beneath the sample does not seem to tilt the sample. This method avoids the possibility of bumping the chip with an applicator, which almost always requires starting the process over after cleaning the chip in isopropyl alcohol.

The last stage in sample mounting is to place small blobs of silver paint on the surface of the PMMA to allow focusing of the electron beam. Silver has a very large electron density, so it provides good contrast in the SEM. The goal in applying the silver paint is to leave numerous micron-sized silver chunks directly on the PMMA surface, not in the middle of a big glob of silver paint.

2.2.5 Writing the pattern on the SEM

The process of writing the pattern on the PMMA covered GaAs chip involves stepping the electron beam from spot to spot on the sample surface, delivering a precisely known dose at each location. To achieve this result quickly, the beam is always "on" at a specified current, and the computer controls a fast shutter to blank the beam as the SEM lenses move the beam to the location of the next spot. All of these steps are controlled by the computer; it is up to the user to set the correct beam current, to ensure the beam is tightly focused at the sample surface, and to align the sample. Coarse alignment of the sample is achieved by locating the four corners of the chip and

---

[14]. For an alternative method see C. L. H. Crouch, Ph.D. Thesis, Harvard University (1996).

positioning them by moving the micrometer controlled stage by hand. If fine alignment is necessary, it can be accomplished electronically using the NPGS system. A detailed set of instructions for e-beam writing can be found in Catherine Crouch's Ph.D. thesis.14

2.2.6 Developing the sample

Once the sample has been written, the final step in the lithography is to develop the PMMA. For the positive PMMA resist we commonly use, developing removes the resist in the region which has been exposed to the proper dose by the electron beam.

The sample is removed from the SEM slug by pushing laterally with the smooth edge of a pair of tweezers. The sample is then placed in the developing solution for 60 seconds, after which it is immediately transferred to a beaker of isopropyl alcohol for a similar length of time. The developing solution is mixed with the following ratios: 6.5 ml MEK, 125 ml MIBK, 375 ml IPA.[15] If parts of the sample are not fully developed after 60 seconds, the chip can be placed in the developer again. This does not seem to degrade the fine features, at least for another minute or two.

2.3 Evaporation and wire-bonding

One of the most common processing steps in nanostructure fabrication is the deposition of thin metal films on the substrate surface. In order to deposit the metal in

15. The abbreviations stand for the following chemicals: MEK = 2-butanone, MIBK = 4-methyl 2-pentanone, and IPA = isopropyl alcohol.

the correct locations, lithography is performed and windows are opened in the PMMA resist. The metal is then deposited through this mask in the desired pattern.

2.3.1 Evaporation and liftoff

For a number of years, all of the evaporations for semiconductor nanostructure fabrication had been performed in a general purpose thermal evaporator in the outer clean room. Because of an increasing number of users for that machine and a desire to have a "cleaner" evaporator dedicated to the evaporation of a few select metals (Au, Cr, Al), a new evaporator was purchased in November of 1996. The older evaporator is still used for the evaporation of other materials, such as gold, nickel, and germanium ohmic contacts (see section 2.4). I have made samples in both evaporators. The two evaporators are similar, and I will describe the new evaporator here, as previous students have described the old evaporator in detail.[8]

Figure 2-5 is a schematic of the new thermal evaporator. The evaporation occurs in a large bell jar which has been evacuated to a pressure of several $x10^{-7}$ torr; the exact pressure does not seem critical. One of the primary advantages of the new evaporator is that it is pumped by a cryopump, rather than a diffusion pump. The cryopump does not need a liquid nitrogen jacket; it is inherently cleaner; and it is much faster than a diffusion pump. The large bell jar can be evacuated to $2x10^{-7}$ torr in about one hour — roughly three times as fast as the old diffusion pumped evaporator.

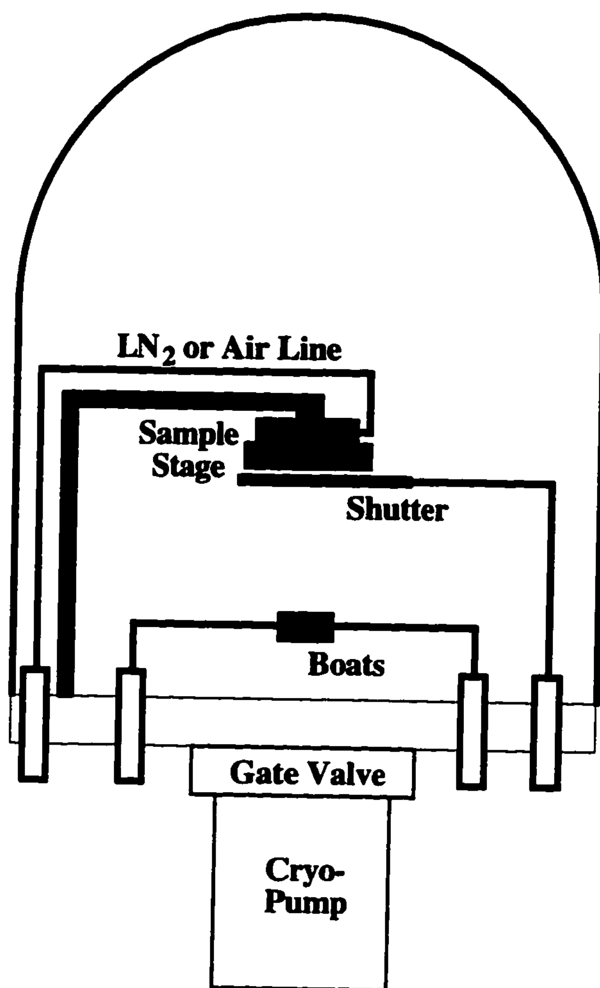

Figure 2-5 "New" cryopumped thermal evaporator.

Figure 2-5 also shows the various feedthroughs which provide access to the vacuum space. The most important feedthroughs are the current leads for the three sets of evaporation posts, the rotary feedthrough for the shutter, and the pipes which carry air or liquid nitrogen to the sample stage. Our samples are mounted on a metal stage with carbon paint, and the stage is bolted to the evaporation platform in the vacuum space.

The elements to be evaporated are placed in boats beneath the sample. Large currents are run through the boats until the vapor pressure from the hot metal is such that approximately 1 Å/s of material is deposited at the sample height. The deposition rate is monitored using a standard crystal monitor positioned near the sample. A shutter is controlled manually to start and stop the deposition on the sample. The following are some tips for evaporating metals onto GaAs:

1. Immediately prior to the evaporation, dunk the sample in a 1:5 mixture of ammonium hydroxide (NH_4OH):water, for approximately 5 seconds. Then blow the sample dry without rinsing it in any solvent. This step greatly increases the adhesion of the metal to the GaAs surface.[8]
2. The stage should be cooled with liquid nitrogen. This seems empirically to help the liftoff. It has also been shown by Carol Livermore to reduce the tendency of Cr to ball up on the surface, presumably by reducing surface diffusion.

Once the evaporation has been completed, the next step is to perform "liftoff", a process which removes the PMMA and unwanted metal. Figure 2-6 (a) is a diagram showing the ideal profile of the PMMA and metal after an evaporation. At this point the GaAs chip and its PMMA/metal overlayer are placed in a beaker of acetone and allowed to sit for a period of time. The sample should sit from one to twelve hours, depending on how quickly that particular sample lifts off. After soaking in acetone until the surface looks wrinkled, the liftoff technique I prefer is to ultrasound the chip in its acetone bath for about 5 seconds — the beaker containing the acetone and the sample can be placed directly in the ultrasound. The sample is then placed in a petri dish filled with acetone so that it can be viewed under a microscope. If inspection shows the liftoff is complete, the sample can be placed in a beaker of methanol and then blown dry with the nitrogen gun.

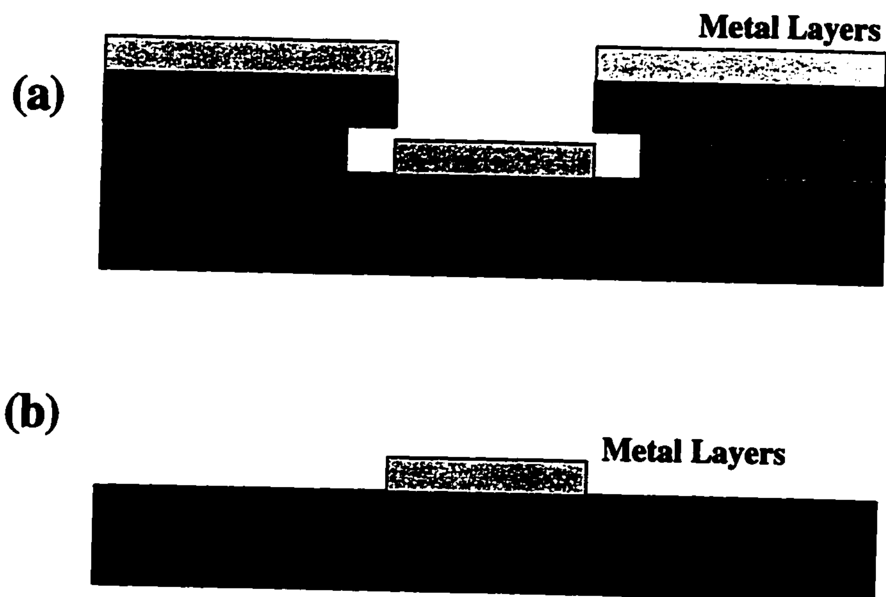

Figure 2-6 Evaporated metal and liftoff.

Figure 2-6 (b) shows the profile of the metal once liftoff is complete. If the liftoff is incomplete, the chip is placed in a new beaker of acetone (the original is usually filled with little pieces of metal) and placed in ultrasound for 30 seconds. This process should be repeated, with new acetone only as needed, until the sample looks good under the microscope.

2.3.2 Wirebonding

In order to make electrical measurements on the sample, it is necessary to attach wire leads. Figure 2-7 is a photograph of a completed sample, mounted in a chip carrier, with gold wires bonded between the chip and the chip carrier. In order to make measurements the chip carrier is placed in a socket, which has pins to make electrical contact to the pins on the chip carrier.

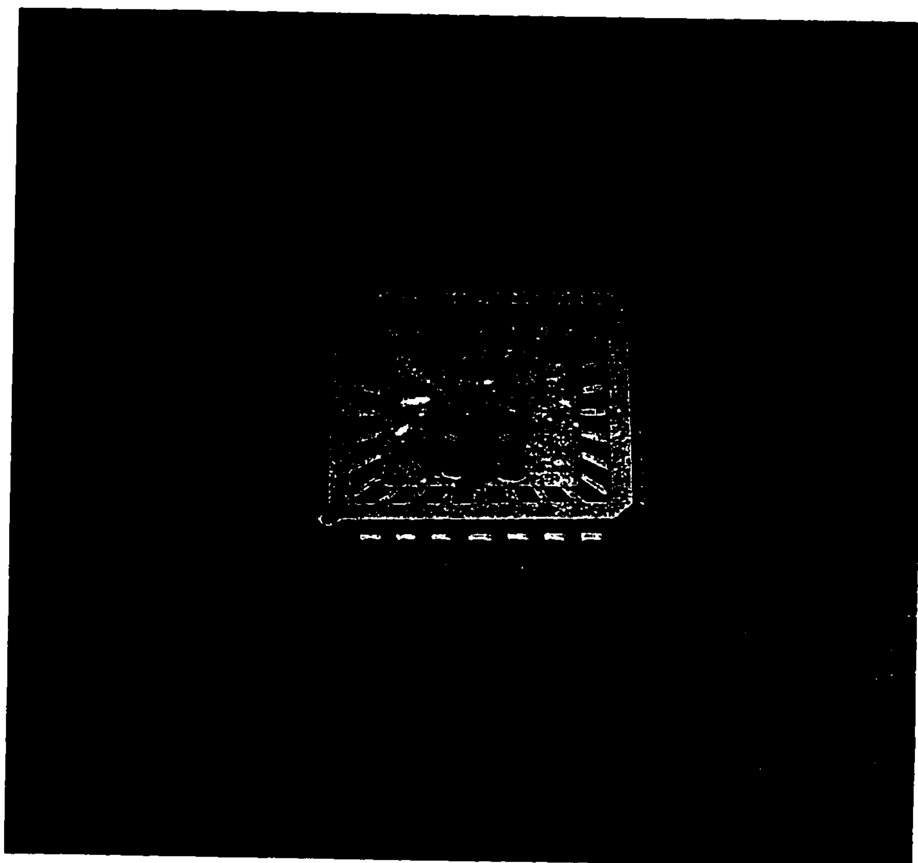

Figure 2-7 Photograph of a completed sample wirebonded into a chip carrier. The width of the chip carrier is approximately 1/2 inch.

The wirebonds are made with the help of a machine in the outer clean room that is creatively named the wirebonder.[16] Figure 2-8 shows a diagram of the essential working parts of the wirebonder. A 1 mil gold wire is looped under a piece called the "foot." The foot presses the wire into the surface and vibrates with a strength that the user can control. This creates a micro-weld between the wire and the surface beneath. Gold wires can be bonded to other types of metal, like aluminum, but gold bonds most

16. Kulicke-Soffa model 4123.

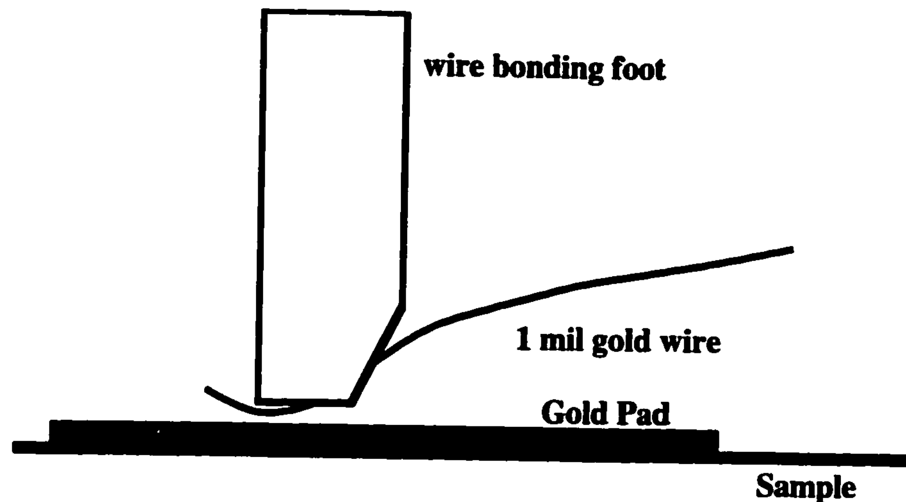

Figure 2-8 Wirebonding foot.

easily to gold. The wirebonder is a well engineered piece of equipment, and it handles all of the details like trimming the wire in an automated and convenient manner.

There are two failure modes in wirebonding gold wires to gold pads on GaAs. The first is that the gold wire may not stick to the gold pad. This is almost always due to a dirty surface, and the sample can simply be cleaned in acetone and methanol. The second failure mode is that the wire will bond to the pad and then rip it up off the surface. This situation is more difficult, because the cause is a lack of adhesion between the pad and the surface, and it is too late to fix that. The problem is almost always avoided by dunking the chip in ammonium hydroxide prior to evaporating the metal pads (see section 2.3.1). Both of these problems can sometimes be fixed by tuning the settings on the wirebonder, such as the duration of the bonding, the force with which the foot pushes on the surface, and the power supplied to drive the vibration of the foot.

2.4 Ohmic contact to the 2DEG

One method to make electrical contact to the 2DEG, which is typically 500 Å beneath the surface, is to press indium metal onto the surface of the chip. The chip is then heated and the metal diffuses into the heterostructure and contacts the 2DEG.[17] This was the procedure when I first started doing research in the Westervelt group. This process was time consuming, and, even worse, the indium blobs would frequently fail to make electrical contact to the 2DEG.

It has been known for some time that a very reliable method for making ohmic contact to GaAs wafers is to replace the indium with an alloy of gold, nickel, and germanium (Au/Ni/Ge).[18] There was a general reluctance in the group to make this change, because the old process of attaching wires to any part of the GaAs chip was to use indium (which is very malleable) as a kind of putty to hold the wire to the chip. Using an evaporative procedure like Au/Ni/Ge contacts would simply require indium to be placed over the Au/Ni/Ge contact, which seemed a little redundant. Catherine Crouch and I eliminated this concern by showing that the wirebonder in the outer clean room worked well with our GaAs heterostructures, and Rex Beck and Carol Livermore demonstrated that the Au/Ni/Ge process did indeed make good electrical contact to the 2DEG.[19] Au/Ni/Ge contacts and wirebonding is now the method of choice in the Westervelt group for making electrical contact to the 2DEG.

---

17. For details on this process, see D.J. Mar, Ph.D. Thesis, Harvard University (1994).

18. For a discussion of contacts to semiconductors see Dieter K. Schroder, *Semiconductor Material and Device Characterization*, John Wiley and Sons (1990).

Figure 2-9 is a schematic of the evaporated layers of metal which form the ohmic contact to the 2DEG. The metal layers need to be heated so that they will mix and diffuse into the semiconductor. A strip heater is used to anneal the contacts.[20] A thermocouple is spot-welded to the back side of the strip heater to monitor the sample temperature. The chamber holding the strip heater is closed during the annealing, and a flow of forming gas (80% Helium and 20% Hydrogen) is maintained throughout the process. The procedure for annealing contacts is as follows:

- Place chip on strip heater, close chamber, and flow gas for at least 60 seconds.
- Heat chip to 110 °C by adjusting the voltage across the strip heater with the variable transformer — hold at this temperature for 60 seconds.
- Heat chip to 260 °C — hold for 10 seconds.
- Heat chip to 400 °C — hold for 20 to 25 seconds.
- Allow to cool to near room temperature (30 – 40 °C).

The times quoted do not include the time necessary to achieve the given temperature: begin timing when the temperature is within approximately 10% of the desired value. The length of time necessary at 400 °C depends on the size of the chip. The contacts

19. All of these processes have been used for years in the semiconductor industry. Demonstrating them here was simply a matter of showing that the equipment worked as it should and alleviating concern that this "new" technology would somehow ruin the good luck which allows experiments to be successfully completed! To be fair, such caution is warranted: there is nothing worse than having a working experiment delayed by rushing too quickly into a change which will be convenient in the long run but which is unnecessary at the time. This is one of the trickiest balances in a research project: to know when to invest in infrastructure for an experiment, and when to get the job done quickly.

20. Constructed by Alex Rimberg. See A.J. Rimberg, Ph.D. Thesis, Harvard University (1992).

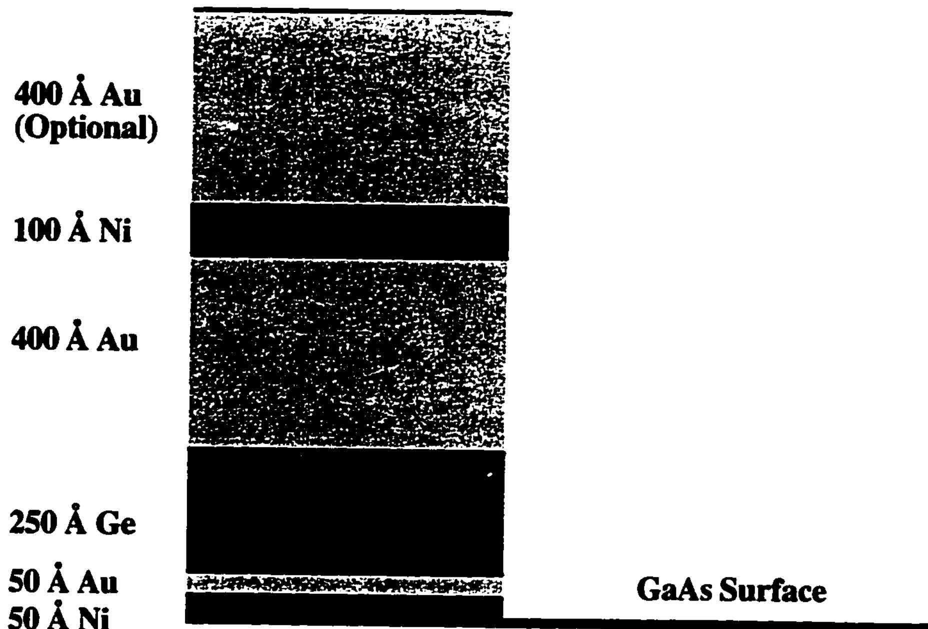

Figure 2-9 Schematic of evaporated layers for forming ohmic contact to the 2DEG.

will work almost without fail if when viewed under a microscope they resemble the surface of the moon. If the surface still looks smooth under magnification, repeat the above procedure. It does not seem possible to "overbake" a Au/Ni/Ge contact, as long as the depth of the annealed contact is not a serious concern.

The contacts can be tested by wirebonding to the contacts, dunking in liquid helium, and measuring the resistance between contacts. A typical 2DEG will have a resistance per square of 42 Ω for a wafer with sheet density $n = 3.0 \times 10^{11} \mathrm{cm}^{-2}$ and mobility $\mu = 500,000 \frac{\mathrm{cm}^2}{\mathrm{Vs}}$. Typical contact resistances are a few tens of ohms.

2.5 Lateral confinement of the 2DEG

The fabrication techniques discussed in the above sections are used to laterally confine the two-dimensional electron gas in order to make interesting mesoscopic devices. These devices can have a wide variety of shapes, and it has become a field in itself to explore the physics of microstructures of different sizes and shapes. The purpose of the work reported in this thesis is to develop a new technique for studying mesoscale devices, and we have therefore chosen to look at one of the simplest mesoscale devices, the point contact. The two methods which are generally used to confine the 2DEG, and which I have used to make the samples studied here, are surface gates and mesa etches.

2.5.1 Surface gates

One of the most flexible confinement techniques is to use surface gates. When a negative voltage is applied to the surface gates, electrons are transferred from the 2DEG to the surface gates, just as in a parallel plate capacitor. Applying a sufficiently large negative voltage, the depletion voltage, completely depletes the carriers in the 2DEG region beneath the gate.

The recipe for creating surface gates used in our research group is to evaporate approximately 100 Å Cr followed by 300-400 Å Au, and then to perform liftoff, as discussed in section 2.3.1. The Cr layer prevents the Au from diffusing into the surface and improves the adhesion of the metal layers to the GaAs surface.

Figure 2-10 (a) is an SEM micrograph of a sample consisting of an array of twelve point contacts fabricated in wafer KC9. As shown in figure 2-10 (b), the current flows from left to right across the sample. The sample shown is an array of one dozen point contacts in series. In order to understand the micrograph, it is simplest to consider the light regions, which are the Cr and Au gates, as the regions with no electrons beneath them. The dark regions are the surface of the GaAs chip, and beneath those regions there are free carriers in the 2DEG. The twelve arms extend all the way to the edge of the chip, so that applying the depletion voltage to any single arm will divide the chip into two reservoirs joined by a narrow point contact, as shown in the micrograph.

The purpose of creating this array of point contacts was to make alignment of the AFM easier at low temperatures (see chapter 6). The many small icons to either side of the point contact array also help in the alignment process.

2.5.2 Mesa etches

Another common technique for carving a 2DEG into a useful geometry is to use mesa etches. Figure 2-11 is a schematic diagram of an etch trench in a GaAs heterostructure. In this case the trench is deep enough that it cuts completely through the 2DEG. An important point is that the exposed surfaces in the etch trench contain surface states, just like the heterostructure surface. This causes a depletion region to extend into the semiconductor chip, as shown in figure 2-11. The etch trenches do not have to extend through the 2DEG: if the trench comes close enough to the donors to draw all of the

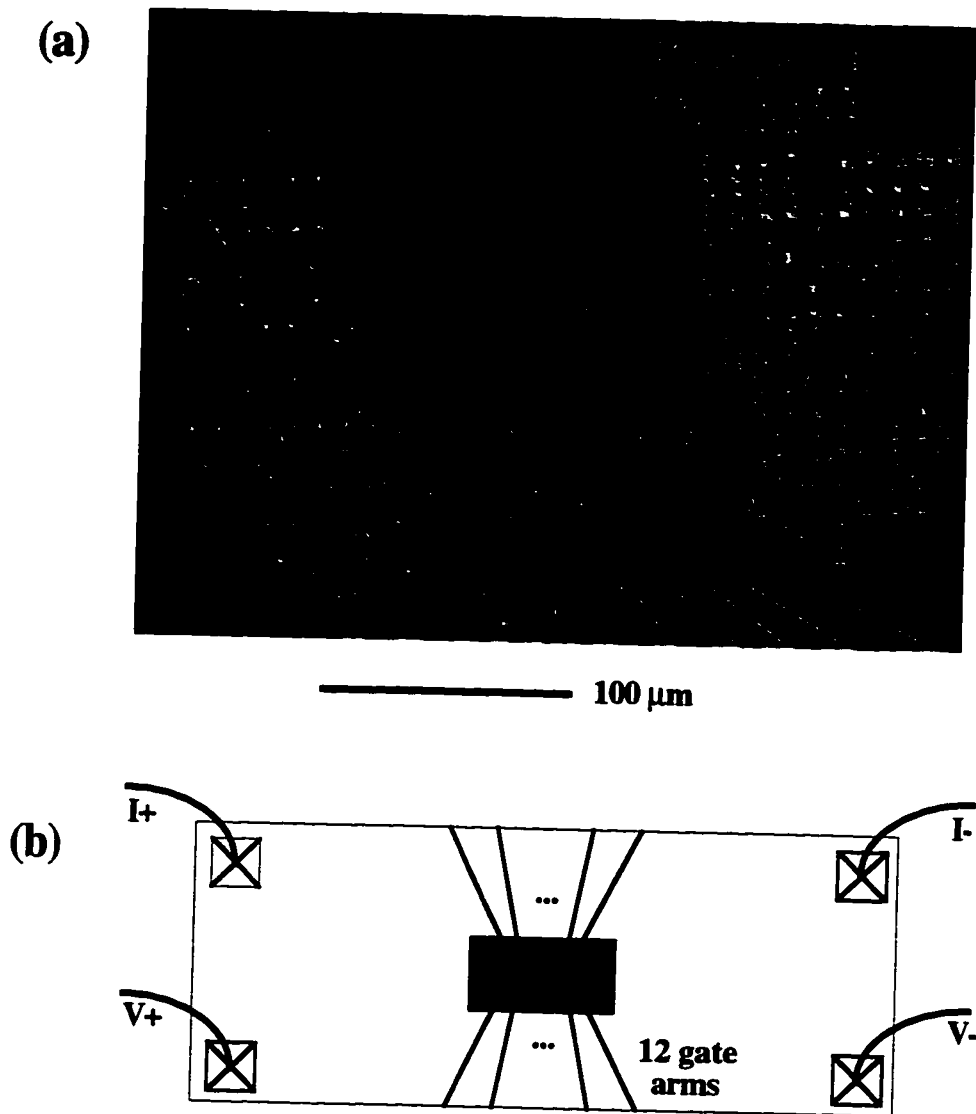

Figure 2-10 (a) SEM micrograph of an array of point contacts.
(b) Schematic of the sample. The gray square indicates the position of the micrograph in part (a).

carriers into the surface states, or if the etch trench simply removes the donors themselves, then there will be no 2DEG at the GaAs/AlGaAs interface.

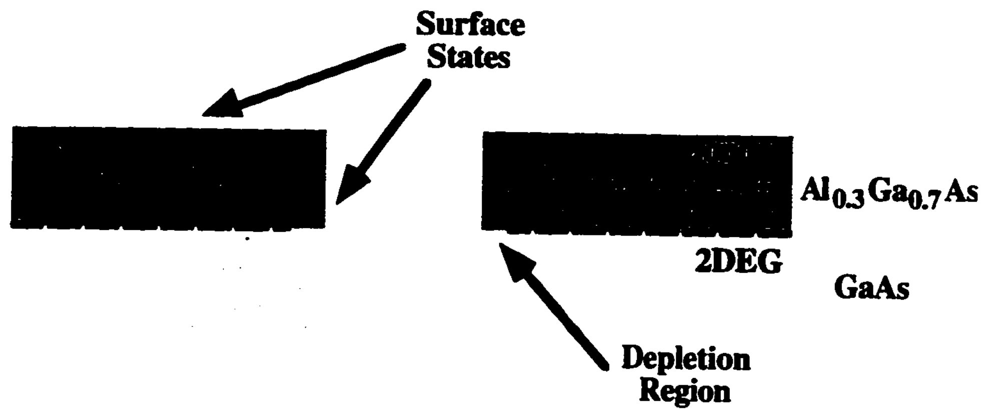

Figure 2-11 Schematic of an etch trench in GaAs/AlGaAs Heterostructure.

Figure 2-12 shows an AFM topographic image of a point contact fabricated from wafer KC8. The darker region is the etch trench, which is lower in this image. The etch trench divides the chip into two reservoirs connected by a narrow point contact. In this case the point contact is 2.9 μm wide, instead of 100 nm wide for the gated point contacts of figure 2-10. Many of the data scans in chapter 5 were taken on this sample.

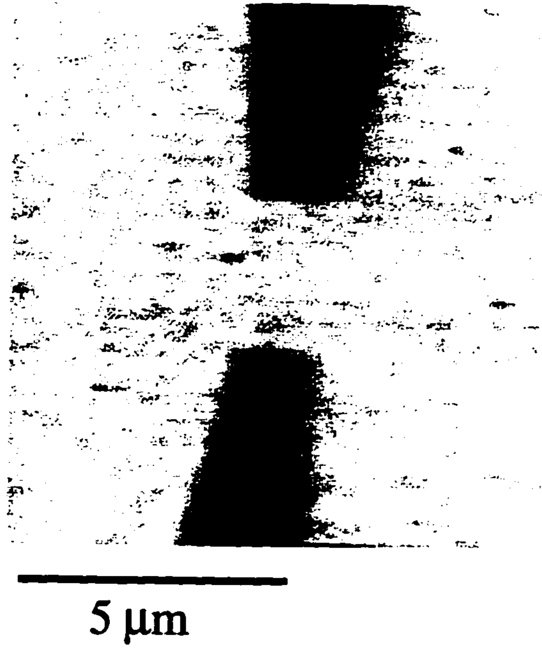

Figure 2-12 AFM image of an etched point contact in sample KC8-F.

CHAPTER 3

A scanning probe microscope for low temperature mesoscopic physics

A major part of this thesis research project was the design and construction of a scanning probe microscope appropriate for studying semiconductor nanostructures. This chapter provides a detailed description of the scanning probe microscope we designed and built for studying nanostructures, and which was used in the experiments reported in chapter 5.

3.1 Overview of scanning probe microscopy

Since its introduction in 1982, scanning probe microscopy has spread rapidly through not just the surface physics community, but throughout much of condensed matter physics, chemistry, biology, and many other fields. This section gives a brief overview of the

history and concepts of SPM technology. There are a number of books which give an excellent review of this very large field.[1,2]

3.1.1 History and operating principles

The scanning tunneling microscope (STM) was invented by Binnig and Rohrer in 1982, and is shown schematically in figure 3-1.[3] Although the STM can make many measurements, its primary purpose is to measure the microscopic surface topography of a sample. The success of the STM in this role is astounding: STMs can image the atomic structure of surfaces ranging from metals such as gold to semiconductors such as silicon; both the vertical resolution of an STM and its lateral resolution are subatomic. The STM has become the prototypical example of the general class of instruments known as scanning probe microscopes (SPMs).

Figure 3-1 (a) shows the interaction between the tip and the sample in an STM. The principle of the STM is that by applying a voltage between a sharp tip and a conducting sample, a tunneling current will flow between the tip and the sample. The unparalleled resolution of the STM is due to the exponential dependence on distance of this tunneling current.

---

1. R. Wiesendanger and H.-J. Güntherodt, eds., *Scanning Tunneling Microscopy II*, Springer-Verlag, New York (1995).
2. C. Julian Chen, *Introduction to Scanning Tunneling Microscopy*, Oxford University Press, New York (1993).
3. G. Binnig, and H. Rohrer, *Helv. Phys. Acta.* 55 (1982).

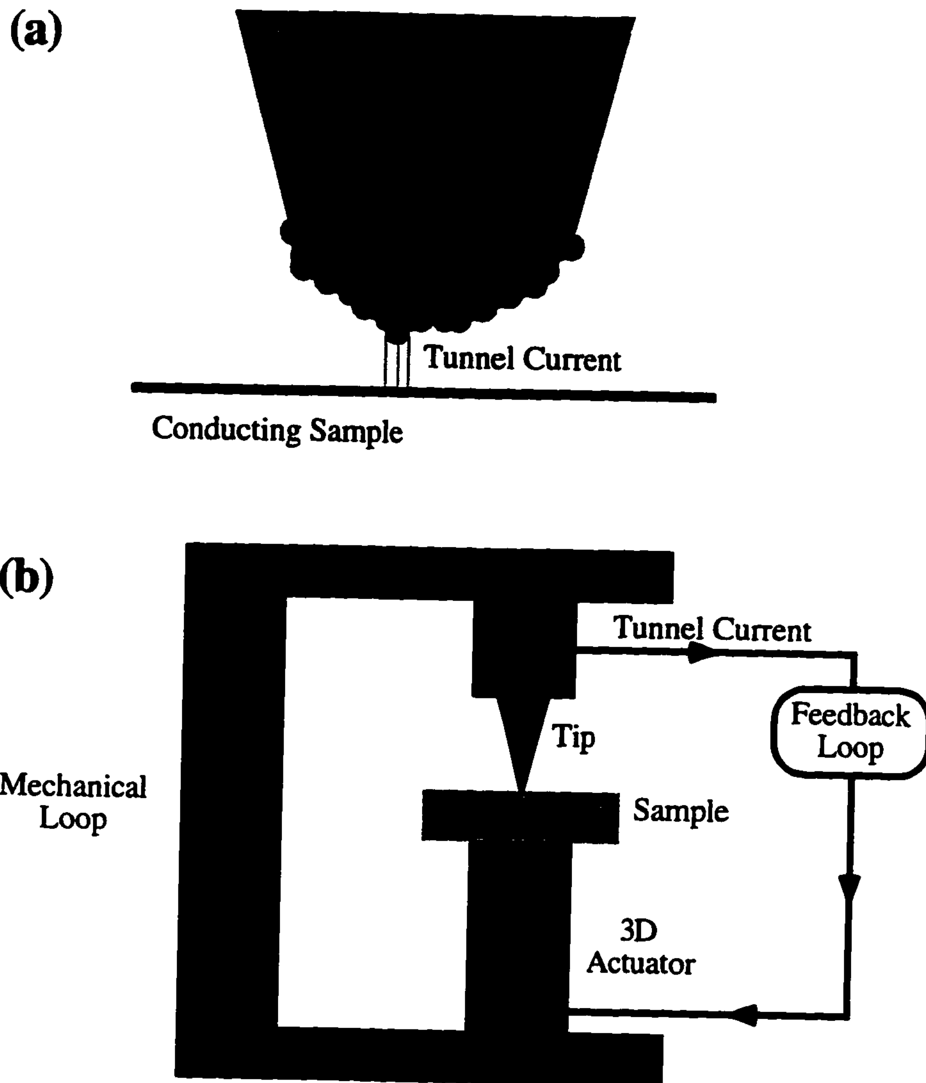

Figure 3-1 Schematic diagram of the scanning tunneling microscope.

Figure 3-1 (b) indicates the mechanical loop and feedback loop which make the STM work. The tip-sample voltage is held constant, and the tunnel current is measured. As the sample is moved in a raster scan, the feedback loop adjusts the height of the sample such that the tunnel current is held constant. Because the tunnel current depends

predominantly on the tip-sample distance, recording the height of the sample as it is scanned beneath the tip produces an accurate profile of the sample surface.

The STM works well only when the sample to be imaged is conducting. It also only probes the electronic density of states. A desire to image insulating samples, and to study properties besides the electron density of states at surfaces, has resulted in the development of a myriad of other scanning probe technologies. All of these microscopies follow the same general feedback scheme shown in figure 3-1 (b). Figure 3-2 illustrates the concept of a general scanning probe microscopy. In all cases, some type of localized tip, known as a proximal probe, interacts with a sample surface. When the sample is scanned, data is recorded at each position, and an image is created.

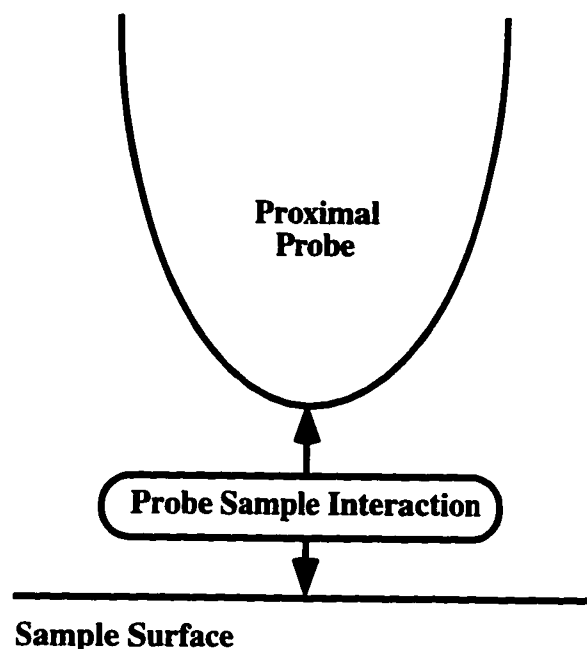

Figure 3-2 General scanning probe techniques.

Table 3-1 summarizes some of the more well known scanning probe techniques. All of these microscopies replace the tunnel current interaction in the feedback loop of figure 3-1 (b) with a different type of local interaction between the tip and the sample.

Microscopy	Probe	Measurement Technique
STM	Sharp Conducting Tip	Tunnel Current
AFM	Sharp Tip (Conducting or Insulating)	Laser Beam Deflection
		Interferometric Techniques
		Capacitance
		Piezoelectric Charge
		Piezoresistive Effect
SCM	Sharp Conducting Tip	ac Current
		Force (any AFM technique)
		Charge
SKPM	Sharp Conducting Tip	same as SCM
NSOM	Coated Optical Fiber	Scattered Light

TABLE 3-1 A few widely recognized scanning probe microscopies.

STM = scanning tunneling microscopy
AFM = atomic force microscopy
SCM = scanning capacitance microscopy
SKPM = scanning Kelvin probe microscopy
NSOM = near-field scanning optical microscopy

The most widely implemented and most important scanned probe technique for our work is the atomic force microscope, or AFM. The AFM was invented in 1986 by Binnig, Quate, and Gerber,[4] in order to image nonconducting samples. Atomic force microscopy replaces the tunnel current interaction with the van der Waals interaction

---

4. G. Binnig, C. F. Quate, and Ch. Gerber, *Phys. Rev. Lett.* **56**, 930 (1986).

between a sharp tip and the sample surface. Instead of measuring a current, AFMs measure a deflection caused by the van der Waals force. Perhaps because of the non-exponential nature of the interaction, the resolution of AFM images is not generally as good as STM images. AFMs, however, have an enormous advantage over STMs in that they can image any relatively flat sample — regardless of whether the sample is insulating or conducting.[5] Even though its resolution cannot compete with the STM, the resolution of AFMs is nonetheless near atomic, and some true atomic resolution scans have been achieved.[6]

Table 3-1 lists examples of different types of atomic force microscopes. The difference between each of them is simply the method for sensing the deflection of the tip. Figure 3-3 illustrates one example, the fiber interferometer method. In all AFMs, a sharp tip is mounted on or fabricated at the end of a cantilever beam. The cantilever beam is usually 100–200 μm in length, and its typical spring constant is 1 N/m. In the contact mode, which is important for this thesis, the cantilever is brought into close proximity with the surface so that it deflects due to the van der Waals force between the tip and the sample. The van der Waals force depends primarily on the tip–sample distance, so maintaining a constant deflection while scanning the sample will produce a topographic map of the surface.

---

5. For a review of AFM techniques see C.F. Quate, *Surface Science* **299/300**, 980 (1994), and Daniel Rugar and Paul Hansma, *Physics Today* **43**, 23 (1990).

6. Without entering into the debate itself, since our work concerns length scales much larger than the atomic scale, it is worth noting that atomic resolution usually refers to the ability to measure atomic scale defects in the crystal lattice, not just the ability to extract the underlying lattice periodicity.

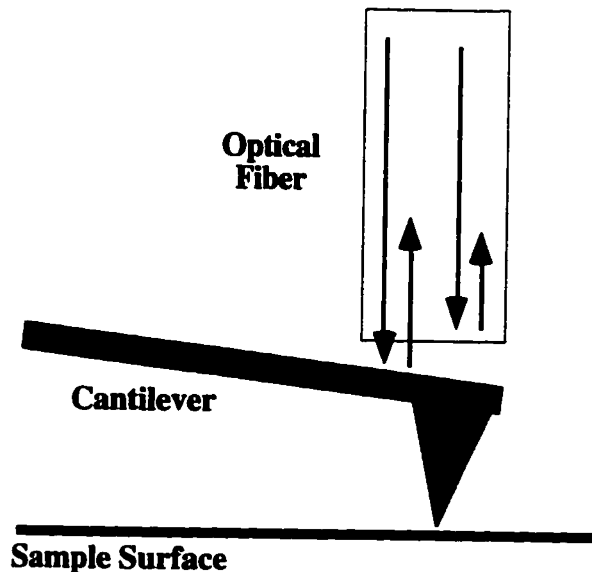

Figure 3-3 Fiber interferometer AFM technique.

In the fiber interferometer case shown in figure 3-3, the cantilever deflection is measured relative to the fixed end of the optical fiber. The cleaved end of the fiber, which is partially reflective, serves as the reference arm for the interferometer. The other arm of the interferometer also traverses the optical fiber, but its end is the top side of the AFM cantilever. As the gap between the fiber and the sample is varied, the interferometer fringes shift. Although intuition might lead to the assumption that the distance which can be measured by this method is of order the wavelength of the light, this is not correct. In practice it is very easy to measure small shifts in fringe intensity, simply by using a photodiode. In terms of deflection noise levels, the fiber interferometer is one of the best AFM deflection sensors available. Root mean square

noise levels of 0.005 $\text{Å}/\sqrt{\text{Hz}}$ have been achieved above 1 kHz with an all–fiber version of this method.[7]

The first scanning probe microscope I built used an all-fiber interferometer as its deflection sensor. Figure 3-4 is one of the first images taken with that microscope, and I reproduce it here as an example of the imaging capabilities of an AFM. The sample in this case is a quantum dot fabricated in a GaAs/AlGaAs heterostructure. The height of the Cr/Au gates which form the dot is approximately 500 Å, and the inner diameter of the dot is about 1 μm. It was a desire to work towards imaging the transport properties of this type of microstructure which led us to perform the experiments on point contacts which are reported in this thesis.

It is beyond the scope of this thesis to explain all of the techniques listed in figure 3-2 in detail. In fact, there are many more scanning probe techniques besides the examples listed, and more are invented every year. See the reviews previously mentioned for more information on these techniques.[1,2]

3.1.2 Goal of our research

The goal of this thesis research is to image spatial variations in the electronic properties of mesoscopic samples. Because of the flexibility of scanned probe techniques, we chose to develop a special type of scanning probe microscope which would allow us to make these measurements. The SPM would consist of two parts: an

7. T. R. Albrecht, et al., *Ultramicroscopy* **42-44**, 1638 (1992).

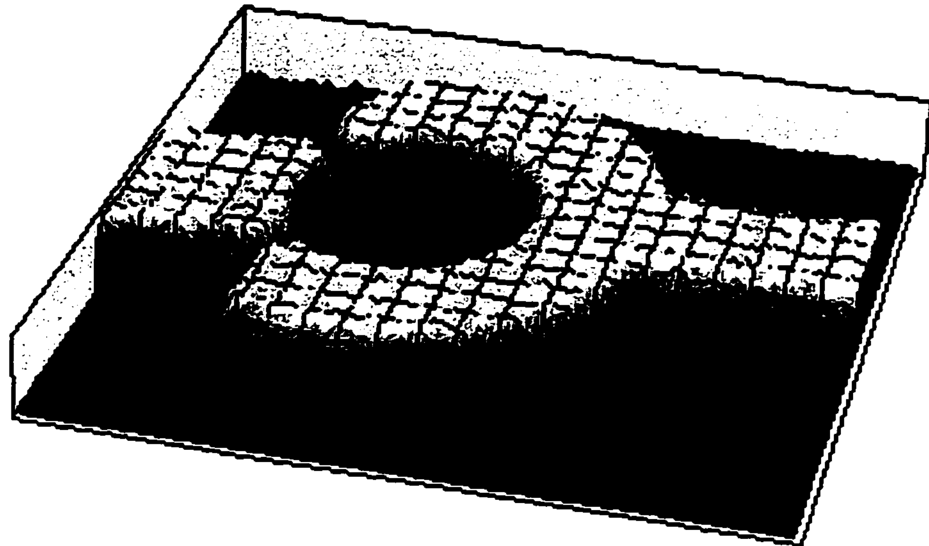

Figure 3-4 Room temperature AFM image of the metal gates forming a circular quantum dot. The inner diameter of the dot is 1.0 μm.

atomic force microscope, so that we could image the device topography and align to the nanostructure, and an additional microscopy, which would allow electrical measurements on the sample. The additional microscopy which we have developed uses the conducting SPM tip in our instrument as a mobile surface gate. There were a number of requirements which we needed to fulfill in order to study mesoscale 2DEG devices:

- The instrument needed a long range in order to find and study micron size samples.
- The SPM had to work at liquid helium temperatures, so our nanostructures would be

in the mesoscopic limit (i.e. long mean free path, long phase coherence time, degenerate electron gas, etc.).

- There could be no photoexcitation of carriers in our samples.
- The tip had to be conducting, and we needed electrical contact with it so that we could couple electrostatically to the 2DEG.
- The electromagnetic environment of the sample had to be cold and free of noise.
- The sample had to have numerous electrical leads attached to it.

The purpose of this chapter is to describe the design we used to meet these requirements, and to give a detailed explanation of how our SPM works.

3.2 Deflection sensors

The method used to detect the deflection of an AFM cantilever determines to a large extent how the entire instrument will be built. I have used two types of deflection sensors in SPMs that I have built at Harvard. The first SPM I built used an all–fiber interferometer. This method is not desirable for studying semiconducting samples because stray light from the interferometer can induce changes in the carrier densities in the sample. Nonetheless, building that instrument taught me a lot about scanning probe microscopy, and the all–fiber interferometer remains in working order. It was described briefly in section 3.1.

The main deflection sensors which I have used to study mesoscopic samples are piezoresistive cantilevers, which are now commercially available from Park Scientific Instruments.[8] These cantilevers are very well suited to our application of scanning probe microscopy to the study of semiconductor nanostructures.

3.2.1 Piezoresistive cantilevers

In 1993 Marco Tortenase and collaborators at Stanford University fabricated a new type of cantilever which provided an integrated method for sensing the cantilever deflection.[9] Their cantilever was made of p–type silicon, which is piezoresistive. The deflection of their cantilever could be obtained by measuring the resistance of a current path through the cantilever. This type of cantilever is now manufactured and marketed by Park Scientific Instruments under the brand name piezolevers.®

Figure 3-5 (a) is a schematic diagram of the cantilever cross–section. The cantilever is fabricated using several silicon processing steps, and the details can be found in Marco Tortenase's Ph.D. Thesis.[10] An important point for our work is that the cantilever is doped on the tip side of the cantilever and that the tip itself is also doped. This is confirmed by the original publications[9,10] and by Marco Tortenase, who is now in charge of piezolever® manufacturing at Park Scientific.[11]

---

8. Park Scientific Instruments, 1171 Borregas Ave., Sunnyvale, CA 94089. (408)747-1600
9. M. Tortenase et al., *Appl. Phys. Lett.* **62**, 834 (1993).
10. Ph.D. Thesis, M. Tortenase, Stanford University (1993).
11. Personal communication.

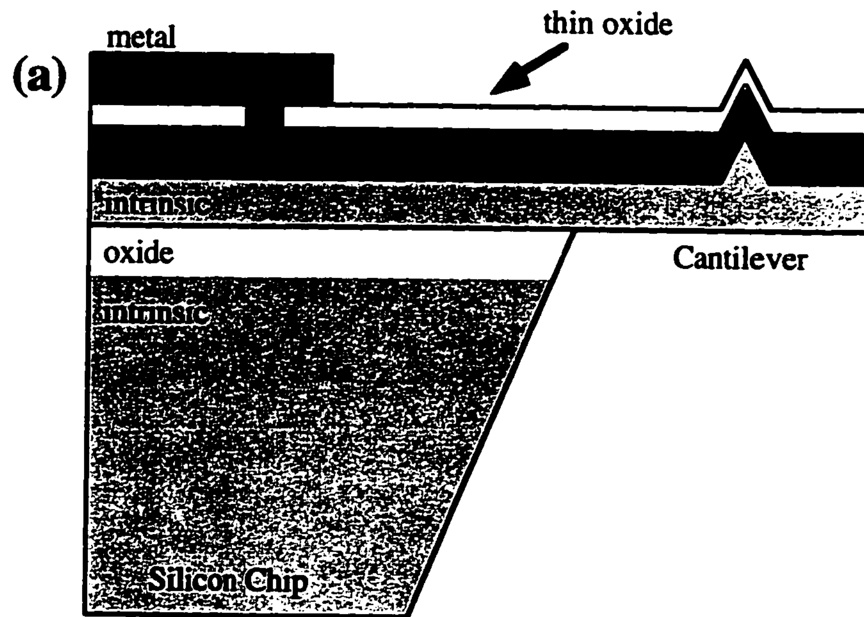

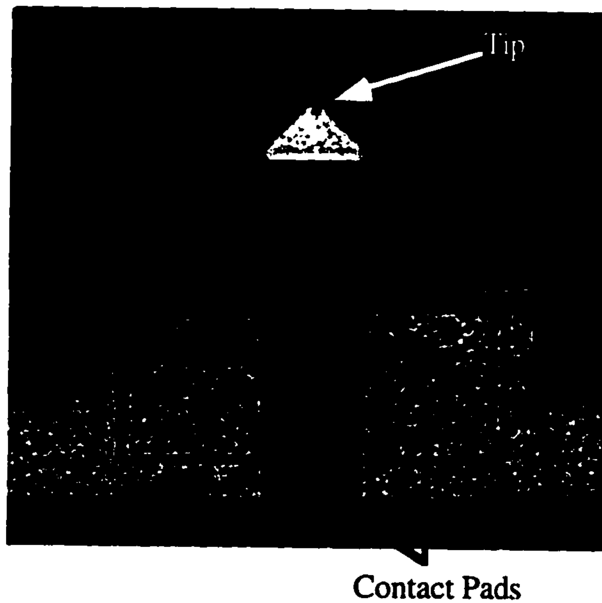

Figure 3-5 (a) Schematic cross–section of piezoresistive cantilever.
(b) Photograph of piezoresistive cantilever. The cantilever is 150 μm in length.

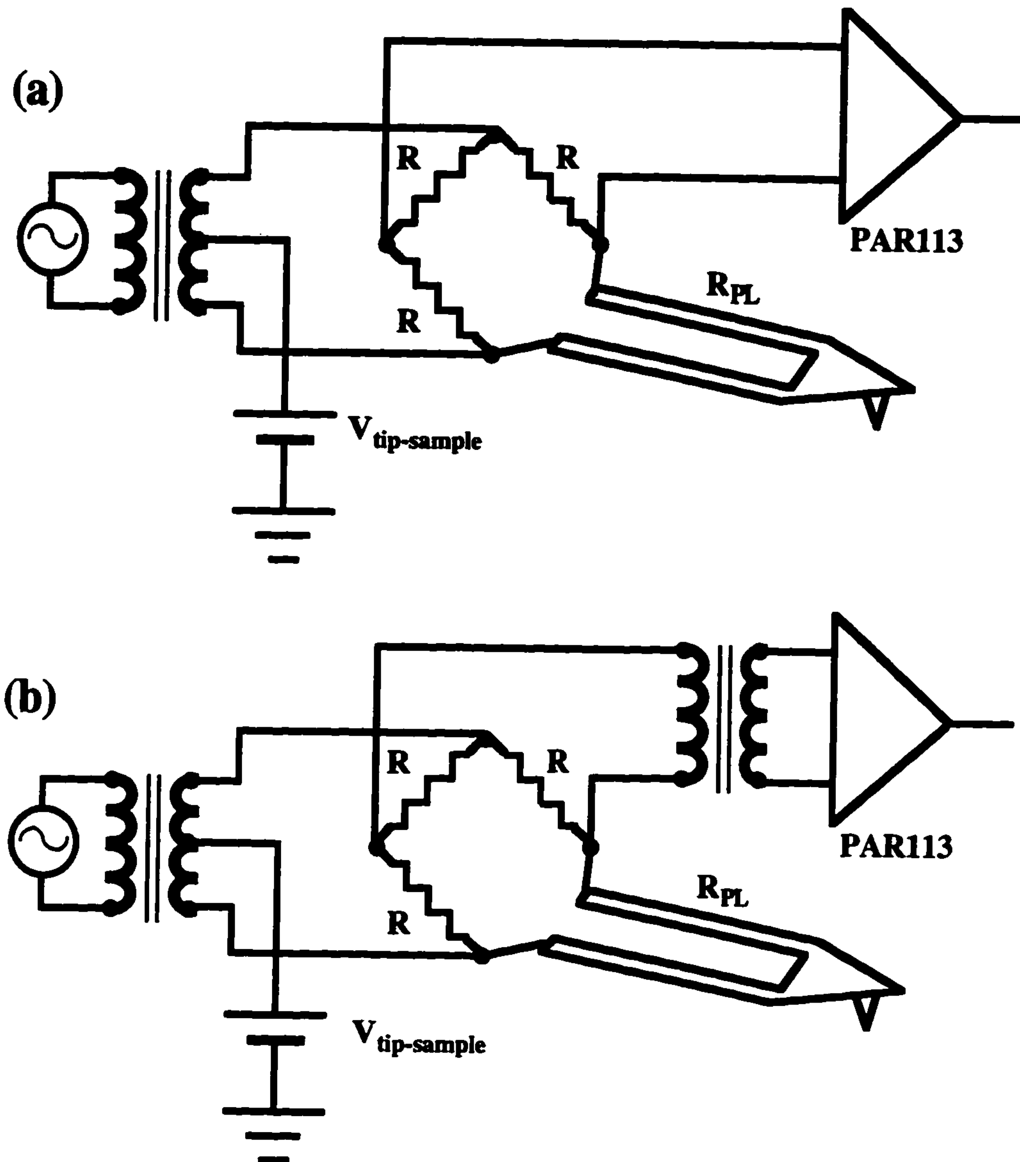

Figure 3-6 Cantilever measurement schematic.

In addition to the fact that these cantilevers remove the need for an optical readout, the main advantage offered by piezoresistive cantilevers is that the readout is fully integrated. For small deflections, the cantilever displacement is proportional to the

change in cantilever resistance. The sensitivity of the piezolevers® is approximately $\frac{\Delta R}{R} = 0.3\times10^{-6}/\text{Å}$. For typical deflections, the change in resistance is obviously a small fraction of the total resistance of the piezolever, and for this reason the cantilever is usually operated as one arm of a Wheatstone bridge.

Figure 3-5 (b) is a photograph of a piezoresistive cantilever. The contact pads to which wires can be bonded are clearly visible in the bottom part of the photograph. The current path extends from one of these pads, up one arm of the cantilever, across the cantilever's triangular-shaped top, and down the other arm to the remaining pad. The tip is barely visible as a dark dot near the top of the cantilever.

Figure 3-6 shows two Wheatstone bridge configurations which I use to measure the resistance changes in the cantilevers. In both cases the cantilever is one arm of the Wheatstone bridge. The cantilever in this case is of course in the helium Dewar, but the rest of the bridge was located outside the Dewar and at room temperature. A Krohn-Hite oscillator provided the drive voltage for the bridge, and the output was amplified first by a PAR113 preamplifier and then fed into a PAR124A lockin amplifier. Figure 3-6 (a) shows the case in which the PAR113 is ac–coupled, and Figure 3-6 (b) shows the case where we used a second transformer to isolate the PAR113 preamp. Transformer isolation was sometimes necessary because the maximum common mode voltage which the PAR113 will tolerate is only 1 V.

The advantage of the measurement circuit shown in figure 3-6 is that it allows the entire bridge to float with respect to the sample. The sample is held at ground, and a voltage box is used to supply a dc level to the center–tap of the transformer driving the bridge. This guarantees a known applied dc voltage at the cantilever tip. Another possible configuration is to apply an ac voltage to the center-tap, and thus oscillate the tip voltage relative to the 2DEG (see chapter 5).

The fundamental noise limit in cantilever deflection is sometimes the thermal-mechanical noise in the cantilever itself. The root mean square thermal noise for a cantilever of spring constant k is[9]

$$x_{rms} = \sqrt{\frac{k_B T}{k}}. \qquad \text{(EQ 5)}$$

For the Park Scientific piezoresistive cantilevers this limit is 0.6 Å at room temperature, and 8 pm at 4.2 K, assuming a typical spring constant for these cantilevers of 1 N/m. This is lower than the other noise levels in our instrument.

The noise limit of the piezoresistive cantilever technique is the Johnson noise in the cantilever itself.[9] In order to assess the noise in our system, and to test a new measurement scheme, we have recently installed a cooled Wheatstone bridge in the helium Dewar itself. For these measurements we have switched to a dc-biased Wheatstone bridge. The dc-bias allows us to record the noise in the measurement

circuit, and it also avoids cross-talk due to the large capacitance between some of the Dewar wires.

Figure 3-7 shows the new measurement circuit for use when the Wheatstone bridge is located entirely inside the Dewar. In this case the bridge is not accessible during the measurement, and therefore it cannot be zeroed to high precision. However, one of the advantages of placing the bridge inside the Dewar is that two of the bridge resistors can be cantilevers. The piezoresistive cantilevers from Park Scientific come with a second cantilever fabricated in the middle of the cantilever package. Using this cantilever as the arm which matches the primary cantilever helps to reduce problems with thermal drift, both during the cooldown from 300 K to 4 K and during normal operation. By using the Wheatstone bridge we obtain an order of magnitude increase in allowed gain before we compare this voltage with a reference setpoint. This is very useful in reducing the noise contributed by the comparison voltage source.

Figure 3-8 shows the measured noise spectrum taken at room temperature with the measurement circuit shown in figure 3-7. The gains of the two PAR113 amplifiers are removed from the measurement, so that the data shown in figure 3-8 is referenced to the voltage levels at the bridge. The drive voltage for this measurement was V_{bias} = 100 mV, and the bandwidth on both PAR113s was 300 kHz. The single peak at 180 Hz is due to magnetic pickup in the cables running from the Dewar to the PAR113, and is not a fundamental limit.

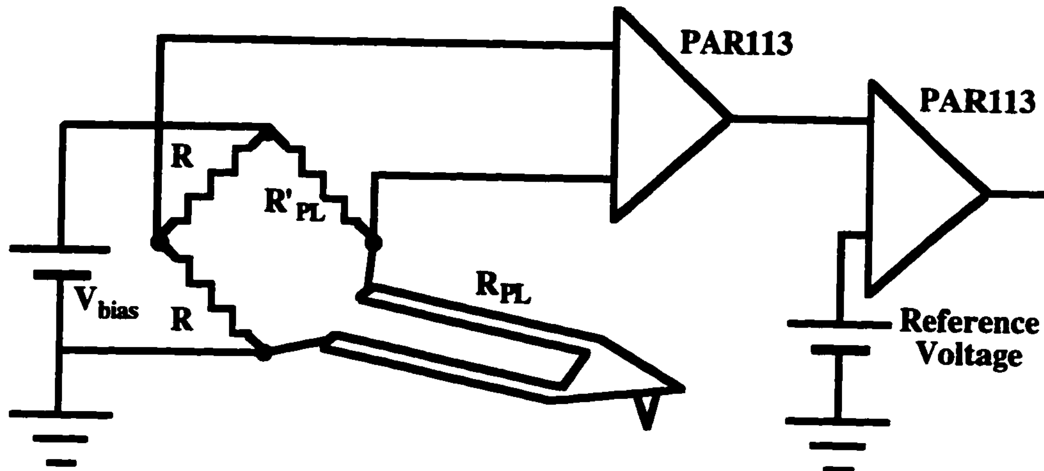

Figure 3-7 DC coupled bridge for use in Dewar.

As can be seen from the graph in figure 3-8, the white noise level at high frequencies is approximately $9\frac{nV}{\sqrt{Hz}}$. The source resistance of the bridge circuit is 2 kΩ (two sets of two parallel 2 kΩ resistors in series with one another is 2 kΩ). Therefore the Johnson noise limit at 300 K is equal to $V_{Th} = \frac{\sqrt{4kTR}}{\sqrt{Hz}} = 5.8\frac{nV}{\sqrt{Hz}}$. The white noise level of our piezolever measurement circuit is 1.6 times the thermal limit. This factor of 1.6 is completely due to the first PAR113 amplifier. The PAR113 is optimized for source resistances of 1 MΩ to 10 MΩ, and frequencies from 10 Hz to 1 kHz. Because our source resistance is 2 kΩ, the PAR113 contributes a multiplicative noise level given by the noise figure, which is approximately 6 dB in this range. A noise figure of 6 dB

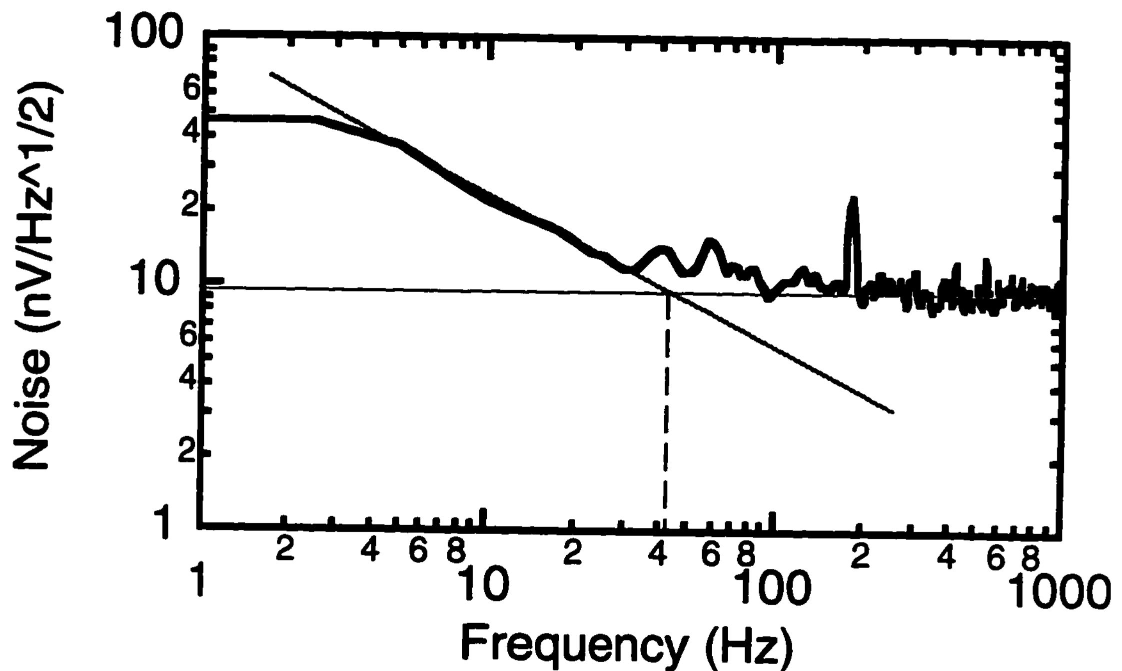

Figure 3-8 Noise power spectrum for circuit shown in figure 3-7.

means that the PAR113 should approximately double the thermal noise of the measurement circuit, which is close to what we observe.[12]

The electronic noise level in the cantilever deflection measurement can be converted to a displacement noise level. The response to a resistance unbalance at the Wheatstone bridge is

---

12. PAR113 users manual. See pg. III-1 for an explanation of the noise figure.

$$V_{signal} = \frac{\Delta R}{4R} \times V_{bias}. \quad \text{(EQ 6)}$$

The piezolever® response to a deflection is $\frac{\Delta R}{R} = \frac{0.3 \times 10^{-6}}{\text{Å}}$. Therefore the unbalance signal corresponding to a 1 Å deflection is $\frac{0.3 \times 10^{-6}}{4} \times V_{bias} = 7.5\ \text{nV}$. So a white noise level of $9 \frac{\text{nV}}{\sqrt{\text{Hz}}}$ corresponds to a white deflection noise level of $1.2 \frac{\text{Å}}{\sqrt{\text{Hz}}}$. If desired, the sensitivity of this circuit could be improved by 60% by the acquisition of a preamplifier designed for use with 2000 Ω source impedances.

The noise level of our measurement system is comparable to that achieved in the original work of Tortenase et al.,[9] which is not surprising since we are using the same cantilevers. Tortenase et al. found a better deflection noise level, because they were able to use a large bias voltage of 8 V across their Wheatstone bridge at room temperature. In our application we are limited to a 100 mV bias voltage, to avoid heating the cantilever at low temperature. The larger bias voltage of 8 V would supply more than 6,000 times as much power as we can tolerate in our low temperature application.

3.3 Microscope stage

The microscope stage is one of the most critical components of a scanning probe microscope. The purpose of the stage is to maintain a rigid mechanical loop between the tip and the sample.[13]

Figure 3-9 is a photograph of the SPM stage, which is the heart of the entire instrument. The stage has two main parts. First, the head of the SPM stage positions the cantilever over the top of the sample, and allows for a coarse approach. Second, the base of the SPM stage contains a scanning element for moving the sample in all three directions. The base also supports the SPM head in a rigid mechanical loop.

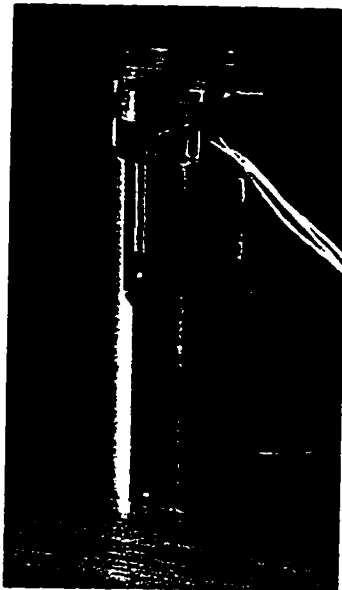

Figure 3-9 SPM stage. The entire unit is about 4.5 inches tall, and it is 1.25 inches in diameter.

3.3.1 SPM stage head

Figure 3-10 is a close up photograph of the head of the SPM stage. The main piece is made of brass, and it holds three 1/4 – 100 screws which allow for careful leveling and

[13] For a review of SPM instrumentation see Y. Kuk and P.J. Silverman, *Rev. Sci. Instr.* **60**, 165 (1989).

vertical positioning of the cantilever. One of the main purposes of the SPM head is to provide the coarse approach for the instrument. "Coarse approach" refers to the large scale positioning which is necessary to bring the cantilever within the restricted range of the fine scanning element (the piezoelectric tube scanner — see below), which is used to generate images. In our instrument the coarse approach is accomplished by turning one of the 1/4 – 100 screws to lower the entire SPM head towards the SPM base and the sample. The SPM head is made of brass instead of stainless steel because the screws, which are made of stainless steel, bind to stainless steel threads upon repeated thermal cycling between 4 K and 300 K. The three screws which support the head can be turned to keep the head level over the sample, but only one screw should be used for the final coarse approach. This helps maintain the SPM alignment.

Lateral positioning is very important for our application, because we are interested in studying fabricated nanostructures, not just random features. The SPM head is specially designed to allow easy lateral alignment. As shown in figure 3-10, the cantilever is hung from a small shuttle. This shuttle rests on three ruby balls which allow it to slide across the surface of the SPM head. The shuttle is held down by a spring clip. Its horizontal position is controlled by two screws and a spring. In this way the shuttle, and thus the cantilever and tip, can be positioned anywhere in a large area over the sample.

For simplicity, we currently mount the cantilever by epoxying it to a rod which extends through a hole in the sample head. This has the advantage that we do not need a

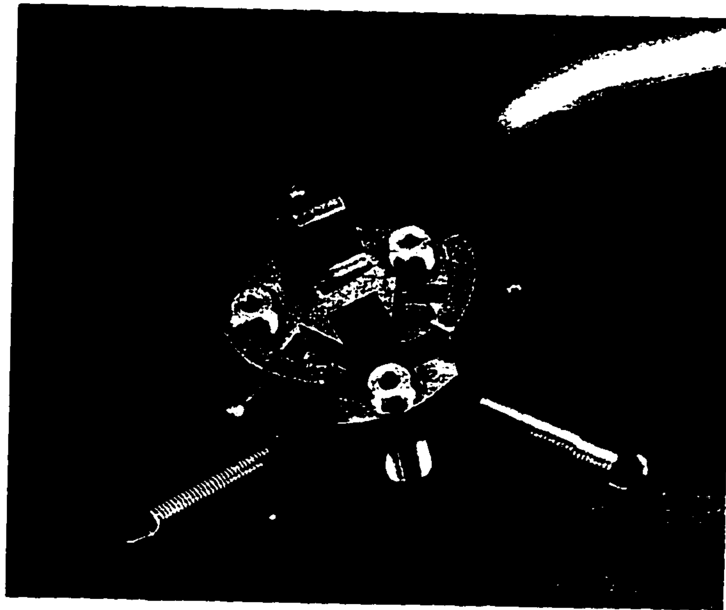

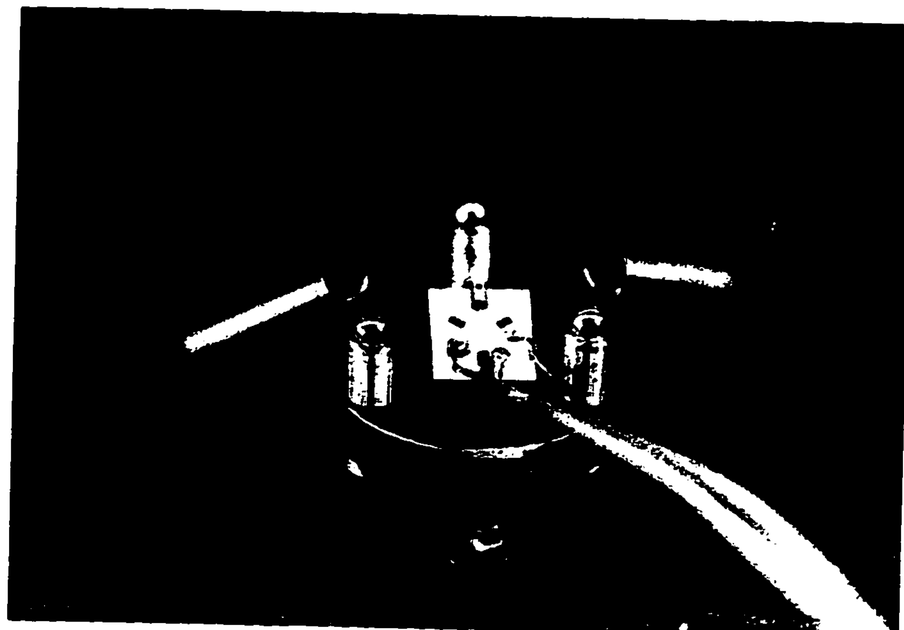

Figure 3-10 SPM stage head, top and bottom views. The stage head is 1.25 inches in diameter.

bulky mounting clip, but it also has the disadvantage that it takes a few hours to change tips. If it becomes necessary in the future to test multiple tips to obtain the very best resolution, then a clip system will be preferable.

3.3.2 SPM stage base

Figure 3-11 is a close up photograph of the SPM stage base. The base is designed to hold the SPM head over the sample in the most compact way possible. The entire SPM is small enough to fit inside the ^{3}He system in the Westervelt group lab, which has a high field superconducting magnet. We have not yet made use of this option.

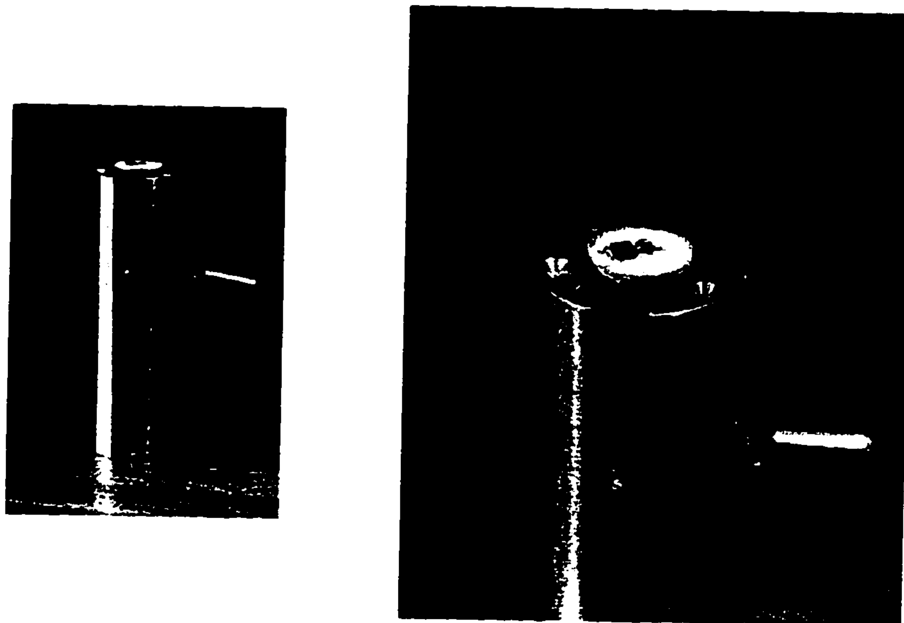

Figure 3-11 SPM base, full view and a closer view of the sample mount. The base is 1.25 inches in diameter, and 3.25 inches tall.

Figure 3-12 is a photograph of a piezoelectric tube scanner, which sits inside the base, as shown in figure 3-11. The primary purpose of the base is to support this scanner which holds the sample and provides the scanning capability for the SPM. The tube scanner was invented in 1986 by Binnig and Smith,[14] and its main advantages are its simplicity and its generally high resonant frequencies. We obtain all of our tube scanners from Stavely Sensors Inc.[15]

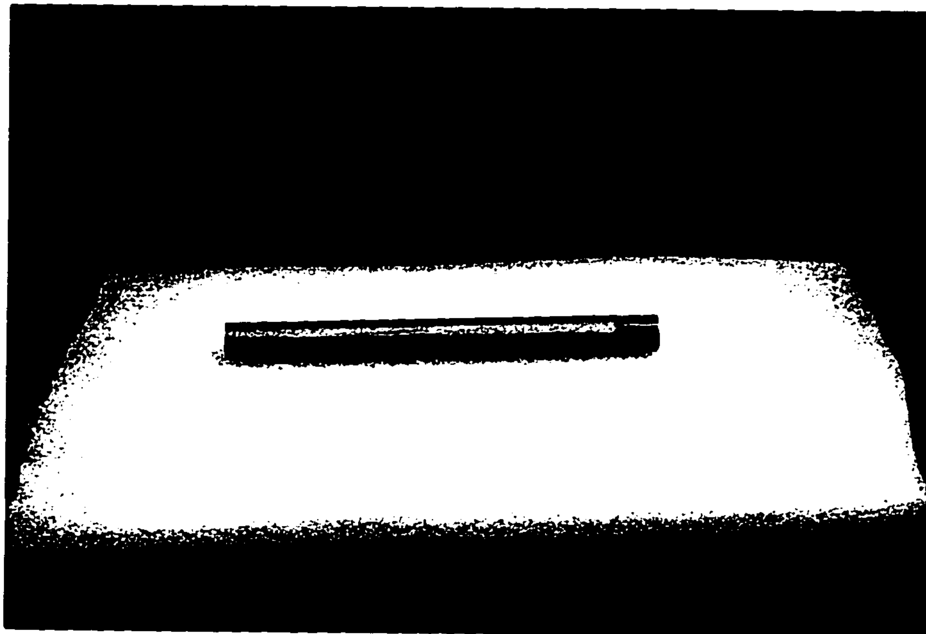

Figure 3-12 Piezoelectric tube scanner. Length = 3.0 inches. Width = 0.25 inches. Wall thickness = 0.020 inches. Note the electrode removal at the right end of the tube scanner. This greatly decreases the chances of developing a short between the electrodes when the scanner is mounted in a ceramic base.

14. G. Binning and D. P. E. Smith, *Rev. Sci. Instrum.* 57, 1688 (1986).

15. Stavely Sensors Inc., 91 Prestige Park Cir., East Hartford, CT 06108. (203)289-5428

The tube scanner is based on the piezoelectric effect. When voltages are applied between one of the outer four quadrants and the single inner quadrant, the piezoelectric material either expands or contracts. This expansion and contraction bends the tube in a circular arc, which to a first approximation scans the tip in a plane.[2,16] Motion in the z-direction is obtained by applying a common voltage to all of the outer electrodes with respect to the single inner electrode.

As will be seen in the following section, the resonant frequency of the stage plays an important role in determining the vibration induced noise level. The higher the resonant frequency of the system, the better the noise level will be. The limiting resonant frequency in our SPM is the piezoelectric tube scanner, and its lowest resonant frequency is in its bending mode. The bending mode resonant frequency is given by[2]

$$f_0 = \frac{0.56\kappa c}{L^2}, \qquad \text{(EQ 7)}$$

where c is the speed of sound, $c = \sqrt{\frac{Y}{\rho}}$, and κ is given by

$$\kappa = \sqrt{\frac{D^2 + d^2}{8}}. \qquad \text{(EQ 8)}$$

In Eq. (8) D and d are the outer and inner diameters of the tube, respectively. For EBL#4,[15] the piezoelectric material our scanners are made from, Young's Modulus

16. C. Julian Chen, *Appl. Phys. Lett.* **60**, 132 (1992).

$Y = 6.5\times10^{10}\frac{N}{m^2}$, and the density $\rho = 7.5\frac{g}{cm^3}$, which gives $c = 2900\frac{m}{s}$. The tube scanner is 3.0 inches long, 1/4 inch in diameter, and has a wall thickness of 0.020 inches, so $\kappa = 2.93\times10^{-3}\,m$. This gives a lowest resonant frequency of about 820 Hz for our bare tube scanner. In the actual instrument the tube scanner holds the sample, and this reduces the resonant frequency to around 450 Hz.

For comparison, the lowest resonant frequency of the stainless steel base itself is around 5 kHz. The performance of our SPM is thus ultimately limited by the low resonant frequency of the long tube scanner. Fortunately, as we will see in the final section of this chapter, the resolution of our SPM is more than good enough for our current applications. As will be discussed in section 3.4, the resolution of our SPM could be increased by using a higher resonant frequency scanning element.

As mentioned above, the reason that we use such a long and narrow tube scanner is to obtain sufficient range at low temperatures. The response of piezoelectric materials drops rapidly with temperature, typically falling by a factor of 3 to 5 between room temperature and very low temperatures. It turns out that the materials with a larger response at room temperature, the "soft" piezoceramics, lose more of their response at low temperatures than the hard piezoceramic materials.[17] As a result, most piezoceramics have similar piezoelectric responses at low temperature. For this reason

17. R.N. Kleiman. *Mat. Res. Soc. Symp. Proc.* **406**, 221 (1996).

we use a hard piezoceramic, EBL#4, in our scanners, because the hard piezoceramics have fewer problems with hysteresis and drift than the soft materials. The range of our instrument at low temperatures is 30 μm, using drive voltages of ± 200 V.

3.4 Reduction of vibration induced noise

One of the primary noise sources in scanning probe microscopes is external vibrations which induce motion between the tip and the sample. This motion is read as a signal by the feedback system, and appears as noise in topographic images. There are two methods of reducing vibration noise which will be considered in this section: vibration rejection and vibration isolation.

3.4.1 Vibration rejection

Vibration rejection refers to the ability of an SPM to operate in a vibrationally noisy environment without degrading the image quality. Atomic force microscopes work by measuring the deflection of a tip as it is scanned over the sample surface, as described in section 3.1. If the mechanical loop shown in figure 3-1 is rigid, then the deflection will accurately reproduce the surface topography. Vibrations which cause the mechanical loop to bend, however, will induce noise in the measured topography.

Figure 3-13 illustrates how external vibrations can couple into a scanning probe microscope. The mechanical loop which sets the reference for the cantilever displacement measurement is flexible and can be modeled as a spring with resonant

frequency f_0. External vibrations will cause the base to oscillate, and these vibrations will be coupled into the tip–sample gap.

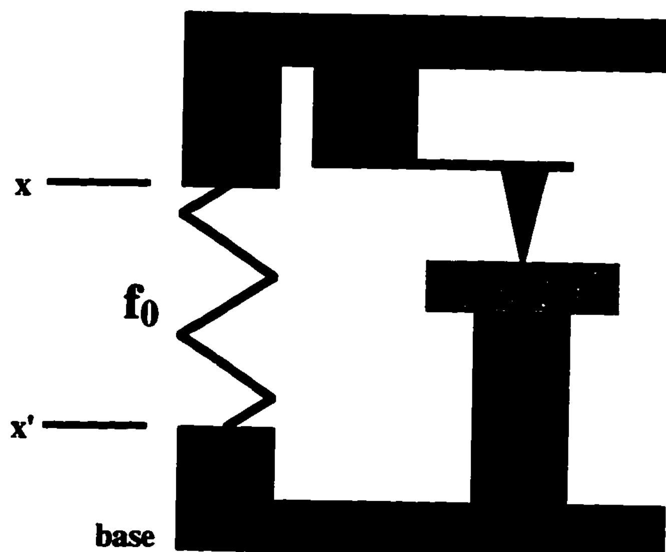

Figure 3-13 Mechanical instabilities in SPMs.

Following Park and Quate[18], we can write the equation of motion for this system as

$$m\ddot{x} + b(\dot{x} - \dot{x}') + k(x - x') = 0, \quad \text{(EQ 9)}$$

where x and x' are defined in figure 3-13. If x' is driven sinusoidally as $x' = x'_0 e^{i\omega t}$, then x will have a sinusoidal response given by $x = x_0 e^{i\omega t}$, where

$$\frac{x_0}{x'_0} = \frac{\omega_0^2 + 2i\gamma\omega}{\omega_0^2 - \omega^2 + 2i\gamma\omega}, \quad \text{(EQ 10)}$$

18. S. Park and C. F. Quate, *Rev. Sci. Instrum.* 58, 2004 (1987).

$\omega_0 = \sqrt{k/m}$, and $\gamma = \frac{b}{2m}$.[18]

Vibration rejection means that if the sample and tip move together as a rigid-body, that motion introduces no noise to the measurement. In the limit that ω is much smaller than the stage resonant frequency ω_0, the mechanical loop is effectively very rigid. The bandwidth of AFMs are typically only a few hundred Hz, and the resonant frequency of the AFM itself, f_0, is usually several kHz. The low frequency limit of Eq. (10) is simply[18]

$$\left|\frac{x_0}{x'_0}\right| \rightarrow 1 + \frac{\omega^2}{\omega_0^2}. \qquad \text{(EQ 11)}$$

The leading "1" in this equation means that in the low frequency limit the tip will move with the sample (i.e. there will be no noise transmitted). There will be corrections of order $\frac{\omega^2}{\omega_0^2}$, and these corrections will induce noise in the images. Increasing the resonant frequency of the AFM stage is thus highly desirable, because it will reduce the amplitude of the vibration induced noise. As described previously, the resonant frequency of our system is approximately 450 Hz. We typically operate in a bandwidth less than 100 Hz, so we achieve a modest level of vibration rejection.

3.4.2 Vibration isolation

Vibration isolation is a technique which keeps the scanning probe microscope stationary, even though the room in which it is sitting may be vibrationally noisy.

Figure 3-14 is a schematic diagram of the vibration isolation box I built for our scanning probe microscope. Many SPMs do not need vibration isolation to work well, and in fact we routinely use the SPM with the Dewar sitting directly on the tabletop. However, best resolution is achieved with the SPM inside the vibration isolation box.

In order to analyze the effectiveness of vibration isolation, we can use the same model as presented in the previous section. In Eq. (9) variable x now refers to the motion of the isolation box, and variable x' refers to the motion of the ceiling. Eq. (10) is again the solution, but we are now interested in the high frequency limit. The resonant frequency of the isolation box when it is hung from the ceiling is approximately 1–2 Hz. Most building vibrations are larger than this range. The large ω limit of Eq. (10) is given by[18]

$$\frac{x_0}{x'_0} \rightarrow \frac{2\gamma}{\omega}. \qquad \text{(EQ 12)}$$

Eq. (12) implies that "high" frequency building vibrations will be attenuated as the inverse of the frequency, for frequencies larger than a few Hz.

We are now in a position to understand the vibration limit imposed on our SPM. When the vibration isolation is used, only building vibrations near a few Hz will be

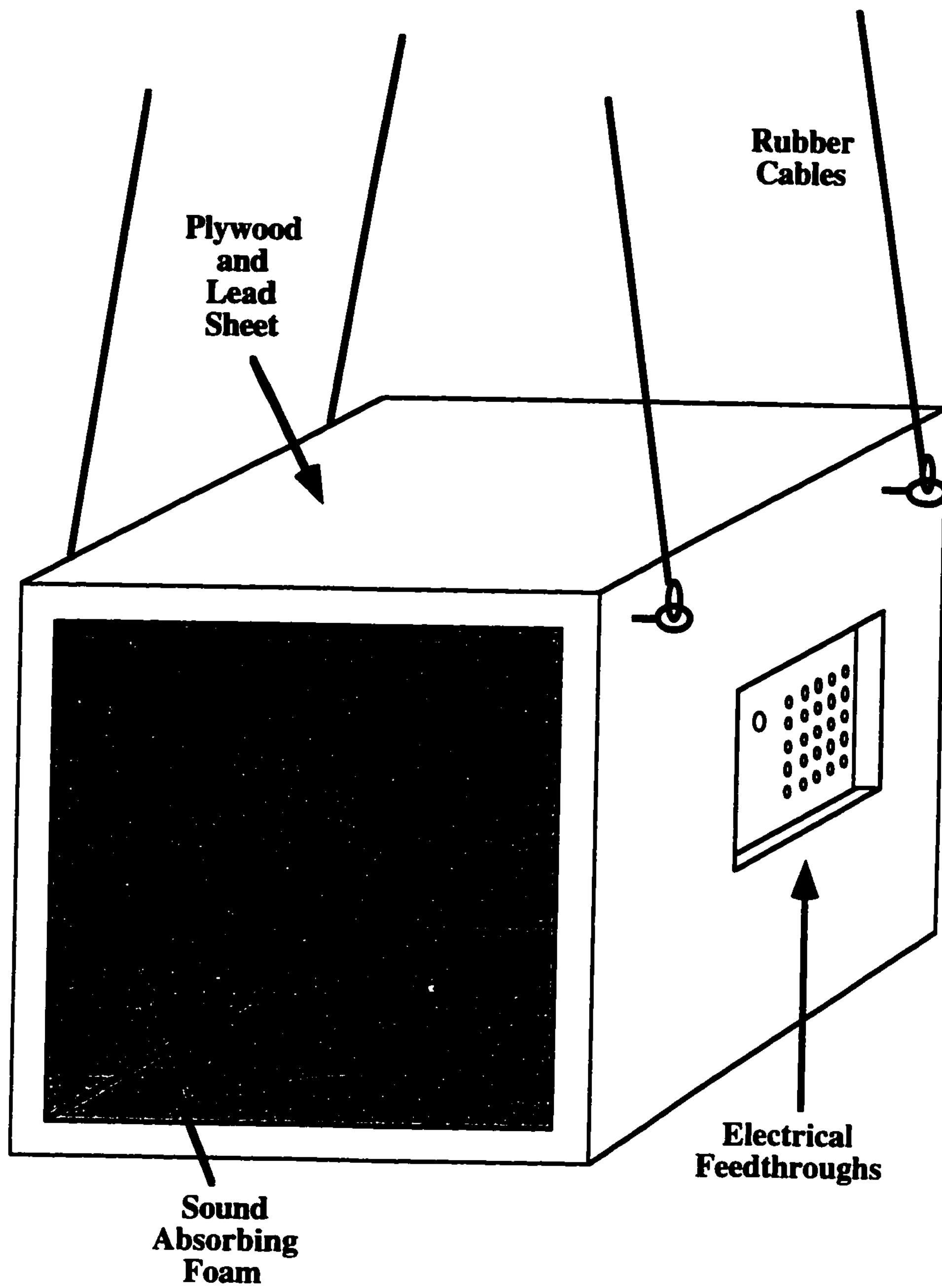

Figure 3-14 Vibration isolation box. The box is 32.5 inches square in cross section and 31.5 inches deep. The plywood is 3/4 inch thick, and the lead sheet is 1/64 inch thick.

passed to the instrument. These vibrations will then be rejected according to Eq. (11) as $\frac{\omega^2}{\omega_0^2}$. Our system has an acceptable noise level for current applications, without using the vibration isolation. If lower noise levels are required in the future, the vibration isolation box can be used, or higher resonant frequency scanning elements may be needed to replace the current tube scanner.

3.5 Dewar

Experiments on semiconductor microstructures need to be carried out at low temperatures, so our SPM was designed to work at 4.2 K inside a liquid helium Dewar.

3.5.1 Dewar basics and operation

Figure 3-15 is a schematic diagram of the Infra-Red Labs[19] Dewar in which we carried out our experiments. The Dewar is approximately 16 inches tall and 10 inches in diameter. We chose to use the IR Labs Dewar for two reasons. First, it has a large evacuated cold space in which we could mount the SPM and into which we had a good mechanical feedthrough. Second, it was available for a good price — free.

The hold time for this Dewar is approximately 15 hours, which is very nice because it means helium transfers need only be done twice a day. The Dewar is designed with both a helium and a nitrogen can. The nitrogen can is attached to a radiation shield which completely encloses the helium can and the cold space. The helium can also has a

19. Infrared Laboratories, Inc., 1808 East 17th St., Tucson, AZ 85719. (602)622-7074

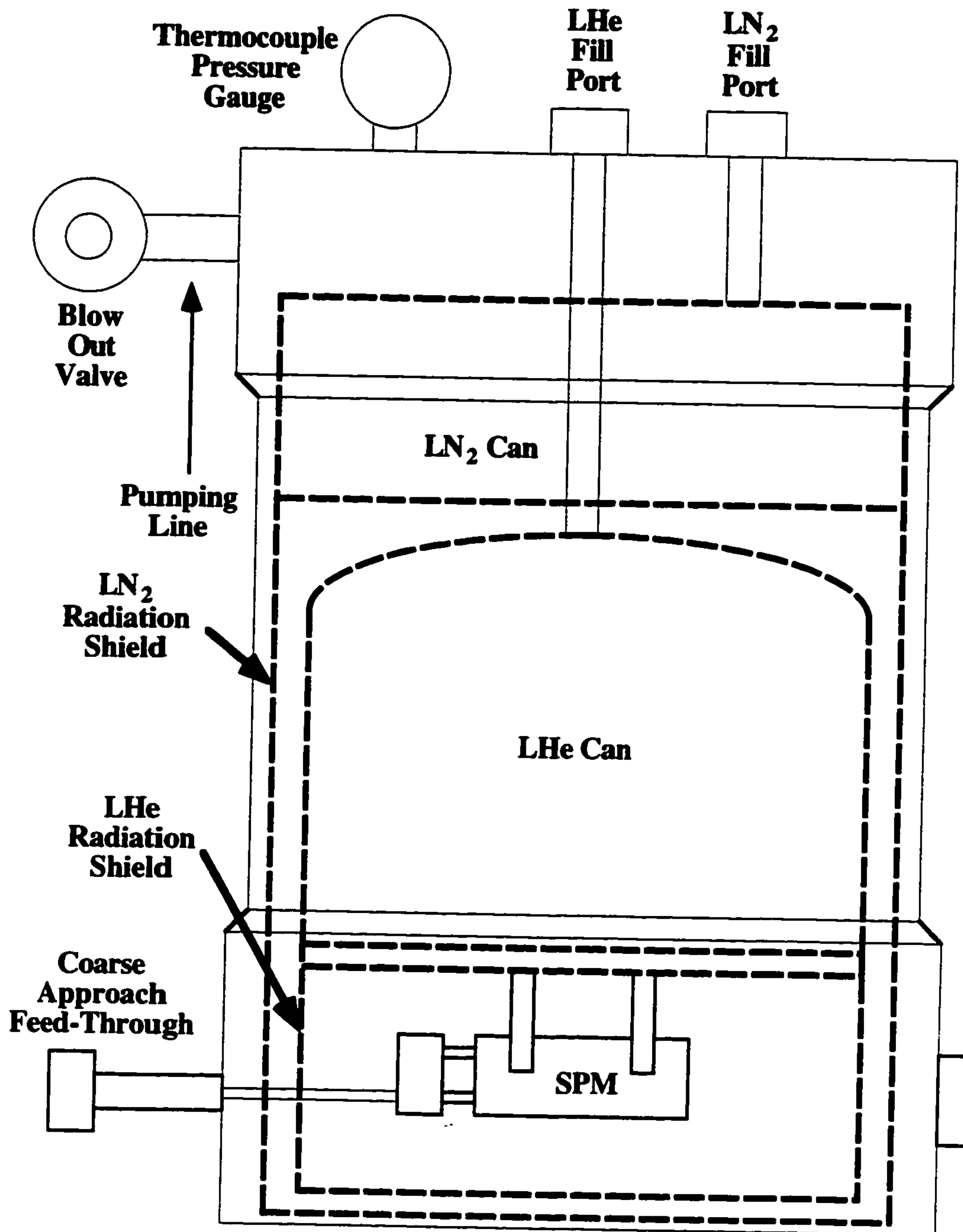

Figure 3-15 Liquid helium Dewar with cold space. The SPM is attached to the cold plate, and a mechanical feedthrough on the left is used to turn the coarse approach screw. The Dewar is 16 inches tall, and 10 inches in diameter.

radiation shield which encloses the cold space. The base of the cold space is a solid copper plate which also forms the bottom of the helium can. Our SPM is cooled by conduction through its metal body and this cold plate.

The Dewar is insulated by the vacuum space between the cans and the outside wall. This space is open to the atmosphere when the working space is open. The vacuum must be ≤ 1 mtorr when liquid helium is in the Dewar, or the boil off rate will be unacceptable. When the Dewar holds helium it will cryopump most gases, so the Dewar will only be soft when it is cold if there is helium in the vacuum space. The procedure for cooling the Dewar is as follows:

- Close all radiation shields and seal the Dewar.
- Invert the Dewar — get help, it is heavy.
- Pump out the Dewar to about 30 mtorr with the Edwards model 18 mechanical pump. This takes about 15 min.
- Add liquid Nitrogen to both the LN_2 *and* the LHe cans. Let sit for about 3 hours while still pumping on the Dewar.
- Blow the LN2 out of the He can using the blow-out tube found in room 203.
- Make sure the LN2 is all out of the can by checking the can with a thin rod — the LN2 transfer tube will do fine. This step is *crucial* or the LHe transfer tube will freeze in the He can.

- Transfer LHe using the large transfer line. The boil off will begin pulsing when the can is full. A full can should thump out to 4.5 inches.
- It is important to attach hoses which run from the cryogen can to the floor whenever cryogens are in the Dewar. If the cans are left open without long hoses attached, ice blocks can develop in the tube leading to the cans.

Compromising the integrity of the vacuum when there is liquid helium in the Dewar is an extremely bad idea. The heat of fusion of helium is small, so the helium in the Dewar will vaporize essentially instantaneously when the Dewar softens. This can result in dangerous pressure building up in the Dewar if the fill tube is not wide open.

3.5.2 SPM mounting and feedthroughs.

Figure 3-15 shows the SPM mounted on the cold plate of the helium Dewar. When the Dewar is warm, it is upside down so that the working space and the SPM can be easily accessed. When everything is closed and ready to be cooled to 4 K, the Dewar is inverted and pumped out.

Figure 3-16 shows the coupling which forms an important part of the coarse approach feedthrough. As described in section 3.3, the coarse approach in our SPM is accomplished by turning a 1/4 – 100 screw, which lowers the cantilever towards the sample. It is important that the SPM head not be rigidly attached to the feedthrough, or else the head will be twisted by the torque applied to turn the approach screw. This has a disastrous effect on the SPM resolution.

To avoid twisting the head we introduced a simple universal joint into the feedthrough bar. The feedthrough shown in black is held rigidly by the joint at the Dewar wall. The coupling shown in gray is held in place by a “swivel joint” between itself and the first piece, and by a second swivel joint between itself and the coarse approach screw. The “swivel joint” simply consists of a ball sitting in a depression in the opposite piece. This allows the coarse approach screw and the feedthrough to be completely misaligned without applying any torque to the SPM head. Torque is applied to the screw when the arms of the primary feedthrough (in black) twist into the arms of the coupling (in gray). This simple system has worked very well.

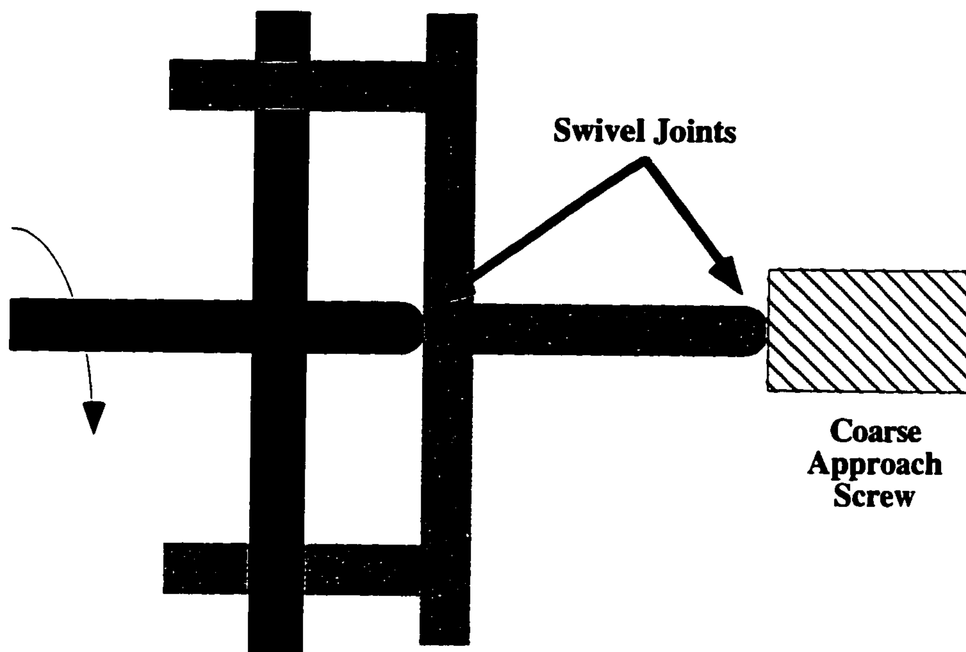

Figure 3-16 Coarse approach coupling.

The other feedthroughs needed to run the SPM and measure nanostructure electronic properties are electrical feedthroughs. There are three sets of electrical feedthroughs on the Dewar. The high voltage feedthrough is a "military" connector.[20] Its only purpose is to carry the 5 high voltage lines which run the piezoelectric tube scanner. The two other feedthroughs are a 24-pin and a 14-pin Fisher connector. One handles the wires which measure the deflection of the cantilever. The other carries the wires which are needed for making electrical measurements on the nanostructures. By separating the connectors in this way we reduce the capacitive coupling between these leads, which reduces the pickup between the lines.[21]

3.6 SPM electronics

As with many modern instruments, scanning probe microscopes are controlled almost entirely with electronics. Our SPM has a series of circuits which work in combination with a Power Macintosh 7100 personal computer. The computer communicates with the electronics through a standard analog/digital (A/D) and digital/analog (D/A) card. This section describes the home-built electronics, and how they are used.

3.6.1 Overview of the SPM electronics

Figure 3-17 is a schematic diagram illustrating the control electronics for our scanning probe microscope. As described previously, the goal in operating an SPM is to

---

20. Type MIL-C-XXX connector, available from Amphenol through Gerber. (617)769-4852

21. Only one connector was in use for the first experiments reported in chapter 5. After doing those experiments we thought it would be easier to do future experiments with less capacitance between the lines, so the additional feedthrough was added.

scan a sample beneath the cantilever and tip, while maintaining a constant deflection of the cantilever. The computer outputs a waveform, $V_x(t)$ and $V_y(t)$, which will drive the piezoelectric tube scanner in a raster scan. This output enters a box which adds a constant offset, VO_x and VO_y, to that signal, if desired. This "split and offset" box then outputs those voltages and their negatives, $V_x(t) + VO_x$ and $-V_x(t) - VO_x$. Two polarities are required because the tube scanner works best when opposing sides are driven with opposite voltages. It is more convenient to invert the voltages before the high voltage amplifiers rather than to work with both high voltage inverting and high voltage non-inverting amplifiers. The raster scan waveform is amplified 20 times by the high voltage amplifiers shown in figure 3-17 to a maximum value of ± 200 V. This high voltage waveform drives the piezotube in a raster scan, which can cover a square 30 μm on a side at liquid helium temperatures.

As shown in figure 3-17, the z–position is controlled by a fifth high voltage amplifier, which is driven by the feedback loop. The cantilever measurement circuit, which was discussed in section 3.2, sends a voltage which is proportional to the cantilever deflection to the feedback circuit. The feedback circuit then sends the appropriate signal to the z high voltage amplifier to maintain a constant tip deflection. The feedback signal is also recorded by the Power Macintosh, and it is this signal which generates the topographic image.

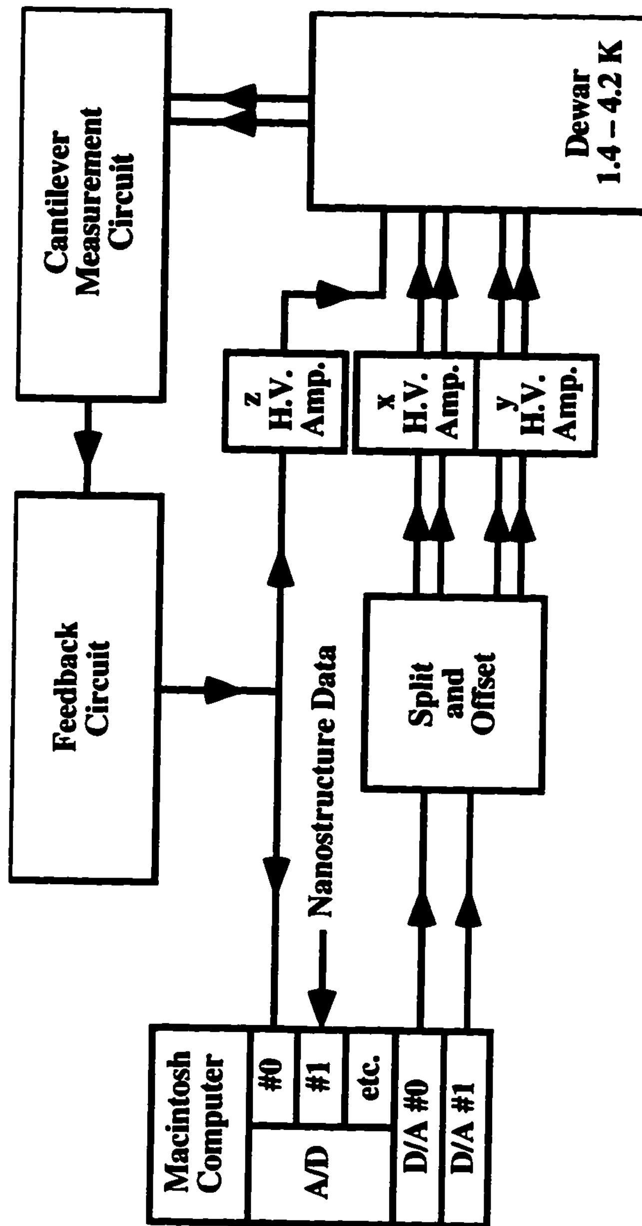

Figure 3-17 Electronics overview.

3.6.2 Control electronics

Figure 3-18 is a schematic diagram of the circuit used to split and offset the voltages which control the raster scan. The actual circuit, as with all the circuits shown in this chapter, is etched into a printed circuit board. The fabrication procedure for making printed circuit boards is very straightforward, and a recipe is given in appendix A. The x and y channel circuits of figure 3-18 are straightforward: the row of three op-amps at the top of the diagram are simply a differential amplifier to receive the signal from the computer, a summing amplifier to allow the addition of an offset voltage if desired, and an inverting amplifier to generate the inverted signal for the piezotube.

The lower half of the circuit shown figure 3-18 allows a voltage to be sent to the z amplifier which is proportional to the raster scan position. This type of offset can be used to anticipate the slope of a sample. By feeding the correct average slope to the z amplifier, the system makes fewer demands on the feedback circuit, which can improve overall performance.[2]

Figure 3-19 is a schematic diagram of the high voltage amplifiers. The amplifiers are simply inverting amplifiers made from PA85A high voltage op amps, which are available from APEX Microtechnology Corporation.[22] There are several important differences between high voltage op amps and the more common ± 12–15 V op amps which are usually used in the laboratory. First, and most importantly, these op–amps are

22. APEX Microtechnology Corporation, 5980 Shannon Rd., Tucson, AZ 85741-5230. (602)690-8600

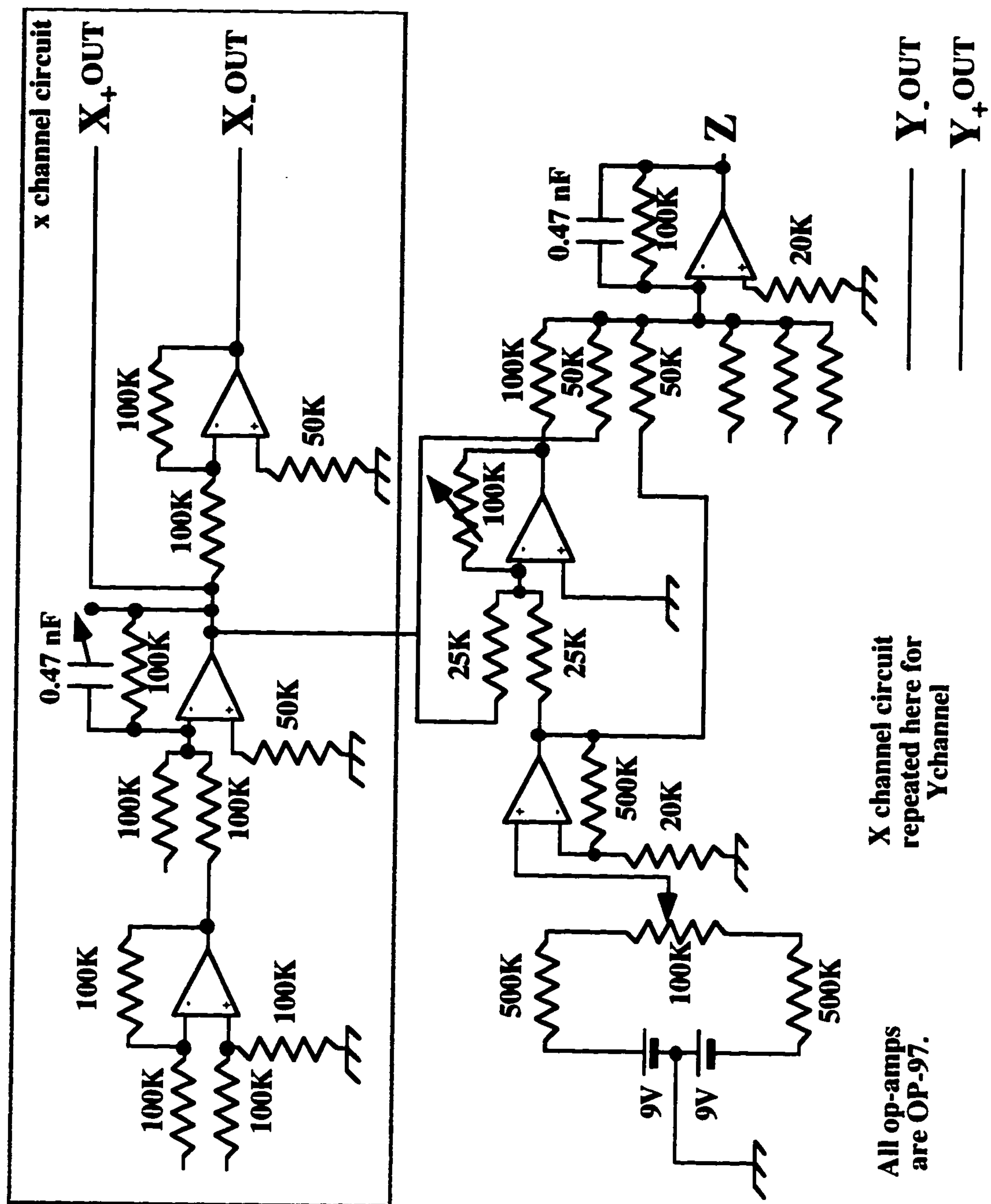

Figure 3-18 Split and offset circuit diagram. All op amps are OP-97 from Analog Devices unless otherwise stated. All resistors are metal film resistors.

capable of supplying large currents (200 mA) at very high voltages (± 225 V). They are therefore inherently dangerous unless proper care is taken in their use. It is very important to check the experiment carefully to ensure that everything is hooked up in a safe configuration, and in particular to ensure that the instrument cases and the Dewar are all well grounded. Second, of course, high voltage power rails must be supplied for the high voltage op amps to function properly. We use regulated supplies from KEPCO[23] for this purpose. Third, these op amps require external compensation and special overvoltage protection elements.

The external compensation and overvoltage protection elements are shown in figure 3-19. There are four main elements. First, a current limit is imposed by a single 30 Ω resistor, which gives a maximum current of 40 mA. Second, a double set of crossed diodes protect the PA85A input circuits from excessive overvoltage. Two diodes in series are used to achieve the necessary voltages to drive the maximum power bandwidth.22 Third, a compensation network of a resistor and capacitor in series (R_c and C_c) are required. This network determines the corner in the roll–off of the op amp open loop gain. Fourth, a resistor and capacitor in series across the inputs (R_n and C_n) are required to avoid oscillations. See APEX Application Note 19.22 A detailed description of these techniques is beyond the scope of this thesis, but all the procedures are well documented in the APEX Data Book.22

---

23. Product number ATE 325–0.8M. KEPCO, INC., 131-38 Sanford Ave., Flushing, NY 11352. (718)461-7000.

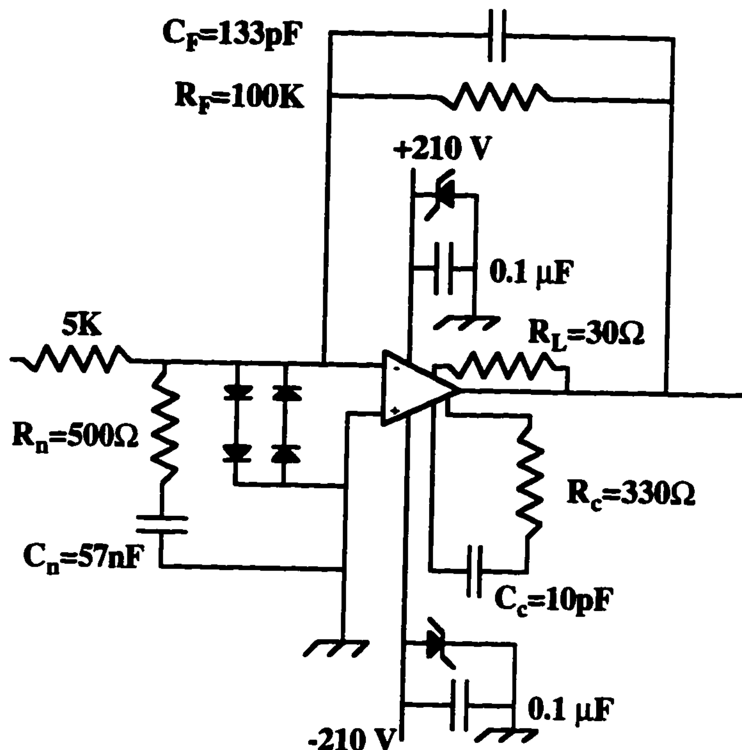

Figure 3-19 PA85A compensation and overvoltage protection schematic. The capacitors are 500 V ceramic, the resistors are 1/8 watt metal film (several in series in the feedback loop to handle the power dissipation), and the diodes are high voltage models available from Newark.

The final consideration is that high voltage op amps will oscillate if the elements listed above are soldered to a circuit board and wires are run to the pins on the op amp. Instead, a special socket must be used to hold the op amp, and all of the components must be wired directly to the socket itself. This process forms a little "birds nest" of circuit elements, but it is the only way to avoid oscillation due to stray capacitance between the wires.

Four of the high voltage amplifiers in figure 3-17 are simply boxes with the high voltage op amps and no other circuitry. These amplifiers have a gain of 20, and they drive the raster scan in X and Y. The fifth amplifier is the z amplifier, also with a gain of 20, but its box does contain an additional circuit.

3.6.3 Feedback and Z electrode electronics

Figure 3-20 is a schematic diagram of the circuit used to amplify the feedback signal to drive the Z electrode of the piezotube. The circuit consists of three differential inputs, plus an internal voltage source. The signal from the feedback board enters via one of the differential inputs, and the other two are available for test purposes. The low voltage circuit just adds the three external plus the internal voltages. The summed voltages are then amplified by a factor of 20 at the high voltage op amp. The internal voltage reference, shown at the top of figure 3-20, is useful for pulling the sample away from the cantilever. This is necessary, for example, during coarse approach.

Figure 3-21 shows the final circuit needed to run the SPM: the feedback circuit. Our feedback circuit is just integral feedback — this simple feedback system is found to be effective in scanning probe microscopes with piezoelectric scanning elements.[24] An internal reference voltage (the inverse of the setpoint) is added to the signal from the cantilever measurement circuit. The difference is then amplified by a gain of between 0.01 and 100, and then it is integrated with a time constant between 0.01 and 1 seconds.

---

24. D. Jeon and R.F. Willis, *Rev. Sci. Instrum.* **62**, 1650 (1991).

Figure 3-20 Z high voltage amplifier box. All op amps are OP-97 from Analog Devices, except the high voltage PA85A from APEX Microtechnology.

The final op amp element in the circuit simply passes the voltage, inverts the voltage, or grounds the output. The optimal feedback setting is determined dynamically by the user, and it depends critically on the settings in the cantilever measurement circuit.

3.7 Computer control system

The electronics which run the SPM are controlled by the Power Macintosh 7100. There are two parts to the control system: the plug-in board which allows the computer to communicate with the rest of the SPM, and the computer program which controls the instrument.

3.7.1 NB-MIO16X Board

The board which we use to interface with the SPM electronics is the NB-MIO16X, produced by National Instruments Corporation.[25] The NB-MIO16 is a multipurpose board with D/A, A/D, and digital input and output capabilities. The D/A output is used to generate the raster scan for the SPM. The control program described below can also use this D/A capability to move the tip so that it follows the motion of the computer mouse. Feedback is maintained throughout this motion. The NB-MIO16 has two 12-bit D/A channels. The output resolution of the raster scan is thus accurate to roughly one part in $2^{12} = 4096$. A typical scan will consist of 256 x 256 points, so even though the full 12-bit resolution is not always easily accessible (for example, over small scan ranges), the NB-MIO16 has plenty of resolution for most scans of interest.

---

25. National Instruments Corporation, 6504 Bridge Point Parkway, Austin, TX 78730. (512)794-0100

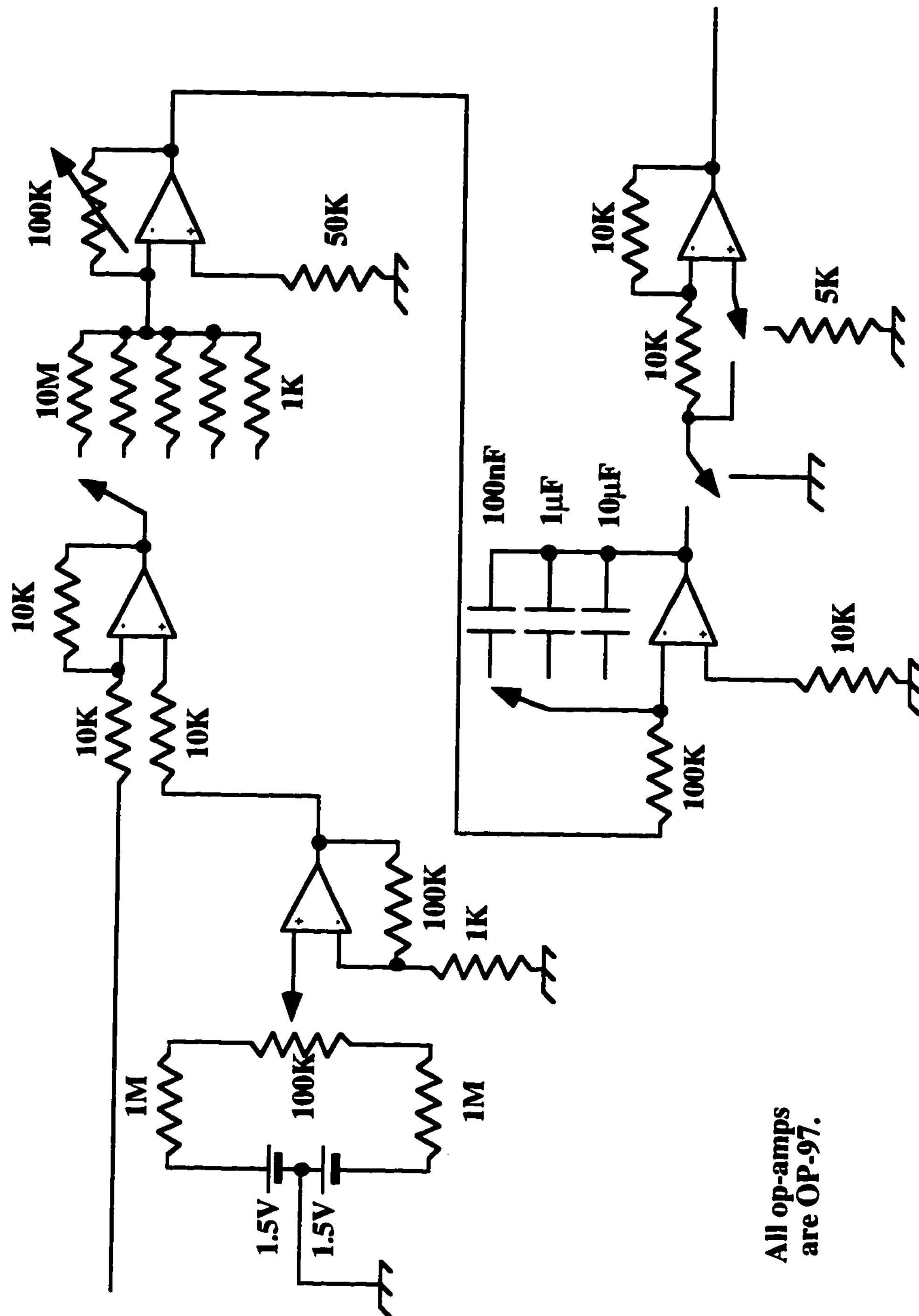

Figure 3-21 **Feedback circuit. All op amps are OP-97 from Analog Devices.**

The NB-MIO16 has one 16-bit A/D converter which is multiplexed on the board to 16 single ended or 8 differential inputs. In our usual configuration, one differential input reads the feedback voltage which generates the topographic image. We use a second differential input to measure an electronic property of the nanostructure under study — often we measure its resistance or a modulation of its resistance as a function of the tip position.

The digital inputs and outputs are used to control the timing of the various inputs and outputs from the board, so that the acquisition of data and the control of the SPM will be well synchronized. In this way data on nanostructure electronic properties is easily correlated with the surface topography.

3.7.2 Control program

The computer control program is written in Labview®, which is a graphical programming language developed by National Instruments Corporation.25 Because Labview interfaces easily with National Instruments plug-in cards, and because many of our other data acquisition programs are written in Labview, it was a natural choice for our control program. Labview has many advantages: for example, it is easy to learn its basic capabilities, create working programs quickly, and make convenient user interfaces. Its main disadvantage is that Labview limits the programmer's control of the plug-in boards to those applications which National Instruments has foreseen. This results in some interesting programming challenges, but on the whole Labview has worked well for this application.

There were two main requirements the control program had to meet. First, it had to be flexible and easy to use. Second, it needed to acquire the data in a carefully timed pattern, so that the data interpretation would be clear. Achieving careful timing of the data acquisition was the main hurdle to be overcome in the programming.[26]

The SPM control program, the current version of which is called AFM 6.3.1, has two main control capabilities. First, the program will output the x and y raster scan waveforms. Second, it will simultaneously acquire data on one or two channels. All of the data input and output is done through synchronous DMA transfers. The output waveform in x consists of a ramp, with a user controlled number of points. The output waveform in y steps the voltage at the end of each line; we pass this output through an RC filter with a time constant of 100 ms to avoid setting up ringing in the piezotube. The input data is acquired at a dynamically determined maximum rate, up to 20 kHz, and then binned to the user controlled number of points. The second control capability of the program is that it will move the SPM tip to follow the location of a cursor on the computer screen. In this way the tip can be moved across an image which was just acquired. The two data channels are continuously updated on the screen as this occurs, so that the topography and the nanostructure properties can be continuously monitored.

The control program is user friendly and flexible. The number of data channels, the speed of the tip during a scan, the resolution of a scan, whether the data is acquired right

26. Many thanks are due to Mark Topinka on this point. He carefully programmed a clever scheme to coordinate the data acquisition with the control waveforms which has worked very well.

to left or left to right, and the number of points in the output ramp are all controlled from the front panel. The user can have the program scan an extra range in x before acquiring data on each line, which helps to reduce the effects of hysteresis at the edge of an image. The program will also subtract a plane from the data as it is acquired, and will determine which plane will produce an image with no average slope (that is, an image whose best fit plane has a vertical normal). By turning off the screen update feature, data can be acquired at a known and constant rate. Previous images can also be easily loaded for comparison. Finally, the user can zoom in or out by moving cursors over the acquired image, making it easy to select an interesting part of the sample. All of these features make it easy to concentrate on the data, without worrying about the details of the data acquisition.

3.8 SPM performance

The true test of an SPM, of course, is whether or not it takes good images. I reproduce two images in this section as examples of the images we have taken with this SPM at 4.2 K.

Figure 3-22 shows a topographic image of sample BW1 WW, taken at 4.2 K. This sample consists of Cr/Au gates on the surface of a GaAs/AlGaAs heterostructure. This image is plotted in perspective, and the roughness on the evaporated metal film is clearly visible above the noise level in the image. The gates are approximately 500 Å thick and the length of the image is 6.6 μm.

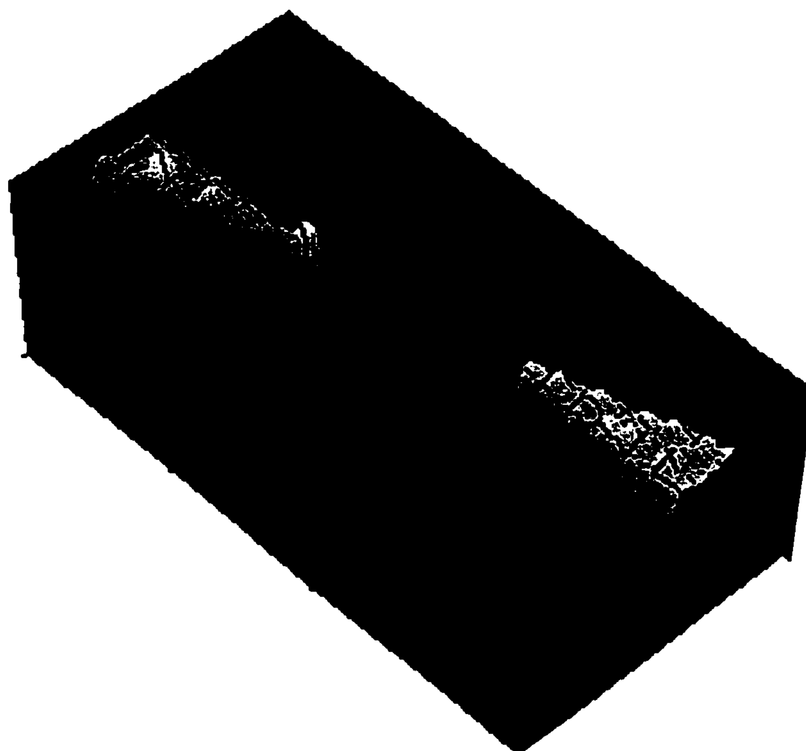

Figure 3-22 Topographic image of sample BW1 WW. The length of the image is 6.6 μm

Figure 3-23 shows a topographic image from our SPM taken at 4.2 K. The sample in this case is a calibration sample which was used to help determine the drift of our SPM on cooling from room temperature to 4.2 K. This sample is affectionately known as the "hieroglyphs," because each symbol corresponds to a position on the sample through a simple code.

The vertical noise level in each of these images is between 15 and 25 Å. Although this noise level is slightly higher than in many commercial AFMs, it is actually an

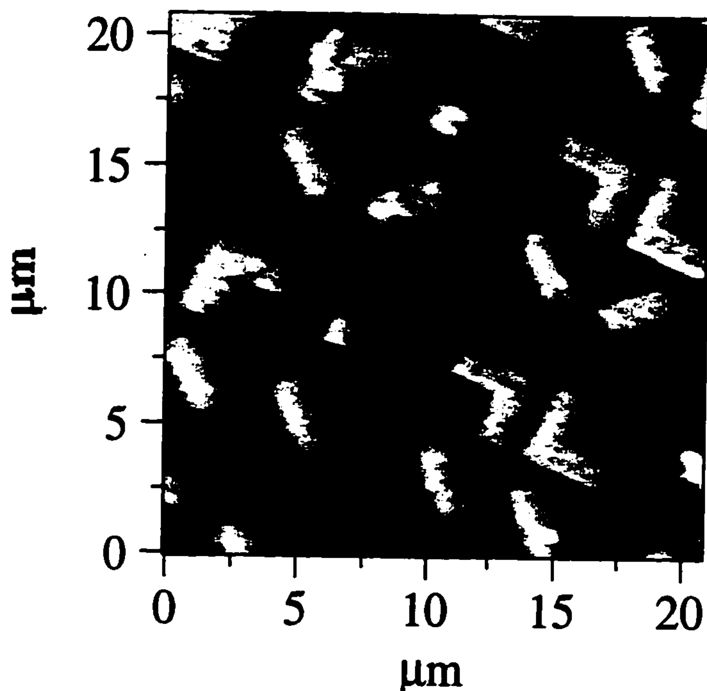

Figure 3-23 Topographic image of sample HG3 taken at 4.2 K.

excellent noise level for our application. The two dominant contributions to the noise level are the Johnson noise in the cantilever measurement circuit (see section 3.2.1), and vibration induced noise (see section 3.4). As previously discussed, these two contributions are larger in our application because of our constraint that the instrument have a long range and work at very low temperatures. The two steps which would most improve the noise level would be to place the entire bridge inside the Dewar, which is currently in progress, and to build or obtain a higher resonant frequency scanning element. Overall, the SPM images samples well, and any efforts to improve the SPM should instead focus on the experimental issues such as tip-sample alignment at low temperature (see chapter 6).

CHAPTER 4 Change in sheet density due to a biased SPM tip

An important concern in scanning probe experiments on subsurface 2DEGs is degradation of the resolution by the distance between the surface and the 2DEG. In typical heterostructures, the electron gas is located 50 nm or more beneath the surface, and the SPM tip cannot directly touch the electron gas or tunnel electrons into it. In this section we present calculations showing that, in spite of these restrictions, the resolution of scanning probe microscopy on subsurface 2DEGs can be very good. In fact, for our experimental system, the theoretical resolution of our current technique approaches the electron Fermi wavelength, which is one of the smallest natural length scales in the 2DEG system.[1]

1. This work has been previously published in less detail: M.A. Eriksson et al., *Superlattices and Microstructures* **20**, 435 (1996).

4.1 Geometry for the calculation

In order to understand the effect of the tip voltage on the 2DEG, and to understand the resolution limit of this microscopy, we calculate the charge induced in the 2DEG by a biased SPM tip using a classical electrostatic model. Figure 4-1 (a) is a schematic diagram of the geometry used in the calculation. The electron gas is modeled as a conducting sheet at a depth of d = 520Å beneath the surface of a $GaAs/Al_{0.3}Ga_{0.7}As$ heterostructure. The dielectric constant of the $Al_{0.3}Ga_{0.7}As$ layer between the tip and the electron gas is 12.24. We assume a tip height of 4 μm. The tip is modeled as a cone of half angle 10°, with a radius of curvature R_c at the tip which is varied in the calculation. The cantilever is at the same potential as the tip, because they are in electrical contact. These parameters are characteristic of the piezoresistive cantilevers used in our experiments.

Figure 4-1 (b) shows the contact area between the tip and the GaAs surface. When two deformable solids, like the SPM tip and the GaAs surface, come into contact, they touch in a circular disk. This was first shown by Hertz in the 19th century.[2] The deformation is not large for common tip-sample forces, but it is necessary to take into account the tip-sample deformation in order to understand the results from our calculations. For a tip with radius of curvature R_c, the formula for the contact radius R_0 is[3]

---

2. H. Hertz, *J. Math (Crelle's J.)* 92, 156 (1881).

3. C.J. Chen, *Introduction to Scanning Tunneling Microscopy*, Oxford University Press, New York (1993).

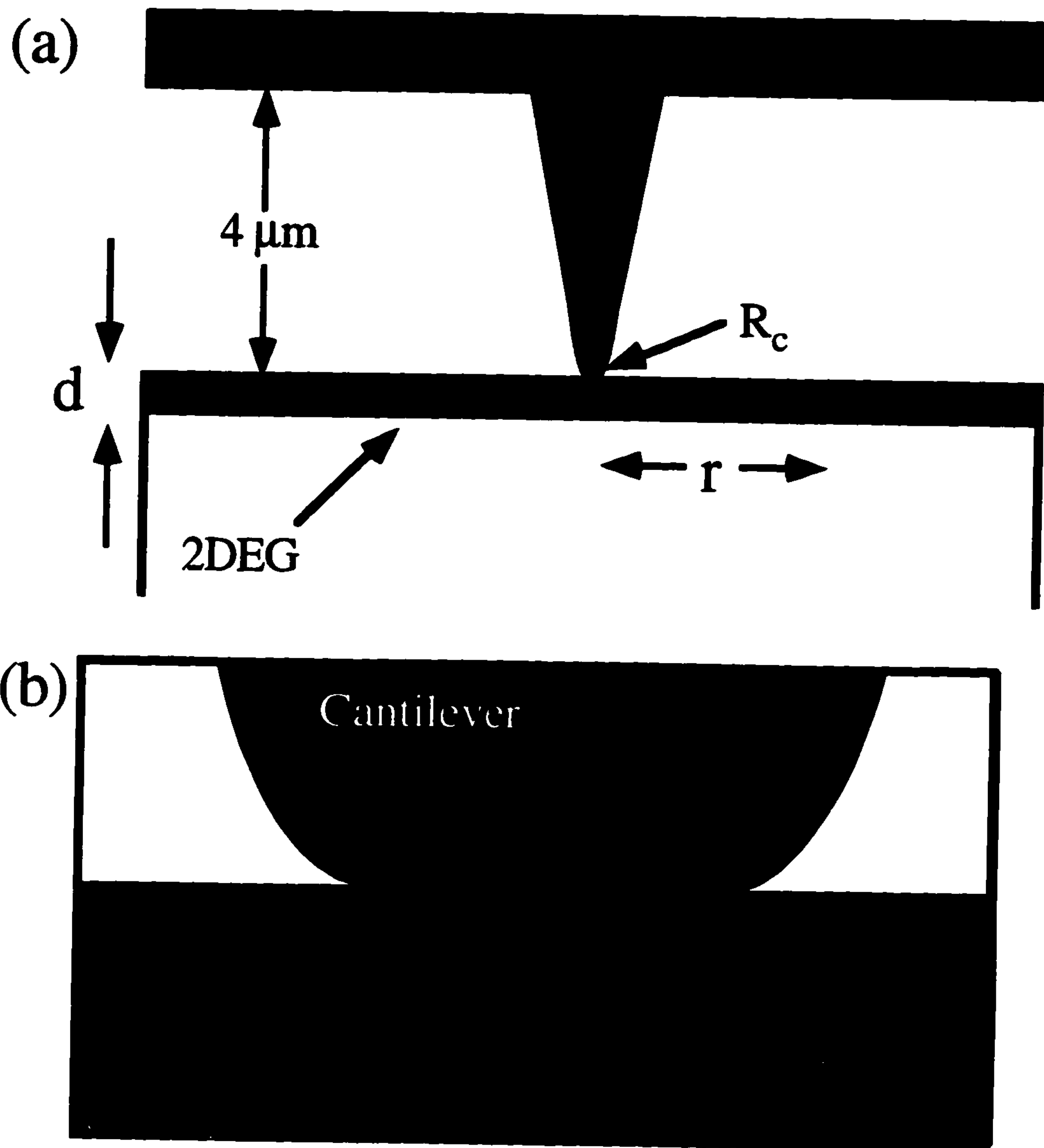

Figure 4-1 (a) Geometry for the calculations. The tip and cantilever are held at a fixed potential relative to the 2DEG.

(b) Close up schematic of the contact area between the tip and the sample. The radius R_0 of the contact area is indicated.

$$R_0 = \frac{1}{2}\left(\frac{6FR_c}{E^*}\right)^{\frac{1}{3}} \qquad \text{(EQ 13)}$$

where $E^* = \left[\frac{1-\upsilon_1{}^2}{E_1} + \frac{1-\upsilon_2{}^2}{E_2}\right]^{-1}$. Here E_1 and E_2 are Young's moduli for the tip and the sample respectively, υ_1 and υ_2 are Poisson's ratios for the two materials, and F is the applied force. In the calculations the tip is modeled as a hyperbola, truncated so that the correct contact area is obtained. This allows independent variation of the tip radius of curvature, the half-angle of the conical tip, and the contact area.

To calculate the electric field, we numerically solve the axially symmetric two-dimensional Laplace equation:[4]

$$\nabla^2\varphi = \frac{1}{r}\frac{\partial}{\partial r}\left(r\frac{\partial\varphi}{\partial r}\right) + \frac{\partial^2\varphi}{\partial z^2} = 0. \qquad \text{(EQ 14)}$$

The tip and the 2DEG are treated as conductors held at fixed potentials in the calculations, so Dirichlet boundary condition are used at both the tip and the electron gas. The calculation is therefore valid for voltages small enough that the electron gas remains continuous beneath the tip.

---

4. See, for example, J.D. Jackson, *Classical Electrodynamics*, John Wiley & Sons, New York (1975).

4.2 Sheet density perturbations

Figure 4-2 is a plot of the electrostatic potential beneath a tip with R_c = 500 Å and R_0 = 50 Å. The gray scale represents the magnitude of the potential, varying from one at the tip (z = 520 Å), to zero at the electron gas (z = 0). The solid lines are the equipotentials. Due to the large dielectric constant of the $Al_{0.3}Ga_{0.7}As$ layer, there is a severe kink in the equipotentials where they cross the vacuum-sample interface. In contrast, there is no bending of the equipotentials at the tip-sample interface: in this circular contact area, the electric field lines enter the heterostructure normal to the interface. The effect of the large dielectric coefficient in the $Al_{0.3}Ga_{0.7}As$ layer increases the resolution of our microscopy.

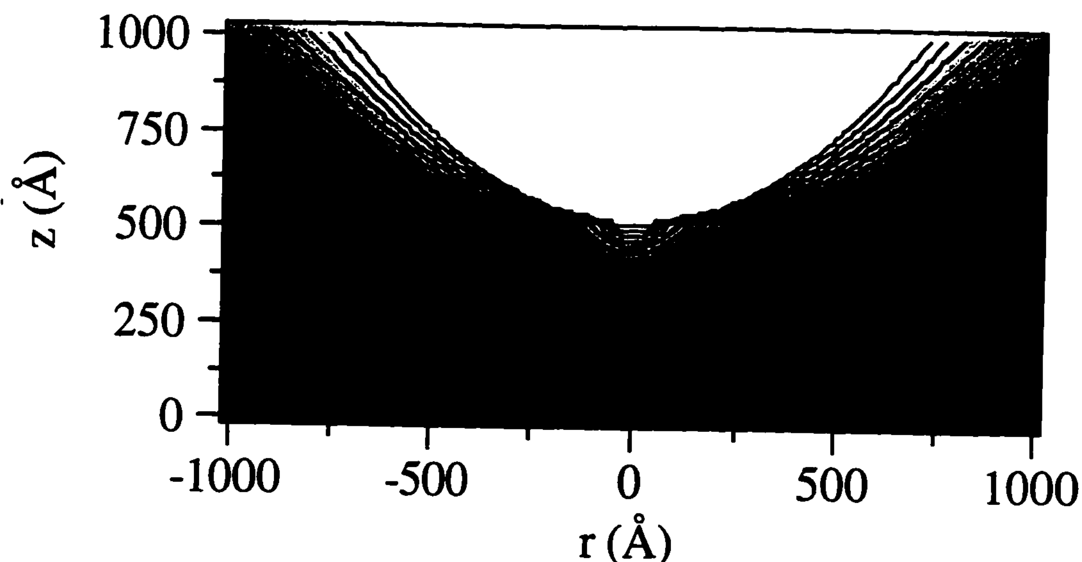

Figure 4-2 Grayscale and contour plot of the normalized electric potential between the tip and the 2DEG. R_0 = 50 Å, and R_c = 500 Å.

Figure 4-3 shows the induced change in density in the 2DEG directly beneath the tip due to the applied voltage for the case when $R_c = 500$ Å and $R_0 = 50$ Å. The calculation is cylindrically symmetric, so the actual density perturbation in the 2DEG may be obtained by spinning the plot in figure 4-3 about its central axis. The resolution of our microscopy is limited by the width of the induced density perturbation in the 2DEG. For $R_c = 500$ Å and $R_0 = 50$ Å, we find the half-width at half-maximum $\Delta r = 545$ Å, or approximately the electron gas depth ($d = 520$ Å in this calculation). Although large on an atomic scale, this resolution approaches the Fermi wavelength λ_F and inter-electron spacing $\sim\lambda_F/2$ of electrons in our two-dimensional electron gas systems.[5]

The half-width at half-maximum Δr of the change in sheet density does not depend sensitively on the tip radius of curvature or the applied force. Figure 4-4 shows Δr as a function of the contact radius R_0, and for three values of the tip radius of curvature, $R_c = 100$ Å, 500 Å, and 1000 Å. For contact radii smaller than ~ 200 Å, the half-width at half-maximum Δr is essentially constant and equal to the electron gas depth. For contact radii larger than 200 Å, Δr increases linearly with R_0. This is not surprising: when the contact diameter (= twice the contact radius) exceeds the gas depth, the half-width at half-maximum must increase, because the system now resembles a parallel plate capacitor.

---

5. For example, $\lambda_F \sim 450$ Å for $n_s = 3\times10^{11}$ cm^{-2}.

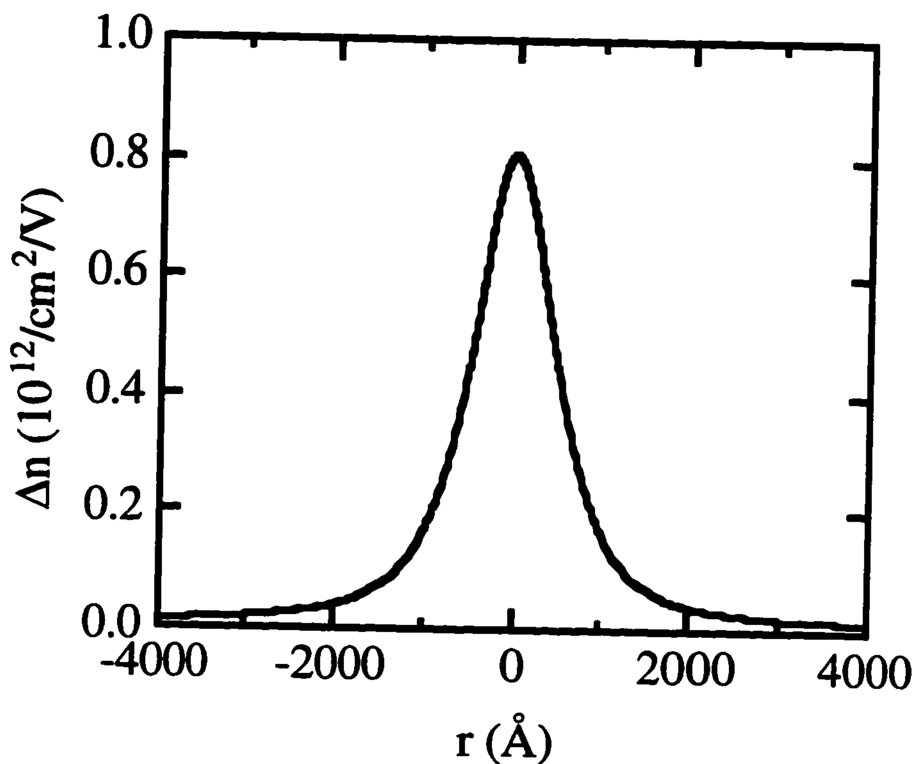

Figure 4-3 Change in sheet density beneath a voltage biased SPM tip as a function of radial distance in the 2DEG. R_0 = 50 Å, and R_c = 500 Å.

We were led to consider the contact area as a parameter in our calculations because our initial results showed that the half-width at half-maximum of the density perturbation was independent of tip radius of curvature. This is not physically reasonable, and the above discussion resolves the apparent paradox. The mechanism by which R_c increases the width Δr of the induced density perturbation is indirect. According to Eq. (13), a large R_c reduces the force required to generate a given contact area. Once the contact radius approaches the electron gas depth, further increases in

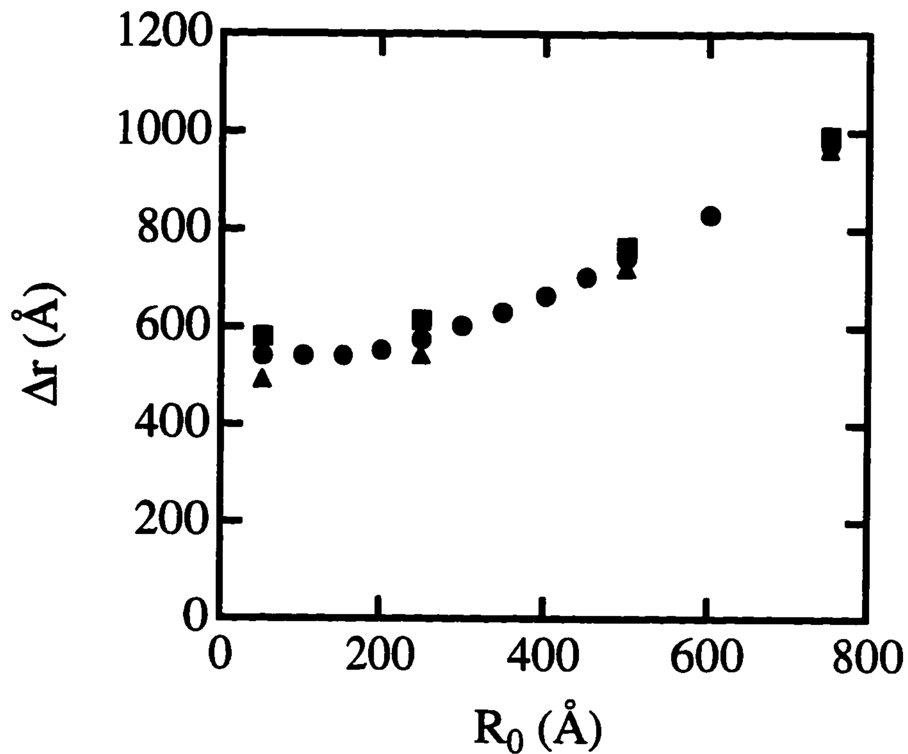

Figure 4-4 Half-width at half-maximum of the density perturbation as a function of contact radius.
squares correspond to R_c=1000Å
circles correspond to R_c=500Å
triangles correspond to R_c=100Å

contact area increase Δr, as shown in figure 4-4. In this way, increasing the tip radius of curvature will increase the half-width at half-maximum of the density perturbation, and degrade the resolution, for constant tip-sample force.

Figure 4-5 shows the contact diameter versus applied force for a series of tip radii of curvature (from Eq. (13)). Typical radii of curvature for the cantilevers used in our

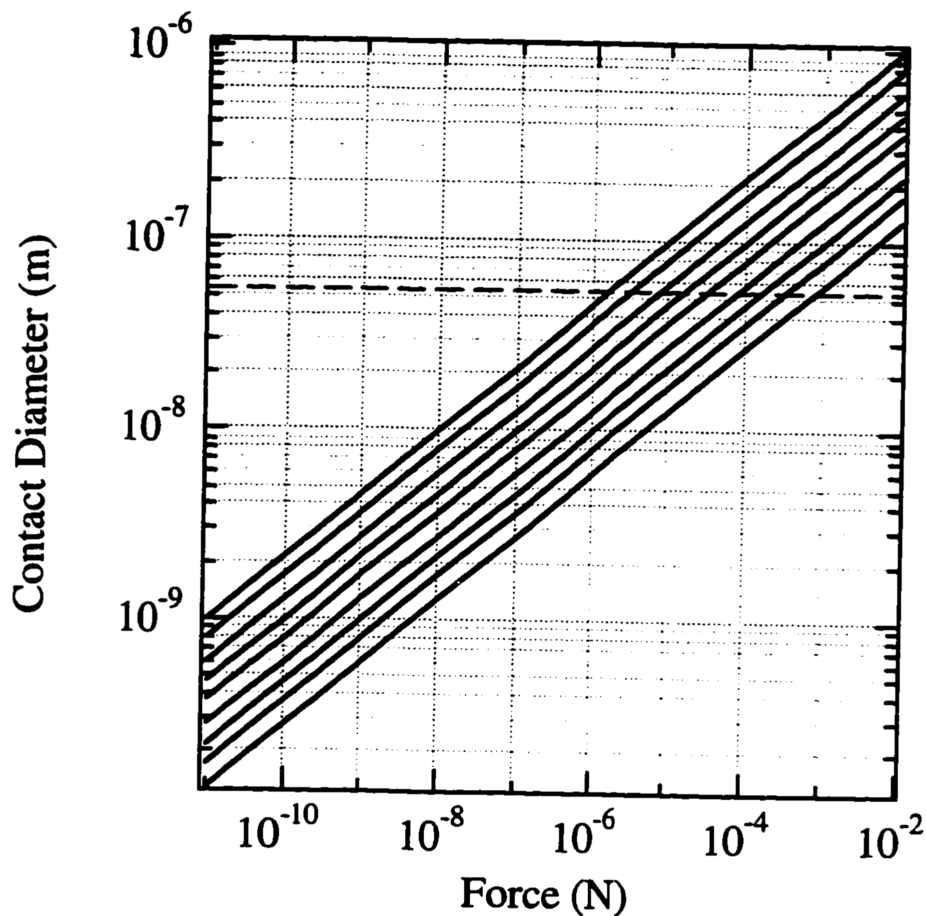

Figure 4-5 Contact diameter versus applied force. Solid lines are for tip radii of curvature from bottom to top of 20, 50, 100, 200, 500, 1000, 2000, 5000, and 10000 Å. The dotted line indicates a typical electron gas depth for our experiments of 520 Å.

experiments are about 100 Å. From figure 4-5 it is clear that it would require an enormous tip-sample force of more than 10^{-4} N to produce a contact diameter approaching the electron gas depth. Our experiments are thus well in the regime where the contact radius is smaller than the electron gas depth, which means the resolution

limit set by the tip-sample electrostatics is not sensitive to the details of any individual tip.

CHAPTER 5

Scanned gate imaging of point contact electronic properties

The goal in applying scanning probe microscopy to the study of subsurface semiconductor nanostructures is to gain information about electron transport which is difficult to obtain in traditional transport experiments. The questions which need to be addressed experimentally range from measurements of where the current flows and what the charge distribution is in 2DEG microstructures, to more difficult measurements such as measuring the wave functions of quantum states in small 2DEG devices. In this chapter we will present data and calculations on scanning probe measurements of transport through two-dimensional electron gas point contacts. These experiments are the first steps towards the use of scanned probe microscopy as a general imaging tool in the study of semiconductor nanostructures.[1,2]

5.1 Scanned gate experiments

The scanned probe technique which we chose to develop uses the sharp, conducting tip of an atomic force microscope as an additional, and moveable, surface gate. One of the advantages of nanostructure experiments in 2DEGs is that the experimentalist can adjust the size and shape of the nanostructure by changing the gate voltages which define the device. By using the tip of a scanning probe microscope as an additional surface gate, we have extended the ability to change the shape of a nanostructure to include the possibility of moving one of the defining gates during the experiment. The experiments we report here show the results of using this method to study microstructures at 4.2 K.

5.1.1 Introduction

Figure 5-1 is a schematic diagram of a scanned gate experiment. The imaging experiments which we present here consist of two simultaneous measurements. First, we measure the topography of the sample using our SPM as an atomic force microscope at 4.2 K. Second, we measure the resistance of the 2DEG nanostructure as a function of the tip position. The tip is voltage biased relative to the 2DEG, so that it serves as an additional, and moveable, surface gate. Because the 2DEG sheet density is locally enhanced or reduced by the tip voltage, the resistance of the nanostructure will be modified in a way which depends on the tip position. Previous experiments have shown

---

1. M.A. Eriksson et al., *Appl. Phys. Lett.* **69**, 671 (1996).
2. M.A. Eriksson et al., *Superlattices and Microstructures* **20**, 435 (1996).

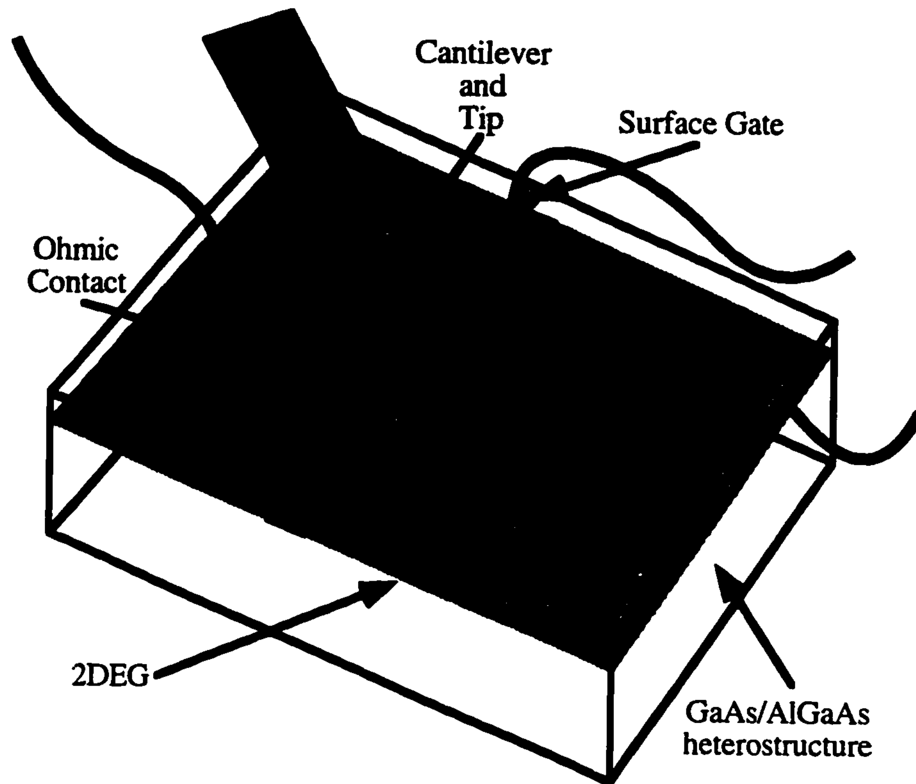

Figure 5-1 Scanned gate experiments. The tip is voltage biased with respect to the 2DEG.

that modulations in the sheet density near a point contact can have a dramatic effect on the resistance of the point contact.[3,4] We use this effect in our experiments to generate images of the transport properties of the point contact, and theoretical calculations show that even the details of the electron wave functions near the point contact may be imaged with our technique.

3. J.A. Katine, M.A. Eriksson, A.S. Adourian, R.M. Westervelt, J.D. Edwards, A. Lupu-Sax, E.J. Heller, K.L. Campman, and A.C. Gossard, to be submitted.

4. M.J. Berry, J.A. Katine, R.M. Westervelt, and A.C. Gossard, *Phys. Rev. B* **50**, 17721 (1994).

5.1.2 AC versus DC perturbations

It is important to distinguish between two types of scanned gate measurements: those in which the tip voltage is kept constant, and those in which the tip voltage is oscillated. When the tip voltage is held constant, the experiment consists of measuring the resistance of the point contact as a function of the tip position. When the voltage is oscillated, the experiment involves measuring the sample voltage at the frequency of oscillation. The advantage of the ac technique is that it ensures that the experiment will only measure the effect of the tip voltage on the 2DEG, and that other perturbations of the point contact resistance will have little affect.

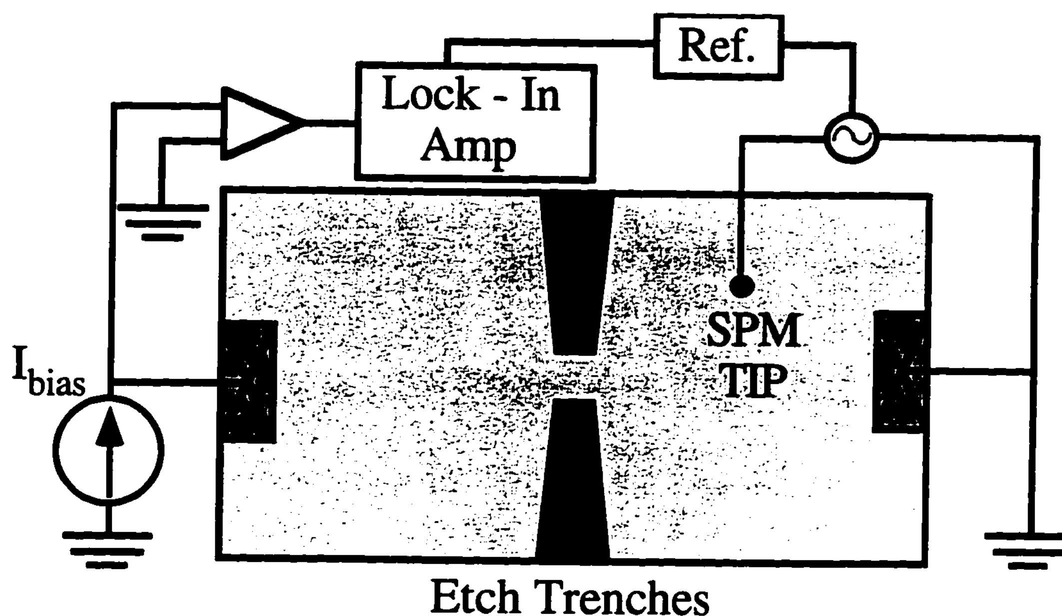

Figure 5-2 **AC tip voltage technique.**

Figure 5-2 shows the measurement schematic for the experiment presented in the next section. The point contact is dc current biased, and the tip voltage is oscillated at a frequency f: typically f ~ 400 Hz. The sample voltage is measured by a lockin amplifier. When we measure the sample voltage at frequency f, we measure the change in resistance due to the voltage applied to the SPM tip, as confirmed experimentally in section 5.2.

5.2 Classical ballistic point contacts

In this section we present experimental results obtained using scanning probe microscopy to study transport through a microfabricated ballistic point contact at 4.2 K.

5.2.1 Motivation

Our goal in performing experiments on classical, ballistic point contacts is to test the experimental viability of scanned gate experiments on subsurface 2DEGs. Point contacts are good candidates for these experiments because they are relatively simple to fabricate, and they are well understood — at least in terms of the traditional transport measurements which are usually performed on semiconductor nanostructures.

Point contacts whose dimensions are smaller than the mean free path have a conductance which is proportional to their cross section. Sharvin[5] was the first to present a formula for the conductance of a classical *three* dimensional ballistic point

5. Yu. V. Sharvin. *Sov. Phys. JETP* **21**, 655 (1965).

contact: $G = \frac{2e^2}{h}\frac{k_F^2 S}{4\pi}$, where S is the area of the point contact. The 2-D analog of this equation which is appropriate for our 2DEG system is[6]

$$G = \frac{2e^2}{h}\frac{k_F W}{\pi}, \qquad \text{(EQ 15)}$$

where W is the point contact width, k_F is the Fermi wavevector, and we have assumed the usual two-fold spin degeneracy. Eq. (15) is the classical limit of the (ironically) more familiar quantum point contact conductance formula $G = \frac{2e^2}{h} N$, where N is the number of modes in the point contact. For wide point contacts $N \rightarrow \frac{k_F W}{\pi}$.

The power and appeal of scanning probe methods is that they provide a means of imaging an experimental system. We will see in the following sections that our scanned gate experiments provide an image of the current flow through a classical ballistic point contact — perhaps the simplest mesoscopic device.

5.2.2 Sample

The sample in this experiment is an etched point contact in a near surface (520 Å deep), high mobility (μ = 540,000 cm^2/Vs) two-dimensional electron gas. Figure 5-3 is a topographic image of sample KC8-F taken with our SPM at room temperature.[7] The dark regions in the image are the etch trenches which define the point contact; the etch

6. C.W.J. Beenakker and H. van Houten, *Quantum Transport in Semiconductor Nanostructures*, in *Solid State Physics* 44, ed. by Henry Ehrenreich and David Turnbull, Academic Press, Inc., San Diego (1991).

trenches are approximately 1000 Å deep. The sheet density in this sample at 4.2 K is $n_s = 3.0\times10^{11}cm^{-2}$. From the mobility and the sheet density we can determine the mean free path $\ell = 5.0\ \mu m$. This sample was fabricated using electron beam lithography to open windows in a PMMA resist, and then the $GaAs/Al_{0.3}Ga_{0.7}As$ heterostructure was etched using a citric etch at 50 °C.[8] From Eq. (15) the resistance of the point contact at 4.2 K is approximately 100 Ω.

Figure 5-3 AFM image of sample KC8-F.

7. The sample naming convention is that the first letters and number (KC8, in this case) refer to the wafer, and the following letter (F, in this case) refers to the specific location of the chip on the wafer, as recorded in our wafer log book.

8. For details of the citric etch procedure see D.J. Mar, Ph.D. Thesis, Harvard University (1994).

5.2.3 Change in resistance images.

Figure 5-4 is an image of the change in resistance[9] of the point contact in KC8-F as a function of the tip position. The full gray scale in the image is 2.0 Ω, and the black lines superimposed on the image are the edges of the etch trenches which define the point contact, taken from a simultaneously acquired topographic image. The dc current bias for this image was 3 μA. The tip voltage was 0.5 V rms at 400 Hz, and there is also an effective dc voltage due to the contact potential between the tip and the 2DEG. We are not sensitive to the contact potential because of the ac technique we are using in this experiment. The peak change in resistance of 2.0 Ω corresponds to 2 % of the point contact resistance, indicating that the measurement is a weak perturbation on the current flow through the point contact.

Some of the features in figure 5-4 are easily understood. First, when the tip is far from the point contact, the image is essentially flat. This is because the point contact is the dominant source of resistance, and small changes to the sample far from the point contact will have a negligible effect on the sample resistance. Second, when the tip is in the center of the point contact, we see a large peak. Modulating the sheet density in the point contact itself is equivalent to modulating the width of the point contact, so from Eq. (15) we expect to see a large change in resistance. In order to understand the peak

---

[9] An experimental justification for the term "change in resistance image" is given in section 5.2.4, but for now we will simply refer to the motivation given in the opening section of this chapter.

Figure 5-4 Change in resistance image of sample KC8-F. V_{tip} = 0.5 V rms, I_{bias} = 3 μA. The full gray scale is 2.0 Ω.

shape in more detail, we will present a model of the mechanism for the change in resistance in section 5.2.4.

Figure 5-5 is a resistance scan with the same parameters as figure 5-4, except that the tip voltage is reduced to 0.2 V rms. The full gray scale in the image is 0.75 Ω. The two images are very similar and give a measure of the repeatability of the imaging technique.

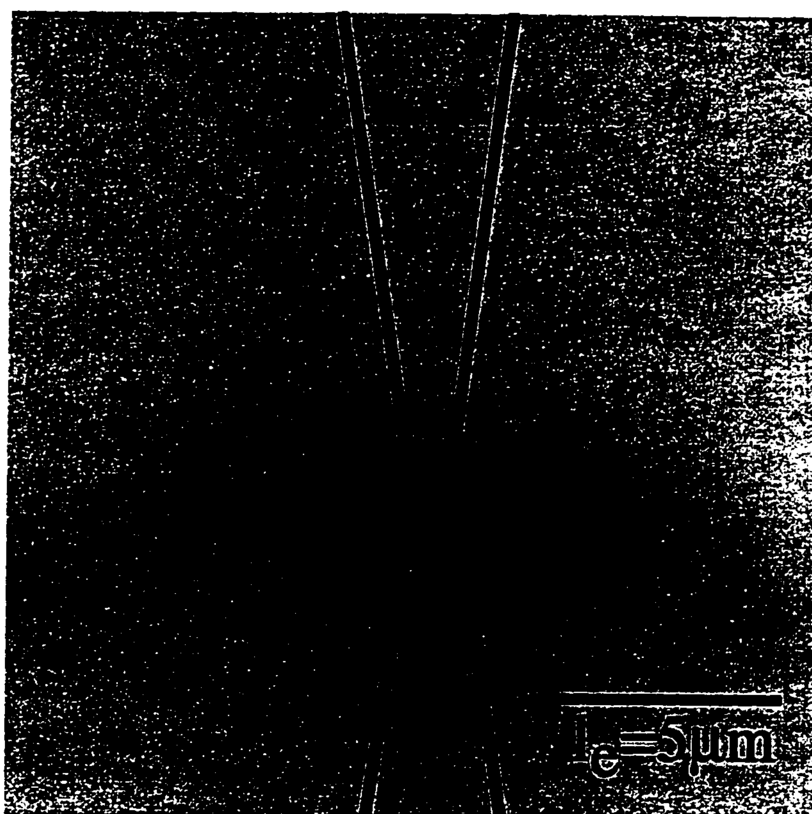

Figure 5-5 Change in resistance image of sample KC8-F with V_{tip} = 0.2 V rms, and I_{bias} = 3 μA. The full gray scale is 0.75 Ω.

5.2.4 The contrast mechanism

In the initial presentation of the data I have assumed that the contrast mechanism in the images shown in figure 5-4 and figure 5-5 is a change in resistance of the point contact due to a perturbation by the SPM tip. This needs to be confirmed experimentally. A good test of whether or not the contrast mechanism is a change in resistance is that the contrast should disappear when the bias current is reduced to zero. Figure 5-6 is an image taken with exactly the same conditions as those for the data shown in figure 5-4, except that now the dc bias current is reduced to zero. The gray scales are identical for the two plots, and the contrast is now completely removed.

Another important characterization of our measurement technique is to measure the maximum change in resistance in figure 5-4 (the height of the peak in the point contact) as a function of the size of the ac tip voltage. Figure 5-7 is a plot of the height of the change in resistance peak as a function of the applied ac tip voltage. The squares indicate the data acquired while increasing the tip voltage monotonically. The circles indicate the data taken while reducing the tip voltage monotonically. The peak height is observed to depend linearly on the applied tip voltage. A line fit to the squares gives a calibration of 0.62 Ω/V, and a line fit to the circles gives a calibration of 0.65 Ω/V.

Figure 5-8 shows the dc resistance of the point contact as a function of the dc voltage applied to the tip. The data in figure 5-8 were acquired with the tip centered in the middle of the point contact. Again, a linear dependence of the change in resistance on

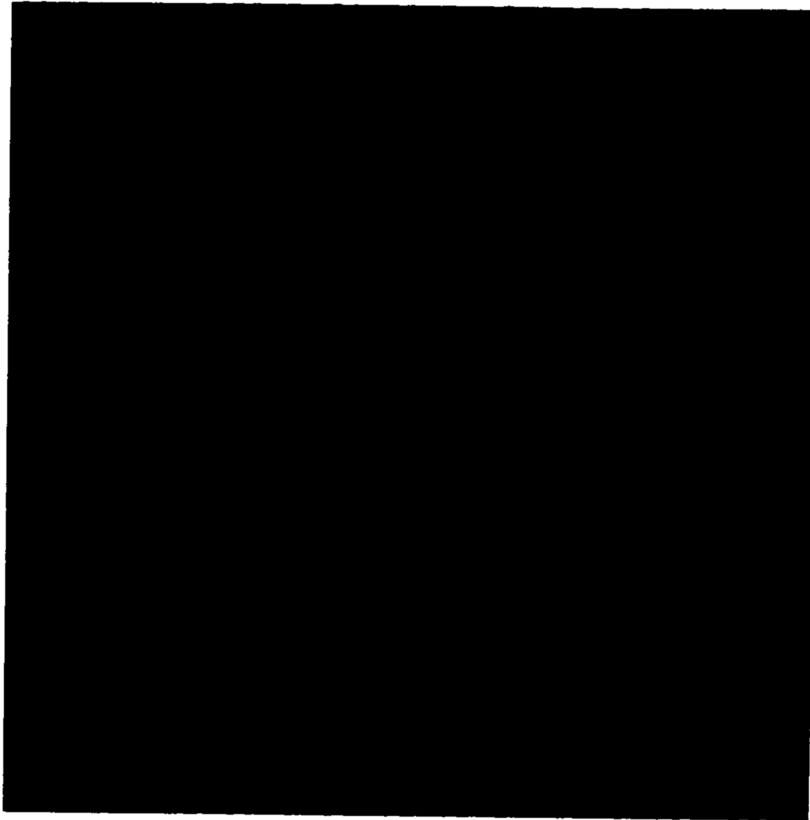

Figure 5-6 Zero bias current change in resistance image. The tip voltage was 0.5 V rms, and the gray scale is identical to that in figure 5-4.

tip-voltage is observed. The absolute value of the slope of the linear fit to the data is 0.52 Ω/V, which compares favorably with the ac results of 0.62 and 0.65 Ω/V obtained from figure 5-7.

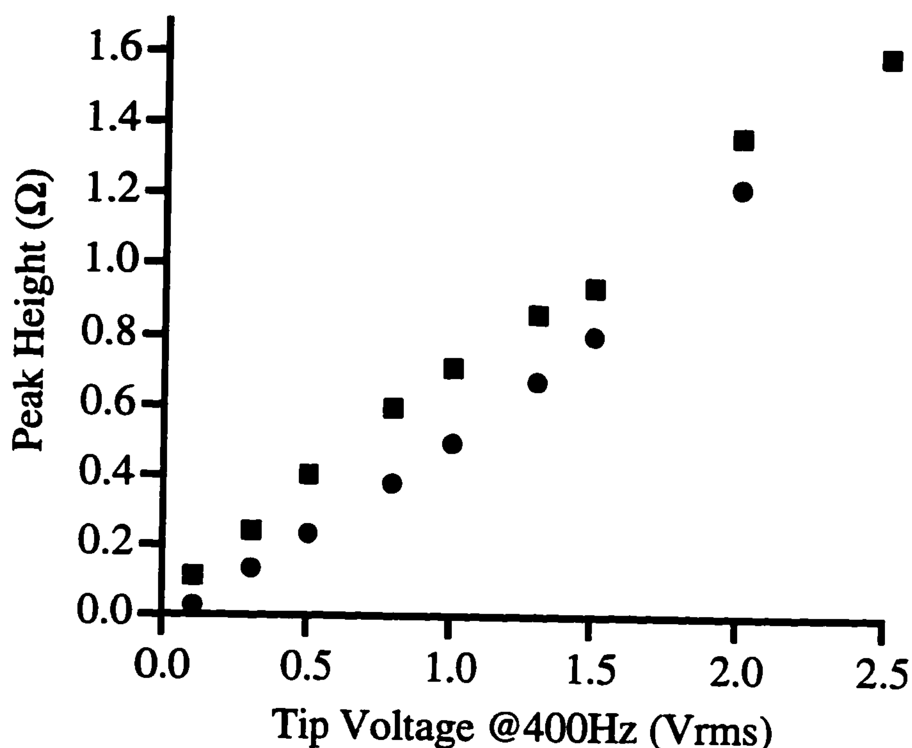

Figure 5-7 Peak height (as in figure 5-4) vs. tip voltage. Squares are the measured peak height while increasing the tip voltage, and circles correspond to decreasing the tip voltage from its maximum value.

Finally, there is a constant background in figure 5-4 which needs to be characterized. Figure 5-9 is a plot of the background level as a function of the root mean square (rms) voltage applied to the SPM tip. The background level is observed to depend linearly on the rms tip voltage. This background can be understood by taking into account the capacitive coupling between the Dewar wires. The tip voltage is applied at a frequency

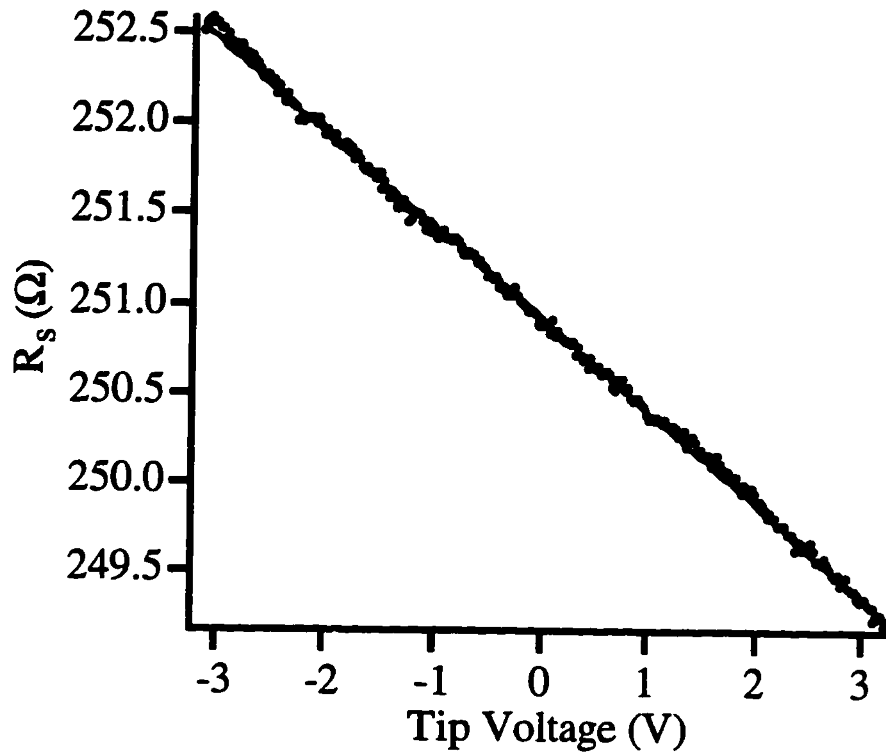

Figure 5-8 DC resistance versus tip voltage. The tip was centered in the middle of the point contact of figure 5-3. The bias current was 3 μA, and R_s is the sample resistance.

of 400 Hz. Parasitic capacitance, C_p, between the Dewar wires will act as a voltage divider between the applied tip voltage and the resistance from the sample to ground, R_{sg}. The measured background voltage will then be given by $V_{bkg} = V_{tip} \times \frac{R_{sg}}{Z_p}$, where $|Z_p| = \frac{1}{\omega C_p}$. The resistance to ground is on the order of 100 Ω. The slope of the

linear fit to the data in figure 5-9 is 1.00×10^{-6}. Therefore the parasitic capacitance must give an impedance which is of order $Z_p = 100 M\Omega$. This corresponds to a parasitic capacitance between the lines of $C_p = \frac{1}{\omega Z_p} \approx 4\ pF$. This is a very reasonable level of capacitance between the Dewar wires. The peak in figure 5-4 rises by a factor of 100 above the background fluctuations. Given the signal to noise level of 100 to 1, and the reasonable value of the interlead capacitance calculated above, we feel the background level is well understood.

5.2.5 Scattering model and peak profiles

Although the general trends in the resistance images plotted in figure 5-4 and figure 5-5 are easily understood by appealing to the concept that the point contact is the dominant source of resistance in the experiment, a better understanding of the data can be obtained by developing a simple model for the change in resistance.

Figure 5-10 (a) is a schematic diagram which conveys the idea behind our explanation for the change in resistance. The calculations presented in chapter 4 clearly showed that the sheet density perturbation due to the voltage biased SPM tip would be localized directly beneath the SPM tip, with a width which was comparable to the electron gas depth. The gas depth, d = 520 Å, is much less than the mean free path for electron transport, $\ell = 5.0\ \mu m$, so any model describing the effect of the tip on the point contact resistance must be a scattering model. To understand the peak shape in the resistance

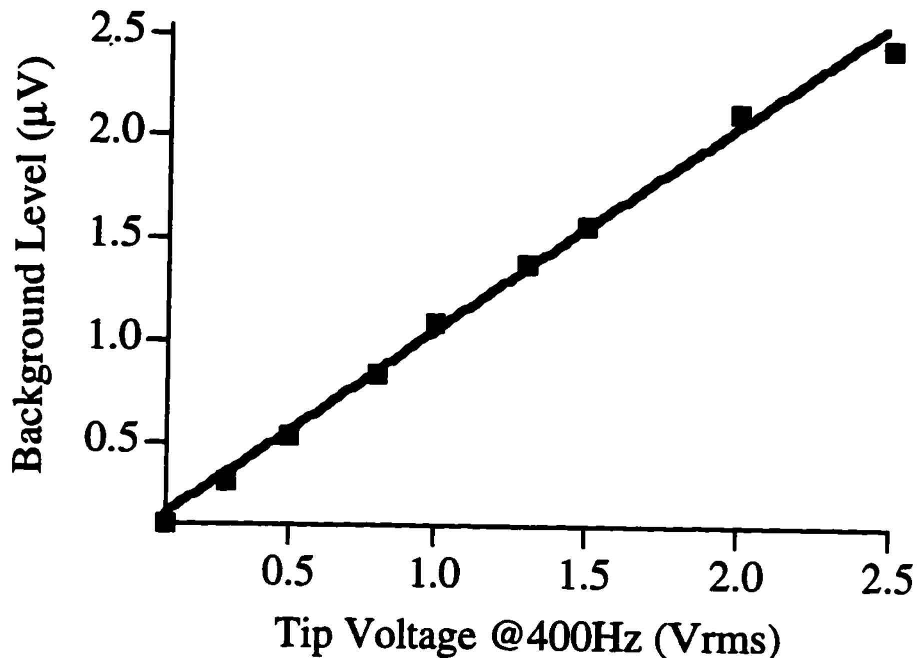

Figure 5-9 Background voltage in figure 5-4 as a function of the voltage applied to the SPM tip. The background voltage is the sample voltage observed to be independent of the tip position, on top of which the features in figure 5-4 are visible. The solid line is a linear fit to the data. The background is observed to depend linearly on the applied tip voltage.

images we assume the simplest model, that the tip induces additional scattering of electrons at its position. If we assume the scattering is 100 % effective in reversing trajectories when the tip is in the middle of the point contact, then the peak height corresponding to 2 % of the point contact resistance in figure 5-4 corresponds to a scattering cross section (a length in two dimensions) which is 2 % of the point contact width, or 600 Å. This compares favorably with the expected width of twice the electron

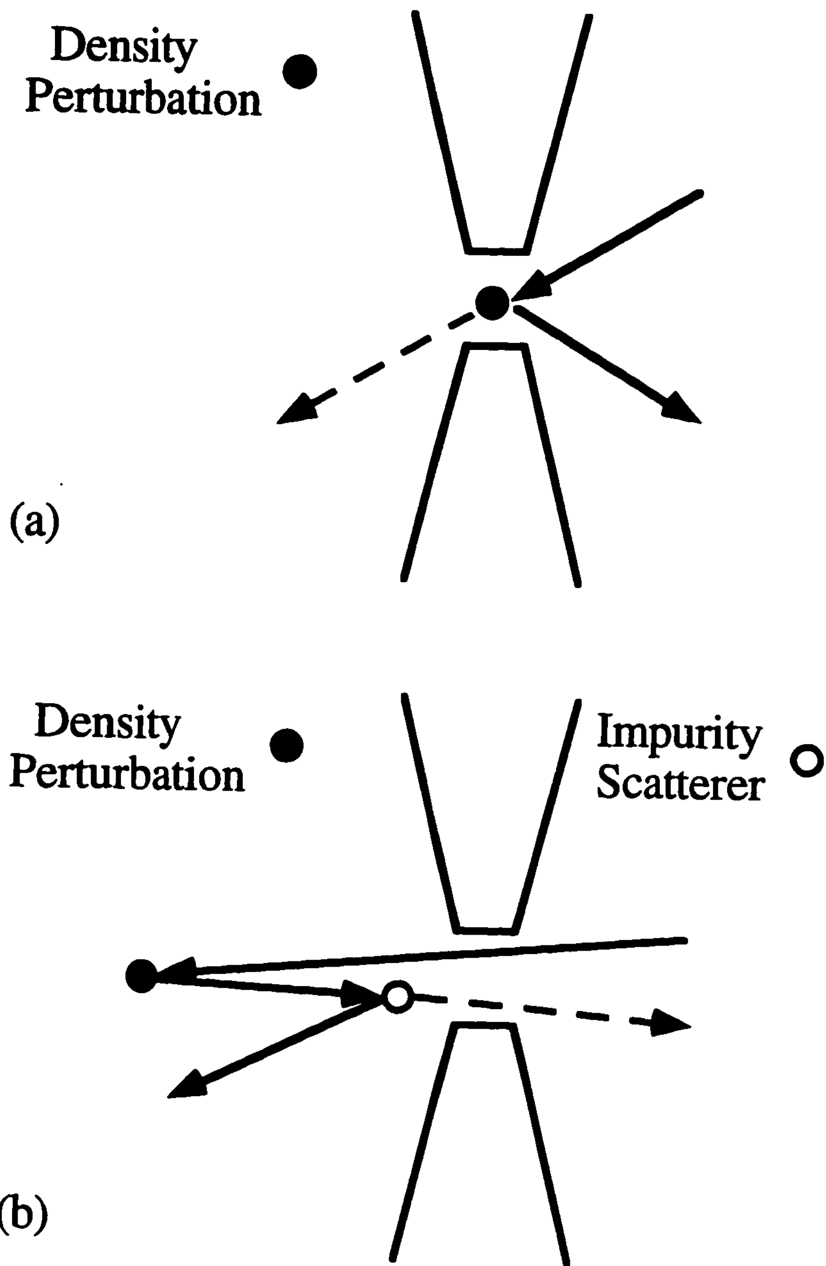

Figure 5-10 Scattering model.

gas depth, or 1040 Å. We would not expect exact agreement since the calculation in chapter 4 assumed no depletion beneath the SPM tip.

Figure 5-11 is a semilog plot of a line trace extracted from the change in resistance image in figure 5-4, as identified by the arrow in the reproduction of that data set. The data fall along a straight line on the semilog plot, indicating an exponential decay of the change in resistance. Figure 5-10 (b) indicates an heuristic explanation for this exponential fall-off. As the tip moves into the reservoir on one side of the point contact, scattering intrinsic to the 2DEG becomes more important in determining how effective the tip induced sheet density modulation is in changing the point contact resistance. The intrinsic scattering in the 2DEG is indicated by a point scatterer in figure 5-10 (b), but small angle scattering is experimentally more important. The scattering in the 2DEG will randomize trajectories on a length scale given by the mean free path. The tip will change the resistance of the point contact only when it reverses trajectories which would have traversed the point contact, as in figure 5-10 (a). The tip will therefore only have a large effect on the point contact resistance when electrons can travel ballistically from the point contact, to the tip, and back to the point contact. The peak should therefore decay exponentially with a decay length of half the mean free path, $\ell / 2 = 2.5$ μm. The observed decay length of 2.8 μm is in reasonable agreement with this value.

The model presented above gives an explanation of why the peak is observed to fall off exponentially, but clearly a more detailed model will be needed for future

experiments. Such a model would be difficult to develop for the present data, because the current flow through the point contact does not appear to be uniform. If the current flow were uniform, then the data would show a broad peak across the entire width of the point contact in figure 5-4. Instead, we observe a peak in the center of the point contact which falls off near the edges of the point contact. However, detailed calculations predicting the tip effect on the resistance of nanostructures in the *quantum* limit have been performed by students in Professor Heller's group, and some important results from these calculations, predicting that single quantum states may be resolved with our technique, will be presented in section 5.3.

The shape of the change in resistance peak in figure 5-4 images an important effect in point contacts which has been known for a number of years: point contact collimation.[10] The usual model of electron transport through point contacts predicts a cosine distribution of transmitted flux.[6] Flaring at the entrance or exit of a point contact, or a change in sheet density (a barrier) in the point contact itself, will reject higher angle trajectories, producing a distribution of transmitted flux which is peaked at small angles — in other words, it will collimate the transmitted flux.[6]

Figure 5-12 is a plot of the change in resistance along a circular arc 4 μm from the center of the point contact, as indicated on the change in resistance image. The change in resistance shows a peak in the forward direction of half-width 20°. This peak is a

---

10. L.W. Molenkamp, et al., *Phys. Rev. B* 41, 1274 (1990).

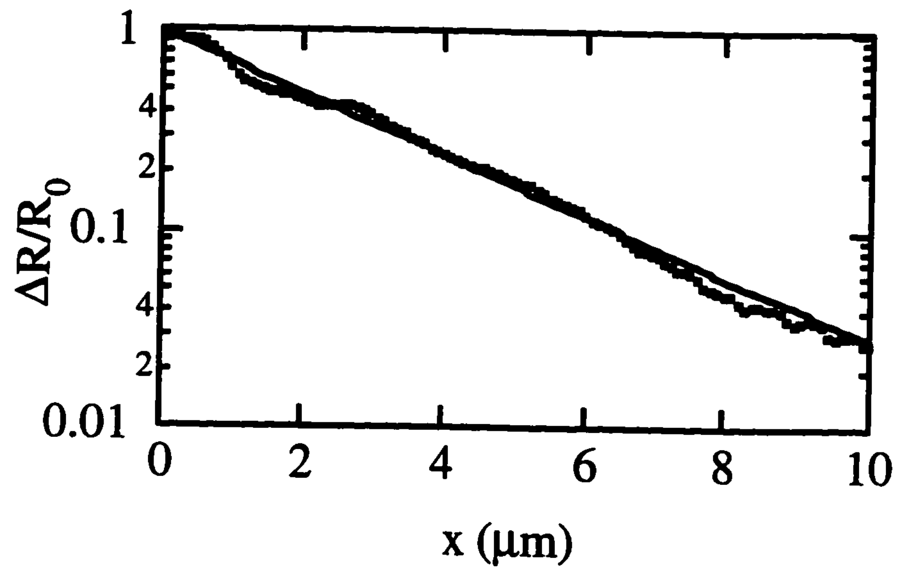

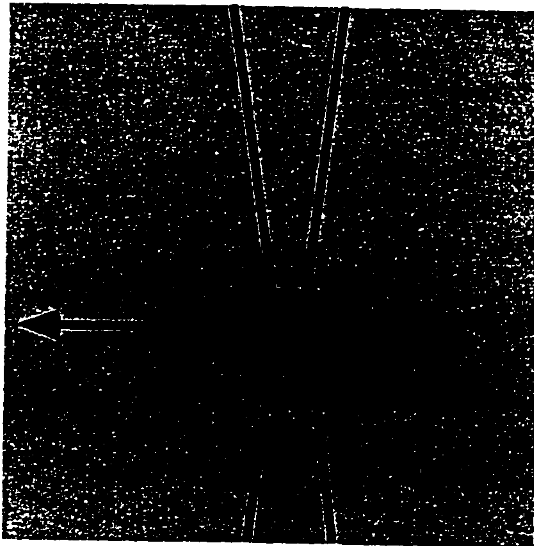

Figure 5-11 Change in resistance versus distance from the center of the point contact along the line indicated on the resistance image. The data is the same as that shown in figure 5-4.

direct image of collimation in the point contact. Although point contact collimation has been known for some time, the original experiments which discovered the collimation effect required specialized gate geometries and a magnetic field in order to observe the effect. One of the goals of this work is to develop a more general imaging approach to studying electron transport. It is valuable to be able to image effects such as point contact collimation in any nanostructure, without specialized gate structures and experiments.

5.3 Quantum point contacts

In this section we present some recent theoretical calculations on the possibility of imaging electron wavefunctions in a point contact-cavity system with our scanned gate microscopy.[3,11]

5.3.1 Motivation and theory

The quantization of the conductance of a point contact was first discovered independently by two groups in 1988.[12,13] Figure 5-13 is a conductance versus gate voltage trace for a quantum point contact, fabricated from wafer KC9; the data were taken at a temperature of 4.2 K. The quantum point contact in this case is part of a series array of 12 point contacts which was fabricated to make alignment of the SPM at low temperatures less critical. The conductance of the point contact is clearly quantized in

---

11. J. Edwards et al., to be published.

12. B.J. van Wees, H. van Houten, C.W.J. Beenakker, J.G. Williamson, L.P. Kouwenhoven, D. van der Marel, and C.T. Foxen, *Phys. Rev. Lett.* **60**, 848 (1988).

13. D.A. Wharam, T.J. Thornton, R. Newbury, M. Pepper, H. Ahmed, J.E.F. Frost, D.G. Hasko, D.C. Peacock, D.A. Ritchie, and G.A.C. Jones, *J. Phys. C* **21**, L209 (1988).

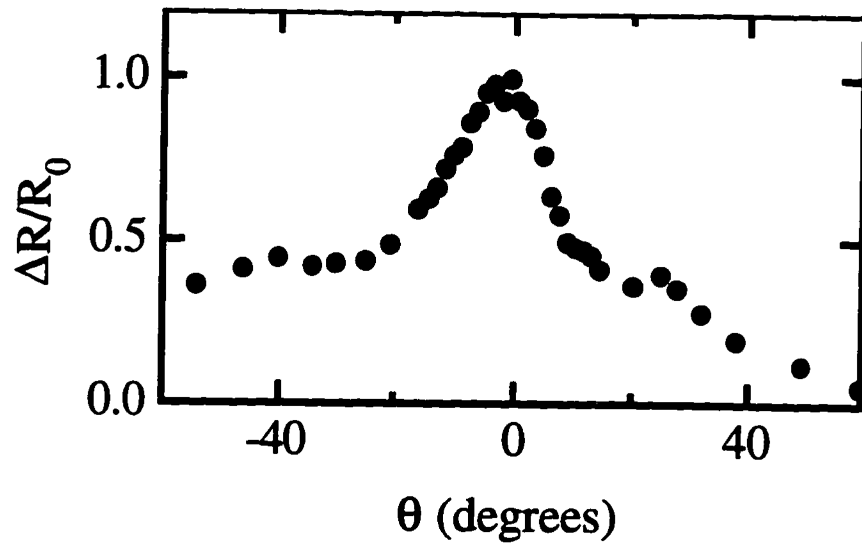

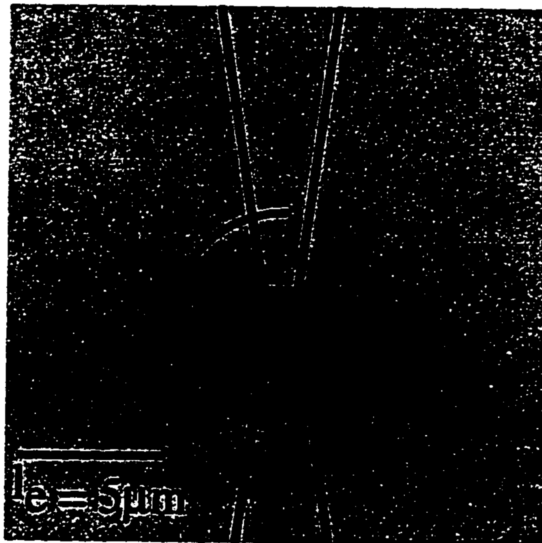

Figure 5-12 Angular dependence of the change in resistance. The data is the same as in figure 5-4, and the angular plot is from the data along the circular arc indicated on the change in resistance image.

units of $2e^2/h$. The rounding of the steps is due to the warm temperature at which this trace was taken, and is one motivation for moving the SPM to a Dewar capable of lower temperature operation (see chapter 6).

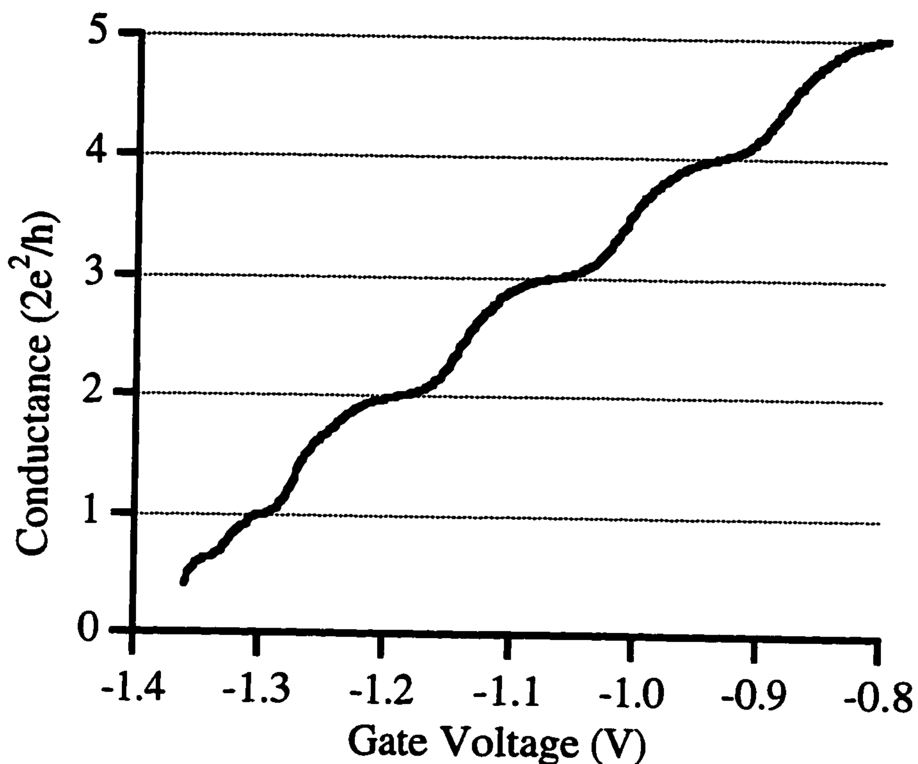

Figure 5-13 Conductance of a quantum point contact at 4.2 K. A background resistance of 125 Ω is subtracted from the curve.

The quantization of the conductance through point contacts at low temperatures follows from the quantization of the number of transverse modes in the channel of the point contact. Because the channel has a finite width, the density of states in the channel splits into a series of one-dimensional subbands. Each spin degenerate subband will

contribute one conductance quantum, $G_{mode} = \frac{2e^2}{h}$, to the conductance of the point contact.[6] The total conductance of the point contact is then given by

$$G = N\frac{2e^2}{h}, \qquad \text{(EQ 16)}$$

where N is the number of occupied modes in the point contact. Eq. (15), for the conductance of a point contact in the classical ballistic limit, is the large N limit of Eq. (16), which is seen by identifying $N = \frac{k_F W}{\pi}$.

One of the motivations for studying quantum point contacts is that they provide a good opportunity to study coherent effects in two-dimensional electron systems. Figure 5-14 is an SEM micrograph of a nanostructure used in a recent (non-SPM) experiment which showed the existence of sharp resonances in an open cavity.[3] One of the successes of this experiment was the reproduction of the experimentally measured conductance by theoretical calculations which identified specific resonant modes in the nanostructure.[3] These calculations have recently been extended to analyze the possible spatial profiling of the resonant modes by a scanned gate experiment of the type presented in this chapter.[11]

5.3.2 Theoretical predictions

Figure 5-15 is a plot of one of the resonant modes of a nanostructure like that shown in figure 5-14. The plot only includes the upper half of the mode, because of the mirror

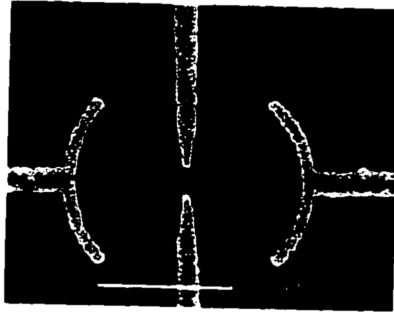

Figure 5-14 SEM micrograph of the nanostructure used in the experiment of Katine et al.[3]

symmetry of the device. One of the long term goals of the microscopy we have described in this chapter is to image this type of resonance in a two-dimensional electron gas.

Figure 5-16 (a) is a close up of the resonance plotted in figure 5-15. In order to model our experiment the tip is assumed to create a hardwalled depletion region of finite width directly beneath the tip. Figure 5-16 (b) is a plot of the change in resistance as a function of the tip position, assuming a depletion region of width $\lambda_F/8$ — an optimistic assumption. The structure of the resonance is rounded by the size of the tip, but the structure of the probability distribution is clearly visible. In order to achieve a resolution of $\lambda_F/8$, two improvements need to be made in our experiment. First, we will have

Figure 5-15 Theoretical plot of a resonance from a nanostructure similar to that shown in figure 5-14.[11]

obtain two-dimensional electron gases which are closer to the surface. This will improve the resolution by decreasing the diameter of the tip perturbation in the 2DEG (see chapter 4). Second, we will need 2DEGs with lower sheet density. This will increase λ_F, and thereby increase the effective resolution of the microscopy.

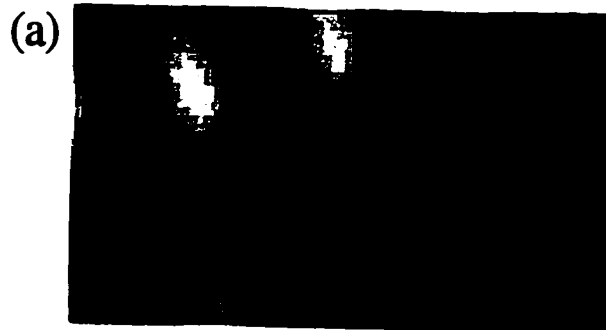

Figure 5-16 **(a) Close up of the nodal structure in the resonance of figure 5-15. (b) Theoretically predicted change in resistance as a function of tip position, assuming a depletion region of width $\lambda_F/8$ beneath the SPM tip.**[a]

a. Calculations from J. Edwards et al.[11]

CHAPTER 6 Conclusions and future directions

In this thesis we have demonstrated a scanning probe technique for studying semiconductor nanostructures at low temperatures.

It is worthwhile mentioning two improvements which could be made to our scanning probe microscope. First, our current instrument relies on the repeatability of thermal drifts on the cooldown from room temperature to 4.2 K in order to align the tip with a nanostructure. Although I have done this successfully many times, it remains the rate limiting step in our experiments. It is sometimes necessary to cool the Dewar many times in order to find the nanostructure. The best solution which I am aware of is to install an inertial slider on the sample holder. Inertial sliders work on the principle that an object can be made to travel across a surface if the surface is moved slowly in one

direction, and then rapidly accelerated in the opposite direction. There are many designs in the literature, and this would allow much faster turn around times for our experiments.

The second improvement is to put the existing SPM stage in a Dewar which is capable of achieving lower temperatures. The current Dewar can reach 1.4 K, but a temperature of 300 mK or lower would greatly enhance the ability to perform experiments requiring phase coherence in the electron gas.[1]

Three ideas for future experiments studying nanostructures with the scanned gate technique developed in this thesis deserve special mention. First, experiments are already underway which are looking at quantum point contacts using the experimental approach presented in this thesis. Early results are promising, and I think with lower temperatures and the recent improvements we have made the experiments have the potential to make interesting measurements on phase coherence near quantum point contacts.

Second, our scanned gate technique could be used to probe transport in ballistic quantum dots. There are specific theoretical predictions which could be tested using our technique. Baranger and Mello have predicted the weak localization correction to the resistance of ballistic quantum dots with a variety of types of real space symmetry.[2] The difficulty in testing the predictions of Baranger and Mello using previously available

---

1. See J.A. Katine, Ph.D. Thesis, Harvard University (1996).
2. Harold U. Baranger and Pier A. Mello, preprint, submitted to *Phys. Rev. Lett.*

techniques is that 2DEGs, and therefore nanostructures, have an intrinsic level of disorder. This disorder makes it difficult to compare small effects, such as the height of the localization correction, between two different nanostructures. The scanned gate technique would allow the same nanostructure to have its symmetry changed during the experiment. To be specific, if the quantum dot is a circle, then the SPM tip could be used to deplete a small region in one part of the circle, removing its up-down symmetry. Comparisons in this type of experiment, where the same nanostructure is used for each measurement, may be able to differentiate between the various symmetries considered in the theoretical work. These experiments would require the SPM to be used in small magnetic fields.

Finally, the scanned gate method could be used to study transport through wide 2DEG regions. The resistivity of 2DEGs determined by the van der Pauw method has variations at the 1-2 % level, in excess of what is expected given the mean free path in these materials.[3,4] By using the scanned gate technique to modify the resistance of an open 2DEG, it may be possible to discover variations in the 2DEG which would account for the anomalous van der Pauw measurements.

Finally, there are two additional microscopies which would be relatively easy to implement in our current SPM, and which could be very valuable tools in studying

3. L.N. Pfeiffer, personal communication.

4. For information on the van der Pauw technique, see the book by D.C. Look, *Electrical Characterization of GaAs Materials and Devices*, John Wiley and Sons, Chichester (1989).

semiconductor nanostructures. Our SPM could be modified to allow for local capacitance measurements or for local voltage measurements. Recent experiments using these techniques on 2DEGs have been performed by other research groups with excellent results.[5,6,7] These capabilities add additional dimensions to the type of scanning probe experiments which can be performed on semiconductor nanostructures.

---

5. M.J. Yoo and H. Hess, 1997 March Meeting of the American Physical Society.

6. R. Ashoori and S.H. Tessmer, 1997 March Meeting of the American Physical Society.

7. K. McCormick, P.L. McEuen, and collaborators, personal communication.

APPENDIX A

Procedure for making PC boards

In the course of experimental research there are a surprising number of simple tasks which need to be accomplished. One important procedure which has not been recorded in previous theses in the Westervelt group is how to make printed circuit boards.

Printed circuit boards are very useful because they result in much tidier electronics. I strongly recommend using printed circuit boards to make any piece of electronics that might be used in an experiment. It will certainly save time in the long run, and it may even speed up the initial construction of the circuit. The following is an overview of the procedure:

- Design the circuit on paper and show it to other people.

- Lay out the circuit design in a drawing program on a computer. Leave plenty of space around components. The standard spacing between pins on op amps is 0.1 inches.
- Print the circuit pattern on printed circuit board transfer film using a standard laser printer.[1]
- Iron the pattern onto a new unpatterned circuit board. It takes a long time to transfer the pattern — keep ironing. Peel the sheet off, and the pattern should be transferred as blue lines onto the copper surface.
- Etch the printed circuit board in the fume hood using the ferric chloride solution. It helps to heat the solution to a temperature of 30 to 50 °C and to stir the solution.
- Rinse the etched board with water, and remove the blue protective layer with acetone and scotchbrite.
- Drill the holes for the components to the correct diameter on a drill press. Wear a mask; the dust from the pc board is not healthy.

The pc board can be mounted using standard insulating spacers available in the Gordon McKay stockroom.

1. Film is available from Techniks Inc.